9-12-2014

Synthesis and Multi-Scale Characterization of Calcium Silicate Hydrate at Multiple CaO/SiO2 Mixture Ratios

Michelle Begaye

Michelle L. Begaye
Candidate

Civil Engineering
Department

This thesis is approved, and it is acceptable in quality and form for publication:
Approved by the Thesis Committee:

Dr. Mahmoud M. Reda Taha , Chairperson

Dr. Arup Maji

Dr. Edward Matteo

SYNTHESIS AND MULTI-SCALE CHARACTERIZATION OF CALCIUM SILICATE HYDRATE AT MULTIPLE CaO/SiO_2 MIXTURE RATIOS

By:
MICHELLE LISA BEGAYE

B.S. CONSTRUCTION ENGINEERING, UNIVERSITY OF NEW MEXICO, 2013

THESIS
Submitted in Partial Fulfillment of the
Requirements for the Degree of

Master of Science

Civil Engineering

The University of New Mexico
Albuquerque, New Mexico

July, 2014

DEDICATION

To my mother: With all your love and guidance, my accomplishment is your accomplishment. Thank you for never giving up on me and inspiring me to move forward and reach my goals. I love you.
To my brothers and sisters: Thank you for being there to pick me up and encourage me to go forth and conquer my fears.

ACKNOWLEDMENTS

I would like to thank the National Science Foundation for funding my graduate education. Without your financial support, my goal would not have been accomplishment and achieved.

Dr. Mahmoud Reda Taha: I would like to personally thank you for this opportunity that you have given me. With all your support, I wouldn't have thought about surpassing the limit that I have set for myself. You have pushed and believed in me when I did not and thought I could not but you never gave up on me. With that said, I am sincerely grateful for your constant guidance and support.

I would like to acknowledge Dr. Usama Kandil, Director of Center of Excellence on Nano-composites and his research group from the Egyptian Petroleum Research Institute (EPRI), Cairo, Egypt for their assistantship in my research. This research would not be possible without their support.

Kenny Martinez: I am fortunate to have you as a friend and a lab-parent that made sure that every morning we ate something. I came close to living in the lab where it was possible to survive with the curing room to be made into a shower room, the lecture room to a bedroom and the living room would be your office. It was possible but by the time I decided to convert this lab to my personal kingdom, it was too late – I'm graduating. Thank you for helping me with making my creativity side come to life and adding to it. I am sincerely indebted you.

I would like to thank my colleagues: Andrew Griffin, Sherif Daghash., Rahulreddy Chennareddy, Justin Brantley, Christine Salas, and Elisa Borowski for their encouragement, assistance ship, support, and help throughout this research.

I would like extend a special thank you to my friends: Sherif Aboubakr , Moneeb Genedy, Rania Ghallab, Adrienne Martinez. Sherif: Thank you for always questioning me and making me understand what I need to do on the next step. Moneeb: I couldn't have asked for a better lab partner and a friend. I am grateful to have such a friend. Rania: Thank you for being there when I needed someone to pick me up. Adrienne: Thank you for being the person you are and allowing me to help you in your project. It was a great experience and opened my eyes to allow my creativity flow.

I am truly thankful to: Mike Gonzales, Sharon Boyd, Hien Pham, Dr. M. Russell, and Dr. Gerstle for your guidance and support.

Synthesis and Multi-Scale Characterization of Calcium Silicate Hydrate at Multiple CaO/SiO_2 Mixture Ratios

by

Michelle Lisa Begaye

B.S., Construction Engineering, University of New Mexico, 2013
M.S., Civil Engineering, University of New Mexico, 2014

ABSTRACT

Calcium Silicate Hydrate (C-S-H) is the primary binding agent that is responsible for setting and hardening, strength, dimensional stability, and durability of Portland cement paste. Although Portland cement hydration produces C-S-H, Calcium hydroxide (CH), ettringite, and other hydration products are also acquired from this process and make it difficult to characterize C-S-H exclusively. C-S-H was first synthesized by mixing calcium oxide (CaO), created by calcining calcium carbonate ($CaCO_3$) that was heated to 950 ºC for 24 hours with fumed silica (SiO_2) and deionized water (H_2O) under nitrogen which produced the synthetic gel-like C-S-H slurry. This composition mixture of synthetic C-S-H was mixed continuously for 7 days with a constant speed and transferred to a filtration system for removal of excess water. The C-S-H gel was then transferred to a drying unit and purged in nitrogen for 5 weeks with a relative humidity (RH) of 11% using Lithium Chloride (LiCl) for 5 weeks. Specimens were obtained by compacting the dried C-S-H powder at 500 MPa. These compacted samples were tested for identifying its mechanical properties on macro, micro, and nano-scale levels. Nanoindentation was

used to identify creep compliance and the reduced elastic modulus of C-S-H. Nanoindentation tests confirmed the 0.7 C/S ratio is stiffer (higher elastic modulus) than C-S-H with 1.5 C/S ratio. Furthermore, C-S-H with 0.7 C/S ratio has a lower creep compliance compared with C-S-H with 1.5 C/S ratios. Microstructural investigations using ^{29}Si nuclear magnetic resonance (NMR) and Transmission Electron Microscopes (TEM) were performed on C-S-H specimens. This work shed light on the significance of silicate polymerization in C-S-H on elastic and creep behavior of cement and concrete. This work might lead to developing alternative cements for concrete structures with time-dependent critical applications.

TABLE OF CONTENT

LIST OF FIGURES

LIST OF TABLES

Chapter 1 Introduction

1.1 Background

The most commonly used man-made building material found in the construction industry is concrete, and its constituents consist of water, aggregate, and cement [1]. The most widely used type of cement is Portland cement, and it has a composition comprised of approximately two-thirds of Calcium Silicate Hydrate (C-S-H) by volume [2]. Most importantly, C-S-H is the hydration product that is held responsible for setting, hardening, strength, dimensional stability, and durability of cement paste and is regarded as the primary binding agent. In addition, C-S-H is defined as an amorphous, poorly-ordered crystalline structure that has caused controversies over its layered nature, and its role of interlayer water on the physical and mechanical properties with no set chemical formula to define its chemical composition [3]. Although many research studies and investigations have been completed, the fundamental understanding of the nanostructure and mechanical properties of C-S-H are still imprecise and need further research.

1.2 Motivation

The 2010 British Petroleum Gulf of Mexico disaster, also referred to as the Deepwater Horizon oil spill, is believed to be the largest accidental oceanic oil spill in the history of petroleum industry to date [4]. In fact, the amount of oil loss with the total discharge estimated at 4.9 million barrels, made evident the ecological and economic challenges that arose from the long months of spill and cleanup activities, which included extensive damage to marine and wildlife habitats [5]. There have been several studies to pin-point the reason behind the explosion and sinking of the Deepwater Horizon oil rig that caused

a sea-floor oil gusher to expel oil for 87 days nonstop. All reports of the investigation have concluded that the main cause, despite the poor management and maintenance of this facility, was from a fracture of the cement barrier that allowed hydrocarbons to flow up through the riser and onto the rig [5]. This resulted in the destruction of the oil rig that ultimately ended in the discharge of the oil spilling into the ocean. This catastrophe and previous tragedies of similar cases have led to the necessity of a new cement composition that can withstand natural and mechanical unseen occurrences that may transpire. The motivation of this research is to develop a correlation between the nanostructure and mechanical attributes of cement for sustainable development of alternative cementitious materials. Although this research does not generate any new types of cement, its focus is to investigate the chemical composition, microstructure, and nano-mechanical behavior on a multi-scale level of varying mixture ratios of synthetic C-S-H.

1.3 Objective

C-S-H features a complex behavior that is dependent upon the calcium oxide (CaO) to silicate (SiO_2) ratio (C/S), curing conditions, compaction level, and other components. The objective of this study has been geared toward synthesizing C-S-H with varying CaO/SiO_2 mixture ratios ranging from 0.6 to 2.0 and observing the nanostructure, elasticity, and creep characterization of synthetic C-S-H. Furthermore, this study investigates the significant changes in silicate polymerization, density, chemical composition, and porosity at the nanostructure on the mechanical properties of C-S-H including storage and loss modulus of elasticity and viscoelasticity of the material.

1.4 Scope of work

In this research, synthesis and characterization of C-S-H was initiated to determine the significance of varying calcium oxide to silica (C/S) mixture ratios from 0.6 to 2.0. The chemical composition of C-S-H makes it complex to characterize C-S-H, solely. Characterizing techniques for 0.7, 1.5, and 2.0 compacted C-S-H samples were achieved by using the Nanoindentation and Dynamic Modulus Analyzer (DMA) to obtain the elastic and viscoelastic properties of the composite C-S-H. Microstructural investigations for C-S-H produced with C/S ratios ranging from 0.6 to 2.0 were performed using Thermo Gravimetric Analysis (TGA), Density Determination, Specific Gravity, Transmission Electron Microscopes (TEM), Scanning Electron Microscopes (SEM), and X-Ray Diffraction (XRD) analysis. ^{29}Si nuclear magnetic resonance (NMR) characterization technique was completed for the observations of silicate polymerization as well as the specific surface area and pore size distribution analysis utilizing the Brunauer-Emmett-Teller (BET) N2 theory and Barrett-Joyner-Halena (BJH) method.

1.5 Thesis outline

The layout for thesis starts with the background and motivation of the significance of C-S-H. Chapter 2 introduces the literature review of C-S-H to include the investigation of the microstructural features of chemical composition and mechanical properties in order to have a better understanding of the nature of C-S-H. Chapter 3 leads into the experimental methodology of synthesizing C-S-H with varying CaO/SiO_2 filtering, drying, and compaction as well as implementing techniques for characterizations. Chapter 4 presents the results and observations with a discussion to integrates the

observations from different experiments performed at different C/S mixing ratios. Finally, Chapter 5 recaps the overall outcomes and presents recommendations for future research.

Chapter 2 Literature Review

2.1 Calcium Silicate Hydrate

Calcium Silicate Hydrate (C-S-H) forms approximately 60% by volume of hydrated Portland cement paste [6, 7, and 8]. It is the main hydration component accountable for its properties that plays a vital role in setting, hardening, shrinkage, creep, diffusion, and dimensional stability within concrete, cement paste, and mortar [2-9]. More so, it is the principal facilitator that stems controversies over the physical and mechanical properties that entails its layered nature and the role of the interlayer water [9]. Its chemical composition has been the focus of many studies by numerous researchers for the last four decades due to the difficulties in the poorly crystalline arrangement and amorphous material properties that are presented in calcium silicate hydrate. These characteristics shaped a level of structural complexity that research has not yet been able to resolve. Nonetheless, Taylor [10] has concluded that there are two types of C-S-H, identified as C-S-H (I) and C-S-H (II), while categorizing C-S-H (I) to a similar structure of 1.4-nm tobermorite and C-S-H (II) to a jennite composition. These minerals entail a layered structure of CaO layers that is connected on both sides by silicate chains following a Dreierketten arrangement. Alizadeh [9], Tennis [11], and Jennings [12], also categorized the C-S-H as Low Density (LD) and High Density (HD), having a volume fraction of 30 and 70%, respectively. It is believed that two-thirds of C-S-H comprise of the low density, while the high density phase encompasses the rest. Another classification for the two morphological entities of C-S-H was termed: Inner, Outer, Middle, and Late Product of C-S-H by Taplin [13] and Richard [14]. Correspondingly, Nonat [15] presented an

alternative nomenclature based on solution equilibrium that consist of three different phases: α-C-S-H (0.66<Ca/Si<1.0), β-C-S-H (1.0<C/Si<1.5) and γ-C-S-H (1.5<Ca/Si<2.0); However, the latter of the three is often used throughout the years in experimental studies. Sugiyama [16] and Taylor [2 and 10] stated that in the development of various synthetic C-S-H structures, the major constraint factor starts with the molar ratio of CaO to SiO_2 (C/S).

2.2 Chemical Composition of Calcium Silicate Hydrate

There are two phases in Portland cement that contains four compounds – Silicate phase, C_3S and β-C_2S and Aluminate phase, C_3A and C_4AF [2, 10, and 17]. In this study, only the silicate phase of the compound C_3S will be observed. In cement chemistry nomenclature denotes C, S, H, A, F for CaO, SiO_2, H_2O, Al_2O_3, and Fe_2O_3, respectively. An indeterminate stoichiometry is implied that signifies the dashes between the lettering of C-S-H. The two important components, crystalline calcium hydroxide (CH) and C-S-H come from the configuration of the chemical reaction between the silicate phases of Portland cement and water [18]. Moreover, the formation of hydration for C-S-H has variable stoichiometry. It is dependent upon the: water to cement ratio, calcium oxide to silica ratio, curing condition, and usage of accompanying materials involved. The work of Cong and Kirkpatrick [19, 20, and 21] concluded that C-S-H is a disarrayed material composed of short silicate chains clasped together by calcium oxide regions with water confined inside the structure. More so, conclusions from previous research have defined that the chemical component has an atomic arrangement similar to 1.4 nm tobermorite and jennite. The crystal structure of 1.4 –nm tobermorite has a chemical formula of $Ca_5Si_6O_{16}(OH)_2 \cdot 8H_20$, where it has been determine to have a composite layer of distorted

central Ca-O sheet that is layered with silicate tetrahedral on each side [9 and 10]. Direct connection of silicate tetrahedron is called Paired tetrahedral and the silicate connecting to two pairs tetrahedral is called Bridging tetrahedral. A schematic diagram is shown in Figure 2.1, illustrating the Ca-O main layer, along with the Paired and Bridging tetrahedral.

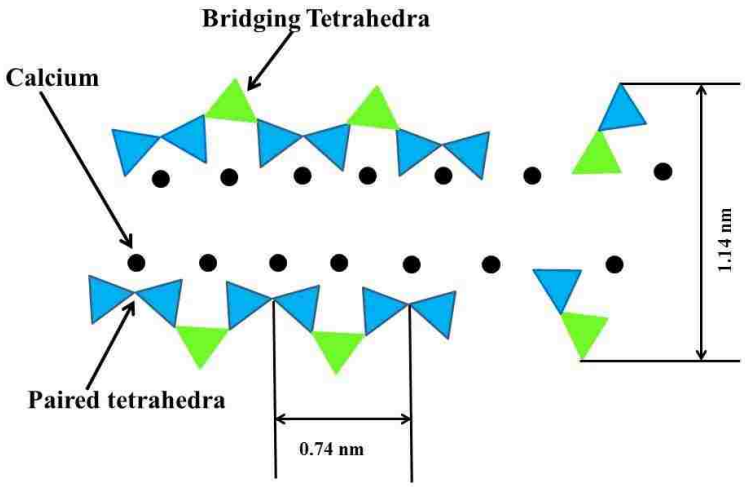

Figure 2.1: Schematic representation of 1.4 nm tobermorite [19]

As previously mentioned C-S-H has similarities in structure to tobermorite but is lacking some bridging tetrahedral and is considered to as a defect tobermorite structure [19]. The overall hydration process observed by both FitzGerald et al [22] and Young [23] can be generally expressed in Equation (2.1):

$$C_3S + (3 + y - x)H \rightarrow C_xSH_y + (3-x)CH \quad (2.1)$$

where, *x*, forms the calcium oxide to silicate (C/S) ratio of the C-S-H and ,*y*, is the total sum of hydroxyl ions and constrained the water molecules that is integrated into the C-S-H gel structure. Both *x* and *y* transforms throughout the reaction and fluctuate in the

sample. Equation (2.1) consists of three separate chemical reactions – Equation (2.2), (2.3) and (2.4) where, tri-calcium silicate, C_3S dissolves in an irreversible exothermic reaction after mixing:

$$Ca_3SiO_5\ (s) + 3H_2O \rightarrow 3Ca^{2+}\ (aq) + 4OH^-\ (aq) + H_2SiO_4^{2-}\ (aq) \quad (2.2)$$

Through a second reaction, the formation of the C-S-H occurs:

$$H_2SiO_4^{\ 2-}(aq)+xCa^{\ 2+}(aq)+(2x^{-2})OH^-(aq)+(y-x)H_2O(l)\rightarrow(CaO)_x(SiO_2)(H_2O)_y \quad (2.3)$$

The Ca/Si ratio, *x*, of the gel resultant has been seen to modify both as a function of hydration time and temperature [22]. Once a critical concentration above the solubility limit has been reached, calcium hydroxide starts to precipitate, expressed as:

$$Ca^{2+}(aq) + 2OH^-(aq) \rightarrow [Ca(OH)_2](s) \quad (2.4)$$

However, to calculate volume and the densities of the reactants, the product must be known. Allen [24] , Tennis [11], and Jennings [12], through experimental investigation found an approximated formula for C-S-H and defined it as $(CaO)_{1.7}(SiO_2)(H_2O)_{1.80}$ with a density of 2.604 mg/m^3 while other researcher varied depending on the specific drying conditions. Renaudin et al [25] specify that several chemical structural types have been solved for the crystalline tobermorite and found that there are three tobermorite families but only two are distinguished in Portland cement that is compatible with the interlayer distance. Among these two families, nine different structural form are designated as: tobermorite 14 Å, tobermorite 11 Å Modo1, tobermorite 11 Å Modo, tobermorite O, tobermorite M, and four clinotobermorite types.

2.3 Models of C-S-H

Initially, studies were experimentally focused on surface area, density, weight, and isotherm change for characterization C-S-H and yet, it is still not completely understood

even with proposed models varying from colloidal to layer-like structures. Powers and Brownyard [26] proposed the first physical models that described C-S-H as a colloidal material. These particles are held together by van der walls' forces and the space between them was called "gel porosity". This gel porosity is only accessible by water molecules. Later, Feldman & Serada's model [27] was developed based on extensive laboratories studies of hydrated cement systems where it explains the role water in time-dependent behavior of hydrated cement paste shown in Figure 2.2. This model is centered on surface area and porosity using nitrogen gas, isotherm of mass, length, and modulus of elasticity changes. The conclusion of this model led to the theory of a layered model for a C-S-H gel and a structural role for the internal area for water as well as explained the changes in the mechanical properties of C-S-H in relationship to water content. In short, the interlayer water displays irreversible behavior during the absorption and desorption processes.

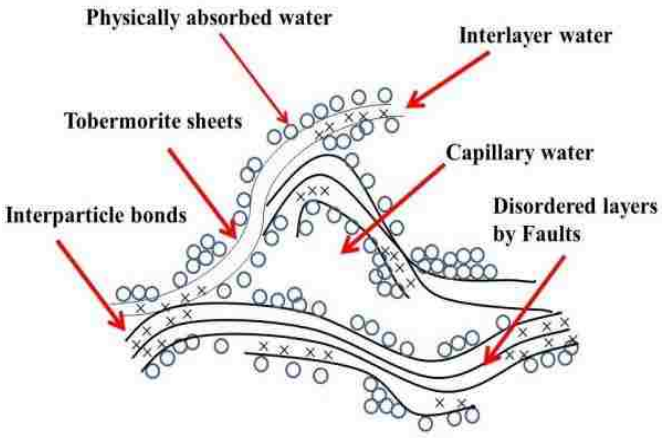

Figure 2.2: Schematic diagram of Feldman & Serada's Model(cf.[2])

Progress in experimental methods led Jennings' to incorporate a new model that features globules and introduced the existence of intraglobular pores (IGP) and small gel pores.

Fundamentally, Jennings colloidal model incorporated the "globules" of C-S-H layers, where it enables C-S-H to exist both a low and high densities. It is expressed that the high density (HD) C-S-H has a packing density of 0.76 while low density (LD) C-S-H has a packing density of 0.63. In addition, the layered model is irreconcilable with the colloid model in its clarification of physic-chemical and engineering behavior. This model neglects the structural role of interlayer water in cement paste as demonstrated by the analogous behavior of synthetic C-S-H (I) and the more amorphous C-S-H existing in the paste. Figure 2.3 features the model by Jennings and co-workers displaying the C-S-H made of globules of about 5 nm in diameter and the absorbed water in the interlayer space; however, this model cannot explain the TEM and soft X-ray imaging studies that shown a fiber or foil-like growth mechanism of C-S-H [18 and 24].

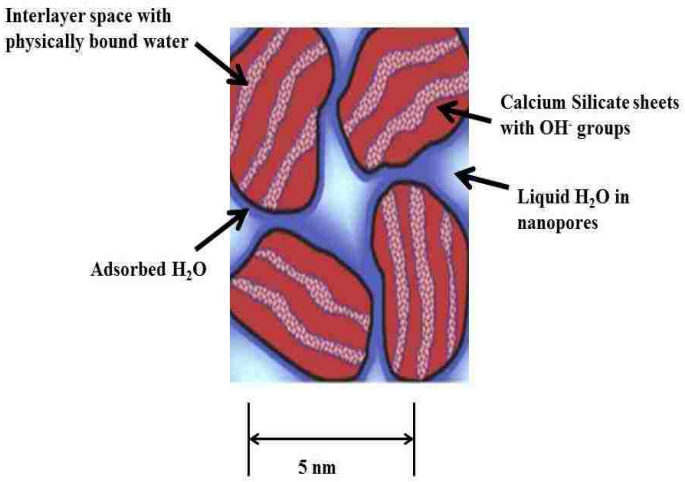

Figure 2.3 Schematic diagram of the nano-scale C-S-H particles (cf.[24])

2.4 Ca/SiO_2 Mixture Ratio

In analyzing C-S-H, researchers have studied extensively over years, with both concentration with cement paste and synthetic or pure C-S-H. Alizadeh et al [28], recently, indicated that the mechanical properties of the compacted C-S-H powder specimen are considered equivalent to those found in the cement paste, concrete, and/or mortar. In fact, he synthesized C-S-H (I) with a C/S ratio of 1.20. Stoichiometric amount of CaO and amorphous silica by mixing with water-to-solid approximately of 11.8 was obtained. The precipitated $CaCO_3$, heated at 900 ºC for 24 hours where CaO was produced. It was then purged with nitrogen gas and stored until required. The amorphous silica was heated at 110º C to dry the material completely. It was then transferred to a high-density polyethylene (HDPE) bottle that was rotated at 16 rpm, continuously for a period of 1 year. Later, he synthesized C-S-H with a C/S ratio of 0.8, 1.0, 1.2, and 1.5 in the exact format with the exception of the time period of 6 month of continuous rotation. The material was filtered for removal of excess water and freeze dried for 4 days under vacuum. The resulting product was stored for further use; however, using thermo gravimetric analysis (TGA) and X-ray diffraction was implemented for immediate characterization. Beaudoin and Feldman [29] formulated an alternative method for synthetic C-S-H by mixing aqueous solutions of sodium metasilicate and calcium oxide with various ratios. Six C/S mixture ratio samples with a range 0.6 to 1.49 were produced. Specimens were dried by bathing in acetone and ether followed by a four day placement under nitrogen to prevent carbonization. The powdered dried specimen of C-S-H was compacted into disks with the dimensions of a 31.8 mm diameter and approximation thickness of 1.27 mm using pressures between 510 and 1360

MPa. The modulus of elasticity was calculated by measuring the center of the compacted disk for the deflection that was supported at three points. Atkins et al [30] used the method of mixing calcium oxide with either silicic acid or silica fume with deionized water. He synthesized C/S ratio ranging from 0.9 to 1.7 where he filtered the samples repeatedly and re-dispersed for removal of impurities and dried to 30% RH using saturated calcium chloride. Sugiyama [16] produced synthetic C/S ratios of C-S-H of 0.65, 0.83, 0.90, 1.10, and 1.20 by mixing calcium oxide with amorphous silica and distilled water. The dry mixed specimens were hydrated for 7 days and dried under vacuum. Renaudin et al [25] synthesized C-S-H by using Degussa, Aerosil 380 silica and freshly decarbonized calcium oxide with a demineralized and decarbonized water to reach a water/solid ratio of 5. Ca/Si atomic ratios of 0.8, 1.0, 1.1, 1.3, 1.5, and 1.7 were created. All the suspension was stored at 20°C under nitrogen for three weeks stirring in a closed polypropylene bottle. Once completed, they were removed and rinsed with acetone and subsequently dried in a desiccator at room temperature. Most recently, Lodeiro et al [31] synthesize four C-S-H gel with a target ratio of 1.9. They prepared the composition by following the procedures of $Ca(NO_3)_2 \cdot 4H_20$ solution of 200 ml of 0.19 M that was added drop by drop to a solution of 0.1 M and a 20 ml of NaOH. Deionized, decarbonized water was used throughout. The solution was continuously mixed at a temperature of 5°C. During synthesis, pure nitrogen was streamed to prevent carbonation. After gel precipitated, it was mixed for 24 hours and left for 2 hours to stand at laboratory temperature of 20-25 °C or until the phases formed – the precipitation and a supernatant. The supernatant was carefully removed and replaced by the same volume of deionized water for removal of the excess sodium and nitrate ion. This was

verified through FTIR of the C-S-H gel. The slurry was filtered using a Buchner funnel under vacuum, while washing the filtrate with distilled water for removal of any residual sodium and nitrate. It was then vacuum- dried inside an AtmosBag to prevent any contamination. All samples were stored in four separate containers until sodium was added. X-ray Diffraction and SEM/EDX were completed on all samples to verify the production composition. All in all, synthesizing C-S-H gives an in-depth resource to analysis the chemical composition more closely with the capability to investigate the nanostructure of C-S-H. Each researcher were successfully in producing synthetic C-S-H to analyze the characterization of their project in which established the groundwork of future analysis for this complex material, the principal binding agent of Portland cement.

Dynamic Modulus Analyzer

Dynamic Modulus Analyzer (DMA) is a technique that is generally applied to characterize a material's properties as a function of temperature, time, and frequency where it determines the mechanical properties by the analysis of an oscillating force that is applied on a specimen in a sinusoidal form. It measures the storage modulus, loss modulus, and the tan delta of a material. Pourbeik et al [60] obtained the storage modulus (E') and found the measurements to be nearly frequency independent within the range of 0.1 to 5 Hz. Alizadeh et al [9] characterized dynamic mechanical behavior at 11% Relative Humidity and found the properties of C-S-H with the C/S mixture ratio ranging from 0.8 to 1.5 to be dependent on its ratio. In fact, the resultants showed a decrease in the storage modulus with an increase in the tan delta as the C/S ratio of the C-S-H increases. This alluded to the conclusion that the observation of the changing in the stiffness and damping of C-S-H conditioned to moisture contents lower than 11% RH

was due to the absorbed and interlayer water contributing significantly to the dynamic mechanical behavior. Figure 2.4 displays the comparisons results of storage modulus and tan delta of DMA results of C/S mixture ratios of 0.8 to 1.5 C-S-H with Portland cement paste and porous glass.

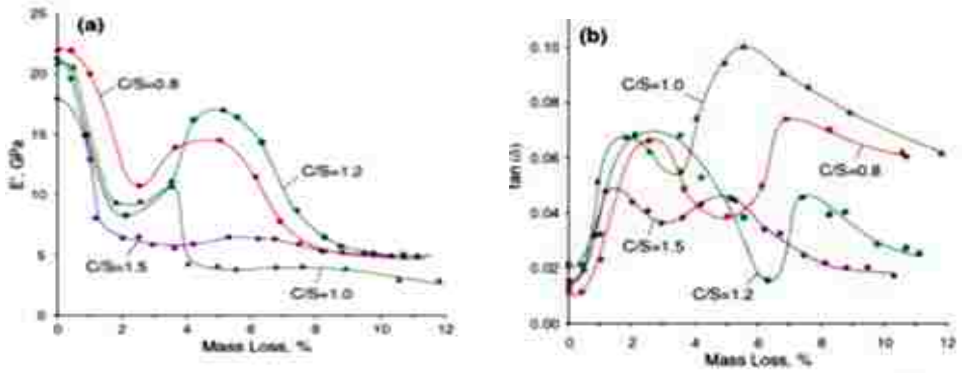

Figure 2.4: (a) Storage Modulus (b) tan(δ) published by Alizadeh et al [9]

2.5 Nanoindentation

Nanoindentation is an extensively acceptable tool to measure the mechanical properties of small materials for characterization of elastic, and plastic properties such as hardness and time dependent properties such as the stress exponent for creep. This technique uses a 3-sided pyramidal diamond Berkovich tip to minimize deformation. In the performance of Nanoindentation, it involves the instrumental loading of a surface while observing the applied force as a function of time and displacement into the surface as a function of time. In this particular technique, it determines the elastic properties and measures the time-dependent mechanical properties as well. Several studies and research have conducted this technique using atypical cement and cement composition. Vandamme and Ulm [46] performed the measurement of "creep modulus" while Da Silva et al [47] measured the elastic properties that is affected by creep in cement paste. In addition,

Constantinides and Ulm [48] determined the appropriate depth for the properties of C-S-H in hydrated cement where the maximum should be 1/10 of the depth of the material phase, where the depth range is defined as $d<<h_{max}<D/10$. d is denoted as the size of a single colloidal particle of C-S-H, approximately 5 nm. More so, Constantinides and Ulm [49] have used this technique to identify the volume fractions of both high density and low density C-S-H, where it was conducted by 200 indentations on hydrated ordinary Portland cement paste with a water-cement ratio of 0.5. The result concluded the low density, low stiffness phase of C-S-H has an elastic modulus of approximately 21.7 GPa while the high density, high stiffness elastic modulus is roughly 29.4 GPa. Mondal et al , [49] also, reported similar values of 23 GPa for a unhydrated particle of C-S-H. Not to mention, Kim et al [35] presented the relative fraction of Young's modulus values ranging of 1.2 -15.4 GPa and 17.1-32.0 GPa for the C/S mixture ratios of 0.7, 1.0, and 1.2 C-S-H.

2.6 Brunauer Emmett Teller (BET) and Barrett-Joyner-Halena (BJH)

When analyzing the mechanical properties of C-S-H, its modulus of elasticity, creep, and strength are dependent upon porosity. Behaviors of the physical and mechanical properties are strongly affected by the distribution of the pores within the solid. Having various sizes and shapes, along with the unity between the pores allow for the characterization of C-S-H's pore structure to be complex and complicated. Once obtained, the parameters of the characterization can determine porosity, hydraulic radius, specific surface area, pore size distribution, and threshold diameter. Several methods can be used to study pore structure but experimental test depends upon the principal technique used to create the specimen. One method that has been used is the Gas

adsorption technique for observation C-S-H gel pores by using the Brunauer-Emmett Teller (BET) technique using nitrogen, N_2. BET-N_2's analysis provides specific surface area evaluation by measuring relative pressure using a fully automated analyzer. This technique incorporates external area and pore area to determine the total specific surface area that serves as the basis of important analysis for measurement of the surface area of the material. Although the BET method was derived over 60 years, it is continuous used for gas adsorption analysis due to its simplicity. Oder [36] found that the factors to determine the BET-Specific Surface of hydrated Portland cement and related materials are affected by composition, curing conditions, sample preparation and the way free water is removed from the pore system. He, also, compared the BET-H_20 and BET-N_2 where he observed that the BET-N_2 has consistently lower resultants caused by the ability of Nitrogen molecules to penetrate small pore entrances and did not enter the interlayered spaces. It was concluded that the nitrogen molecules remain only adsorbed at the surface and thus the obtained BET-N_2 values reflect the true surface area of the material [36, 37]. In fact, Juenger and Jennings [38] used the BET method to calculate the surface area over a relative pressure of 0.05 – 0.025 on the adsorption isotherm. This data was then used to calculate the porosity and pore size distribution by using the Barrett, Joyner, and Hallenda (BJH) method from the desorption isotherm. This technique only measured pores in cement paste with radii between the 1 and 40 nm. In analyzing the analysis of BET-N_2, there are six types of adsorption isotherms obtained for various materials given by S. Brunauer et al [39] shown in Figure 2.5. Type I is referred to as the Langmuir type isotherms where the adsorption on the specimen's pore walls is restricted to a monolayer. Type II isotherms are a sigmoid isotherms and represents multilayer adsorption on non-

porous solid. Type III are obtain from solids with macropores while Type V isotherm are from solids having micropores or mesopores with high relative pressure. Type VI is observed in carbon blacks and is considered rare due to the fact, it is obtain from an adsorbent with a uniform outside surfaces and usually not considered for analysis. Type IV and V are valid for porous material only in which there are modification of isotherms of type II and III. According to the International Union of Pure and Applied Chemistry (IUPAC) classification, the isotherm that is associated with the cement paste is Type IV where the hysteresis loop is related to the pore condensation. Guerrero et al [40] have found that the principal results of the surface area decreases continuously from 17.16 m^2/g to 9.19 m^2/g. It is also noted that the maxima peak from 30 nm to 70 nm has been transformed into a peak of higher intensity where it found there is a higher micro-pore volume and a lower specific surface area in which is concordance with the NMR spectra.

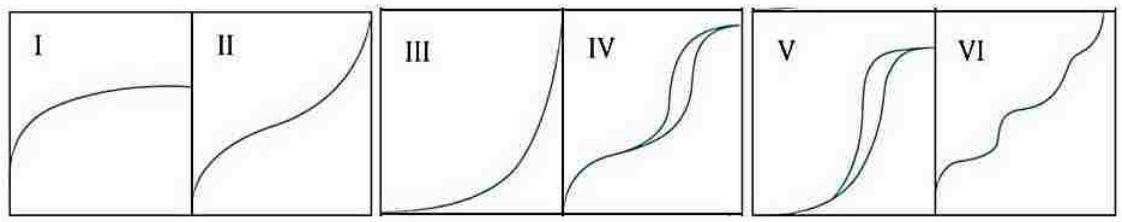

Figure 2.5: Types of adsorption isotherm obtained by the IUPAC Recommendations

2.7 Thermo gravimetric Analysis (TGA)

In cement literature, various researchers used TGA to verify the water lost in C-S-H; however, the resultant of each varied among them. For example, Odelson et al [32] reported the water lost segment is from the temperature range of 200°C to 400°C while Alarcon-Ruiz et al [33] found it to be 180°C to 300°C. Alizadeh et al [28] located the

ambient temperature about 250°C to be associated with the removal of free, adsorbed, and interlayer water. Alonson and Fernandez [8] attained the temperature range to be 100°C to 250°C while Jain and Neithalath [34] , Foley et al [7] ,and Kim et al [35] determined it to be 125°C to 150°C. The mass loss from the temperature ranging 400°C to 600°C is measured as the mass loss of CH and from 600 °C to 825 °C is considered the decomposition of $CaCO_3$. After calculating the content of both CH and $COCO_3$, the rest is found to be C-S-H. In addition to this, Foley et al [7] and Kim et al [35] were able to use this technique to calculate the stoichiometric formula of C-S-H with the measured TGA values using the molecular weights of water, CH, and C-S-H, respectively.

2.8 X-Ray Diffraction Analysis

Alizadeh [44] has defined the X-ray pattern for C-S-H to have three strong peaks located at 1.250, 0.304, and 0.280 nm. It was also stated that the 002 basal spacing at 1.250 nm is sensitive to change in relative humidity and moisture content. However, Cong and Kirkpatrick [19] found that their sample of C/S ratio of 1.5 showed between 5 and 13 peaks with semi-crystalline arrangement. It was found that the number of peaks decreased with increasing C/S ratio mixture that indicates less long-range order. While Li and Roy [45] found the X-ray diffraction results was consistent with the chemical analysis that indicates that the hydration product of 1.5 and 0.83 C/S mixture ratio. Foley et al [7] and Kim et al [35] were able to show several phases of C-S-H, CH, and CaCO3 for both d-dry and 11% dried specimens and found that the XRD peaks were attributable to C-S-H found in previous published results. Furthermore, XRD analyses are used to determine the intensity and the angle of the diffracted X-ray beam after encountering a plane of atoms for the material of C-S-H. Figure 2.6 shows a XRDA plot of C-S-H of a

comparision between varying mixture ratio of C-S-H and the Peaks presented where it shows both the CH presented in the specimen.

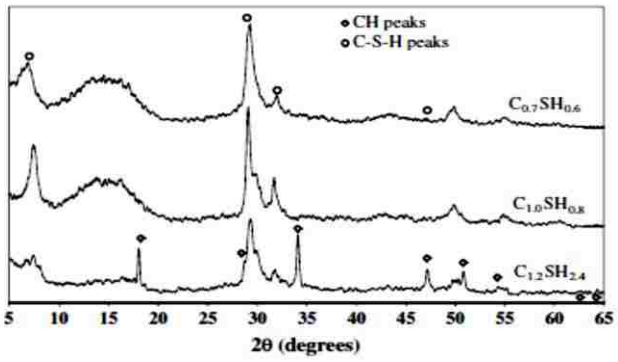

Figure 2.6: XRD spectrum of varying C/S mixture ratios published by Kim et al for [36]

2.9 ^{29} Si Magic Angle Spinning Nuclear Magnetic (NMR)

In prior years, new advancement in technologies with analytical techniques and application has surfaced, giving new methods for research in C-S-H such as the nuclear magnetic resonance (NMR) spectroscopy. Indeed, the NMR testing has proven to be the most effective technique for chemical composition in regards to identifying its bonding. In this technique, a standard reference sample is needed to determine the difference in peak for the specimen. This difference is defined as the chemical shift and is typically multiplied by 10^6 whilst the unit is denoted as parts per million (ppm). The notation Q^n is specifying as number of bridging molecules that is in connection with multiple Si molecules. Q^0 is distinguished for no bridging in the unhydrated cement. Q^1, Q^2 and Q^3, and Q^4 expresses increasing polymerization where Q^4 is characterize of having pure silica fume and sand. Magi et al [41] displays the ^{29} Si chemical shifts that is published for the ranges of silicates where it is used as a reference for C-S-H as shown in Figure 2.7. In addition, Young [42] hydrated tri-calcium silicate (C_3S) and white Portland cement in

which he reported an increase in polymerization that consequently caused a chemical shift. Analyzing the result, it is compared to cement pastes that were cured under elevated temperature. For specimens cured at 2ºC and 25ºC, the observation for these samples were found to be in the Q^1 bond while the 65ºC were shifted to indicate an increase of Q^2 and having a peak at -85.3 ppm. This specifies that at this particular region, it has longer silicate chains. In this study, he did not report any Q^3 observed in which would have led to cross-linking. Other authors such as Cong and Kirkpatricks [19] produced synthetic C-S-H using three different methods for variation and concluded that the sample with the lowest C/S ratio showed the majority of Q^2 bonding. The highest bonding designates a stronger Q^1 silicate chains as opposed to the C/S ratio of 1.2 and 1.5 C-S-H, concluding to having a near-equal ratios of Q^1 and Q^2. Alonso and Fernandez's [8] analysis of their specimen of hydrated cement paste also showed peaks for Q^0, Q^1, and Q^2. Another research by Yu and Kirkpatrick [43] was studied in respect to the effects of elevated temperatures on synthetic low C/S ratio of C-S-H. Their resultant observed a formation of meta-stable and stable phases of Q^3 and Q^4 shifts. It was concluded there exist cross-linking occurrences from the charge balance after the removal of hydrogen from the Si-OH groups.

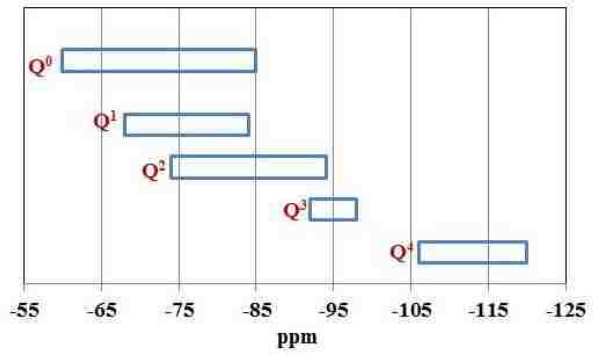

Figure 2.7: ^{29} Si Chemical shift ranges of silicates published by Magi et al [30].

Chapter 3 Experimental Methods

This section explains the experimental methods in the development of the synthetic C-S-H including the material that was used, synthesizing of the technique and procedures, tests setups and methods of analysis that was utilized. We begin with the materials that were incorporated for C-S-H synthesis followed by the preparation of varying calcium to silicate (C/S) mixture ratio ranging from 0.6 to 2.0, and leading into the filtering and drying set up of 11% relatively humidity (RH). Next, the powder specimens were compacted to the pressure of 500 MPa. Consequently, this chapter ends with the diverse characterization and identification techniques that were used to describe C-S-H.

3.1 Materials properties and mix preparation

3.1.1 Pure Lime

Reagent grade calcium carbonate ($CaCO_3$) was used from Mallinchrodt Chemicals to produce lime (CaO) for this research. Approximately, 37 grams of calcium carbonate ($CaCO_3$) was set into a ceramic bowl and placed into the 6000 Thermolyne Furnace to produce lime. The chemical reaction for this process is the following:

$$CaCO_3 \xrightarrow{\text{Heat}} CaO + CO_2 \qquad (3.1)$$

, where $CaCO_3$ is heated to 950 ºC for 24 hours, resulting into calcium oxide (CaO) and carbon dioxide (CO_2). The ceramic bowl was immediately transferred to the glove box purged in nitrogen to pertain the purity of the lime. Once exposed to Oxygen (O), it can be transformed back into $CaCO_3$, in which may cause carbonation contamination to any future C-S-H mixes. Figure 3.1 shows the before and after results of the calcium carbonate where thermo gravimetric analysis (TGA) and weighing of the content was used to determine the purity for verification of the lime.

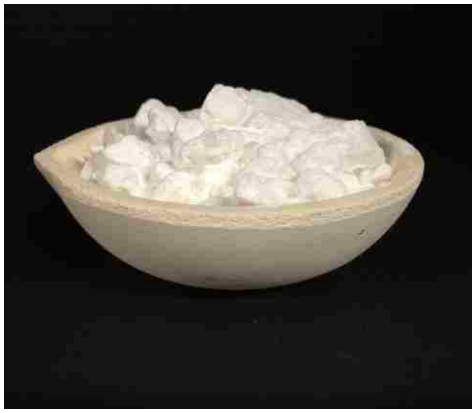
(a)

(b)

Figure 3.1: (a) Calcium Carbonate (b) Lime

3.1.2 Fume Silica and Deionized Water

Fume silica supplied by Aldrich were used with a 99.8% purity and enough deionized water provided by the University of New Mexico asphalt laboratory to form a gel-like slurry.

(a)


(b)

Figure 3.2: (a) Deionized Water (b) Fume Silica

3.2 Synthesis of C-S-H

In synthesizing, Calcium Oxide, CaO, and Fumed Silica, SiO_2, were combined into a mixture of a CaO to SiO_2 (C/S) ratio mixtures ranging from 0.6 to 2.0. The amount of

materials in each C/S mixture ratio is specified in Table 3.1. In each preparation, 10 grams of CaO and 400 grams of deionized water were held constant while the fumed SiO_2 was the varying agent that was calculated for each individual proportion that needed for each blend to produce an aqueous solution. The C/S ratios were selected after numerous investigation of C-S-H [7, 9, 15, 35, and 44].

Table 3.1: Mix proportion of C/S ratios

C/S Ratio	CaO (g)	SiO_2 (g)	H_2O (g)
0.6	10	17.8	400
0.7	10	15.3	400
0.9	10	11.2	400
1.2	10	8.92	400
1.5	10	6.69	400
1.8	10	5.94	400
2	10	5.35	400

Each C-S-H calcium to silicate mixture ratio resulted in an aqueous, gel-like slurry structure that was transferred to a double drum rotary rock tumbler that was purged in nitrogen with an air tight seal lid for a continuous blend for a week to ensure complete reaction. On the 7^{th} day, the gel-like C-S-H slurry was removed and placed into a filtration system for removal of excess water for 24 hours under nitrogen to prevent carbonization. Maximum care in transporting the slurry was crucial to prevent any contamination. This filtration system includes a two 1000 ml beaker with two 47 mm filter holder that holds a 0.7 µm filter paper, support base, stainless steel screen, and an aluminum clamp that is connected to a vacuum source. Figure 3.3 displays the mixing apparatus and Figure 3.4 exhibits the set-up of the filtration system used.

Figure 3.3: Mixing Apparatus

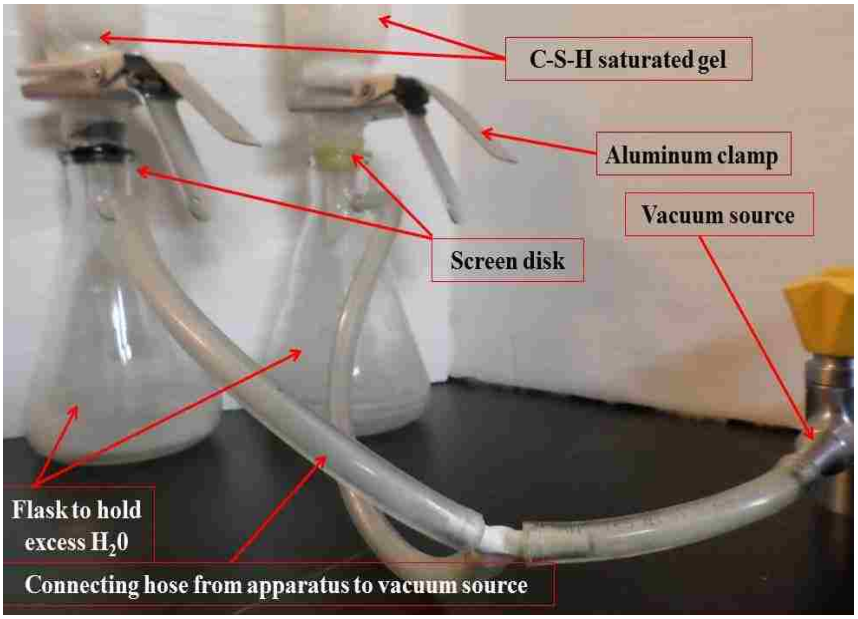

Figure 3.4: Filtering System to remove excess water from mixture

Once the excess water was removed, the C-S-H gel was placed into polyethylene containers for the set-up for the equilibration drying method of 11% Relative Humility

(RH) using saturated Lithium Chloride (LiCl). Each container was set up with a connecting hose with a turn value in series to enable the relative humidity (RH) to flow smoothly throughout. The salt solution was prepared in accords to the ASTM Standard E 104-02 [50]. This system was arranged as a series of 1 beaker and one to four purged nitrogen containers, depending on the number of mixes produced. The first beaker contained the saturated LiCl solution placed on a hot plate with the setting of 55 degree Celsius to keep the ambient temperature in the beaker constant. The second container enclose the saturated C-S-H gel and connected to a vacuum tubing to the Drierite (calcium sulfate and cobalt chloride) held in the third beaker to catch the excess water before it reached the vacuum. The system was first primed without the C-S-H gel in the second container to ensure no air seepage into the connection by verifying the 11% RH by the meter, as well as, reaching equilibrium under the vacuum for five days to confirm the salt solution to achieve steady state. On the fifth day, the saturate C-S-H gel was placed inside the empty second container by using the shut off values fixed on both sides connected to both beakers of the Lithium chloride (LiCl) and Drierite. Next, clamping both vacuum hose that is attached to the container's lid with sealant connectors and transporting this container(s) to the glove box to safeguard any type of contamination from either air and/or atmospheric humidity (room temperature of 25ºC). Similar disconnections were conducted each day to weigh the C-S-H gel specimens to maintain till reaching a constant weight loss. Once this is completed, the container is transported to the glove box to replace the container's lid to seal the powder specimen until further testing is required. Figure 3.5 displays the entire drying system of the 11% RH. This

drying process typically took 4 to 5 weeks to produce a powder specimen of synthetic C-S-H at 11% RH.

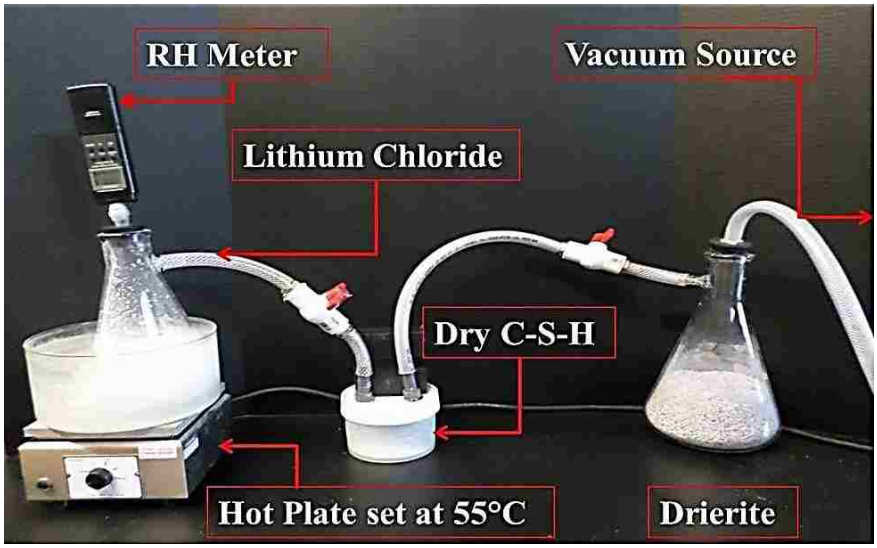

Figure 3.5: 11% Drying System Set-up

3.3 Compaction

All powder preparation was performed in a glove box filled with nitrogen to prevent any contamination or carbonization prior to compaction. This method of compaction was accomplished by one type of systems that comprise of puzzle pieces in a rectangular shape apparatus that can be arranged into two different dimensions – Type A and B. This system has six bolts, one base plate that has a thickness of 25.9 mm, four different pieces for Type A: dimension of 25 x 30 mm (length by width) and four pieces for Type B: dimension of 5 x 10 mm. Two different plunger members for each type and one square ring that surrounds the middle pieces for any expansion or yielding in the harden steel. Under Type A rectangular design, 3.5 g of C-S-H dried powder was utilized and under Type B, 1.60 g of C-S-H dried powder was employed to create a rectangular tile like

specimen under the pressure of 500 MPa. All loads were applied under constant load rate of 1% maximum load per second and held at maximum load for 3 minutes before unloading. Five tile-like plates of each type of C-S-H were made from each device. Figure 3.6 displays the compaction apparatus and the compaction loading. Compactions were accomplished by using Instron® testing machine and the load and displacement were recorded. Each load compaction displacement were recorded and used in the analysis to compare with Alizadeh's curves [44] shown in Figure 3.7. This comparison allows our data to rationale the selection of compressing the specimen to the range of 500 MPa that will simulate C-S-H porosity of concrete at specific w/c ratio. In addition, compacting specimen allows other techniques such as DMA and Nanoindentation to be observed. Figure 3.8 displays the compaction C-S-H specimens. Furthermore, utilizing the loading-unloading pressure-displacement curves from the compaction results, the bulk modulus of elasticity (E_b) of C-S-H specimen at different compaction pressures was acquired using Equation 3.2 shown below.

$$E_b = S_t (t_f - t_r) \quad (3.2)$$

Where S_t is denoted as the slope of the tangent of the unloading pressure-displacement curve shown in chapter 4, t_f is the thickness of the specimen calculated by dividing 3.5 g of C-S-H by specimen area and the measured specimen density that represents initial height of the C-S-H prior to compaction. t_r is expressed as the rebound thickness of C-S-H after compaction unloading.

Figure 3.6: Compaction Apparatus and compaction loading

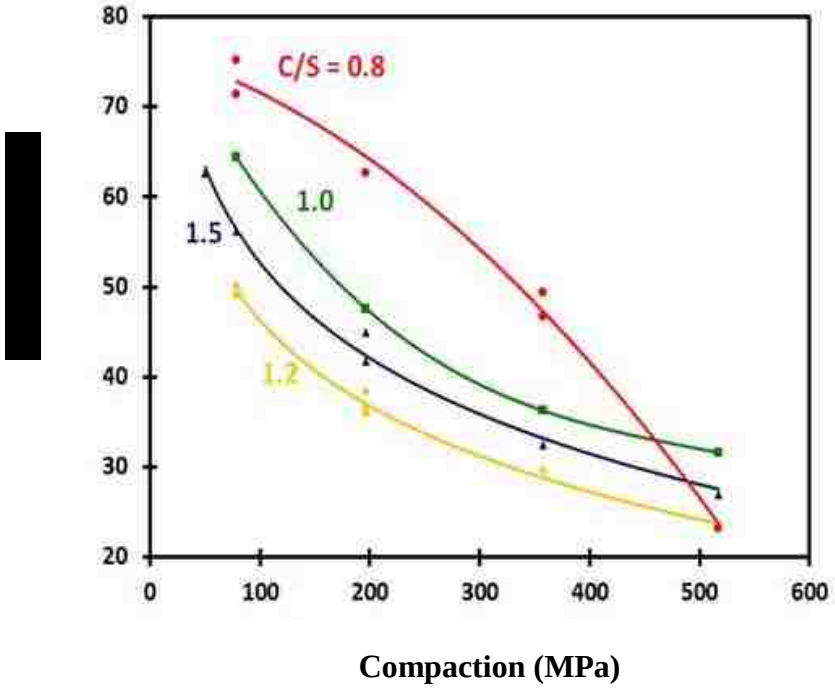

Figure 3.7: Alizadeh's Porosity of compacted C-S-H at various pressures [44]

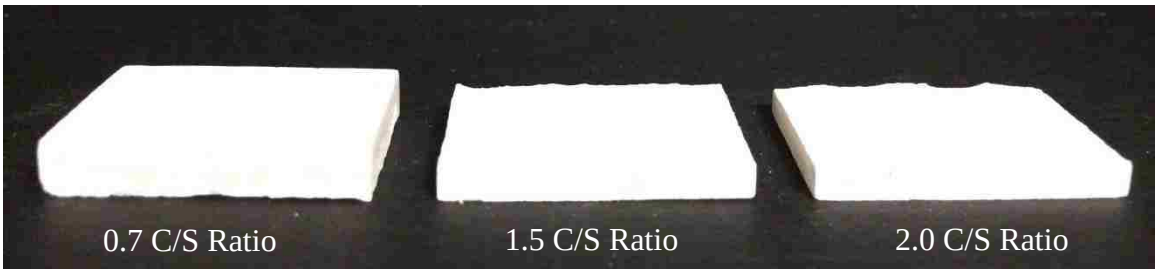

Figure 3.8: 0.7 and 1.5 C/S Mixture ratios compacted at 500 MPa

3.4 Density

Density was determined for both 0.7, 1.5, and 2.0 C/S mixture ratio for the compacted and powder specimens in accords to the ASTM Standard C 914-95 [51] and ASTM Standard C188-09 [52]. These distinct ratios were selected to analyze the categories of CSH (I) where 0.7 falls into this region while 1.5 defines the beginning of CSH (II) territory classified by Taylor [2 and 10] as well as looking more closely at the mixture ratio of 2.0.

3.4.1 Density: Compacted Specimen

Five specimens of each 0.7, 1.5 and 2.0 C/S mixture ratios from the Type A system were compacted with a pressure ranging from 200 MPa to 500 MPa. Each specimen was individually cut into uniform dimensions of 30x20 mm, producing twenty samples for each C/S ratio. Using a Mettler Toledo XS-64 analytical balance with a density kit shown in Figure 3.9 was utilized for the density determinant. The specimens were first weighed to determine the uncoated Mass (M_{un}) and dipped into paraffin wax corresponding to the ASTM Standard D 87 [53] until fully coated as shown in Figure 3.10. After drying, the specimens were re-weighed to measure the mass of the coated specimen (M_{coated}) and

submerged into ethanol. Using the equation 3.3, mass of the wax (M_{wax}) can be calculated:

$$M_{wax} = M_{uncoated} - M_{coated} \tag{3.3}$$

Using the calculated M_{wax} value, the volume of wax (V_{wax}) can be determine using the equation 3.4:

$$V_{wax} = \frac{M_{wax}}{\rho_{wax}} \tag{3.4}$$

where ρ_{wax} is the density of the paraffin wax. Although the ASTM Standards defines this procedure to use H_2O for the submersion fluid, ethanol was used instead for a more accurate measurement for the simple reason that the coated specimen of C-S-H floated, causing an impossible reading for measurement. The coated specimens were submerged and weighed to measure the submerged mass ($M_{coatedsub}$) to calculate the volume of the coated sample using the equation 3.5:

$$V_{coated\ sample} = \frac{M_{coated} - M_{coatedsub}}{\rho_{ethanol}} \tag{3.5}$$

where $\rho_{ethanol}$ is the density of the ethanol. Utilizing equation 3.3 and 3.4, equation 3.5 calculates the volume of the uncoated sample where $V_{uncoated}$ is the volume of the uncoated C-S-H specimen without wax and V_{coated} is defined as the specimen coated with the paraffin wax while V_{wax} is the volume of the paraffin wax coating the C-S-H specimens. While following the ASTM standard, the paraffin fluctuates in density to cause inaccuracies in measurement that affected the results. Aware of this difficulty, a specific process for calibration using fifteen metal coins were performed. Coins, non-porous material, were chosen since the density of a coin can be reproduce and the consistency of the density measurement taken over and over again. This process was

attested accurate enough for determining densities of C-S-H with an average coefficient of variation less than 3% and follows published previous results.

Figure 3.9: Mettler Toledo XS-64 analytical balance with a density kit

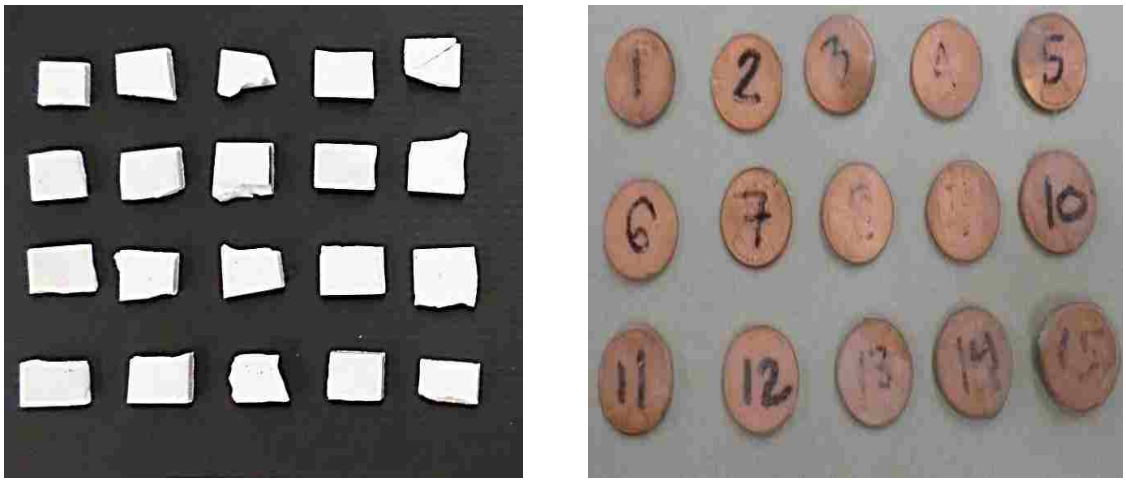

Figure 3.10: coated C-S-H and pennies specimen

3.4.2 Density: Powdered Particle Specimen

Twenty dried powder specimens of 1 gram of 0.7, 1.5, and 2.0 C/S ratio of C-S-H was used to determine the density using the Le Chatelier apparatus shown in Figure 3.11. The

Le Chatelier glass device consists of a 250 ml capacity, with graduated neck from 0 to 1 ml and from 18 to 24 ml in 0.1 ml graduation with accuracy of 0.05 ml. Kerosene with a density of 0.79 g/mL at 25ºC was used to fill the flask to the point marked zero ml on the stem. Using a lint-free cloth, the stem was dried above the marked zero level after pouring and the initial volume measurement was recorded. One gram of the powdered C-S-H specimen was added in small increments to avoid any splashing or adhere to the inside of the flask above the liquid. Once completed in the placement of the powder specimen in the liquid area of the flask, a stopper is set in the flask, held slightly inclined, and gently rotated in a horizontal circle to release any entrapped air from the specimen until no air bubbles is seen. Once set on a flat surface, the final measurement of volume displacement (ml) was recorded and repeated for all specimens. Equation 3.5 determines the density, ρ, of the C-S-H specimens:

$$\rho\left(\frac{g}{cm^3}\right) = \frac{Mass\ of\ specimen}{Volume\ displacement} \tag{3.5}$$

where the volume displacement is the difference between the first and final measurement recorded by the mass of the specimen used in the test.

Figure 3.11: Le Chatelier apparatus

3.5 Dynamic Modulus Analyzer

The Dynamic Modulus Analyzer (DMA) was conducted using a TTDMA instrument and tested at a frequency from 1 Hz to 3 Hz. This technique was performed to determine the mechanical properties of the C-S-H specimen of 0.7, 1.5, and 2.0 C/S mixture ratio under a controlled environment of 11% Relative Humidity (RH) with the average temperature of 22ºC. A three-point bending set-up for this analysis was employed. Three compacted C-S-H specimens shown in Figure 3.12 with dimension of 25x10 mm were implemented for this analysis.

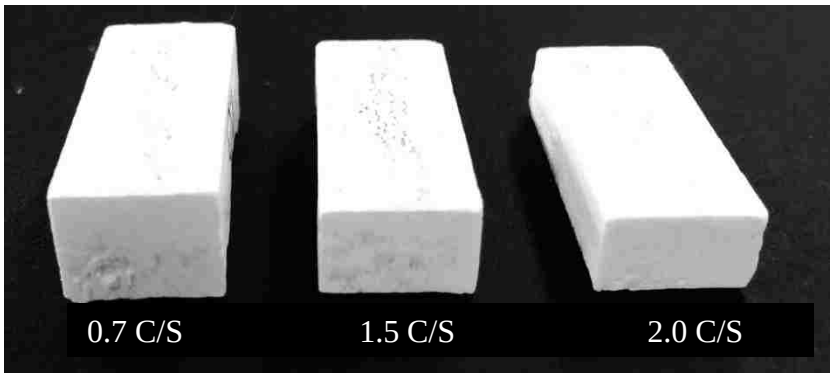

Figure 3.12: DMA compacted specimens

The application of the DMA allows the observation of both elastic and viscoelastic properties of the C-S-H specimens to be analyzed. In this technique, the displacements of the specimens were measured when an oscillating force is a pplied and the reaction of the material is used to calculate the elastic modulus and creep compliance of the C-S-H specimens. Equation 3.17 denotes the oscillating load $P(t,\omega)$ when applied with an amplitude (P_o) when the tensile stresses of C-S-H are within elastic limits.

$$P(t,\omega) = P_o \cos\omega t \tag{3.17}$$

Equation 3.18 calculates the resulting flexural stress with amplitude of (σ_o), where Equation 3.19 signifies the normal strain $\varepsilon(t,\omega)$ with an amplitude of (ε_o). The time lag (Δt) between the two responses are obtained as shown in Figure 3.19 and described by Equations (3.17 through 3.19)

$$\sigma(t,\omega) = \sigma_o e^{i\omega t} = \sigma_o(\cos\omega t + i\sin\omega t) \tag{3.18}$$

$$\varepsilon(t,\omega) = \varepsilon_o e^{i(\omega t-\delta)} = \varepsilon_o[\cos(\omega t-\delta) + i\sin(\omega t-\delta)] \tag{3.19}$$

where, ω, is the angular frequency in rad./sec and equal to $\omega = 2\pi f$ and (δ) represents the phase angle. Also, the phase angle, δ is a function of the internal friction of the material with angle of 0° denotes the ideal elastic behavior and angle of 90° signifies the ideal viscous behavior. The elastic moduli (complex modulus (E^*), the storage modulus (E') and the loss modulus (E'') can be calculated from observing the above dynamic response as described in Equations (3.20) and (3.21).

$$E^* = \frac{\sigma_o}{\varepsilon_o}(\cos\delta + i\sin\delta) = \quad \frac{\sigma_0}{E_0} * e^{i\delta} \tag{3.20}$$

$$E' = E^*\cos\delta \ , E'' = E^*\sin\delta \ \& \ \tan\delta = \frac{E''}{E'} \tag{3.21}$$

In both elastic and viscous resistance, the complex elastic modulus (E^*) is an indicator to the resistance to dynamic loading. The storage modulus (E') is correlated with energy storage representing the elastic behavior while the loss modulus (E'') linked with the dissipation of energy representing the viscous behavior. The phase angle can be calculated using Equation (3.21). Additionally, the same measurements can be used to

determine the complex creep compliance (J^*) using Equation (3.22) and it is the inverse of the complex modulus from a mechanical point of view.

$$J^* = \frac{\varepsilon_o}{\sigma_o}(\cos\delta - i\sin\delta) = \frac{\varepsilon_0}{\sigma_0} * e^{-i\delta} \tag{3.22}$$

Figure 3.14 exhibits the oscillating stress and strain graph in relationship to storage, loss and complex modulus while Figure 3.13 displays the DMA test equipment use for this technique.


(a)

(b)

Figure 3.13: DMA test (a) instrument (b) C-S-H specimen installed in bending mode

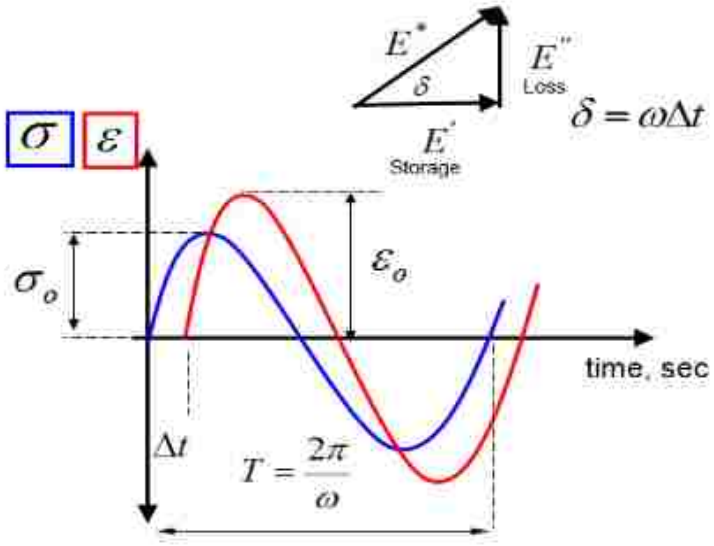

Figure 3.14: DMA oscillating stress and strain graph

3.6 Nanoindentation

Nanoindentation was performed to mechanically characterize the C-S-H specimen at the nanoscale. Compacted specimens were prepared for nanoindentation by casting thumbnails samples in a fast set acrylic to keep the specimens in place for polishing. The specimens were ground and polished on a Buehler Ecomet 3 auto-polisher with a Buehler 2 power head shown in Figure 3.15. Water was used for lubrication for polishing to obtain a very flat and smooth surface finished using 125-micron, 70-micron, 30-micron, 9-micron, and 1-micron diamond pad on sequences for 10, 15, 15, 30, and 60 minutes respectively. Between increments, specimens placed in an ultrasonic bath to remove dust and diamond particles left on the surface for 2 minutes. After completing the polishing procedure, it was shown for the C-S-H specimens to have mirror-like surface reflecting overhead light. Depth versus load Hysteresis nanoindentation test was performed using NanoTest^{TM} 600 indenter system from Micro Materials, Inc., Wrexham, UK shown in Figure 3.16. Nanoindentation was carried out using Berkovich indenter tip with a loading and unloading rate of 0.0125 mN/sec, initial load of 0.05 mN, maximum load of 0.55 mN. The maximum load was held for a dwell time of 120 second to investigate nano-creep behavior. The indentations were made on twenty gridlines spaced 50 µm apart. Each gridline contained 20 indentations spaced at 50 µm producing 400 indentations. To correct for thermal drift, the load-indentation data was recorded post indentation. The recorded load-indentation data was analyzed by utilizing the method outlined by Oliver and Pharr [54]. The reduced modulus E_r is computed as a function of moduli of elasticity and passion's ratios of the indenter and the indented surface. Accordingly, the reduced modulus E_r is computed as:

$$E_r = \frac{\sqrt{\pi}}{2\beta}\left(\frac{\frac{dP}{dh}}{\sqrt{24.5\, h_c^2}}\right) \tag{3.23}$$

Where, β, denotes the correction factor to account for the non-symmetrical shape of the indenter tip, which is equal to 1.034 for a 3-sided pyramidal (Berkovich) indenter. h_c is the indenter contact depth. The slope of the indentation load-depth curve *dP/dh* was computed as the slope of a line tangent to (derivative of) the unloading curve. The creep compliance *J(t)* is defined as the change in the strain as a function of time under instantaneous applied constant initial load. The general mathematical formulation for viscoelastic constitutive models based on indentation via pyramid tip was developed by Giannakopoulos [55].

$$h^2(t) = \frac{\pi(1-\upsilon)}{4\tan\alpha}\int_0^t J(t-\delta)\left[\frac{dP(\delta)}{d\delta}\right]d\delta \tag{3.24}$$

where *h(t)* is nanoindentation depth varying with time, υ is Poisson's ratio, α represents the indenter surface angle with the vertical axis and *J* represents creep compliance under nanoindentation. Equation (3.24) can thus be used to describe the integration to obtain the time-dependent indentation depth *h(t)* as a function of the applied load *P*. Lu et al. [56] showed that the above integration can be solved by considering a constant loading rate $P(t) = \lambda_0\, t\, H(t)$ where λ_0 is a constant and $H(t)$ is the step function, or under a step loading in the form of $P(t) = P_0\, H(t)$ where $H(t)$ is the step function and P_0 is a maximum load. We will consider the case of dwell period loading (t = 60 seconds) to be divided into a ramp loading occurring at time period t_1 within a very short rise time (t_1 = 1

second), then a constant load afterwards for a time period t_2 = 59 seconds. Equation 3.25 can be re-written as

$$J(t) = \frac{4\,h^2(t)\tan\alpha}{\pi\,(1-\upsilon)P_0} \tag{3.25}$$

Where P_0 represents the maximum applied indentation load at which the load was kept constant. Equation (3.25) was used to calculate creep compliance of C-S-H and Figure 3.16 shows a schematic of the nanoindentation that was used for this technique.

Figure 3.15: Polishing apparatus for preparation on nanoindentation samples

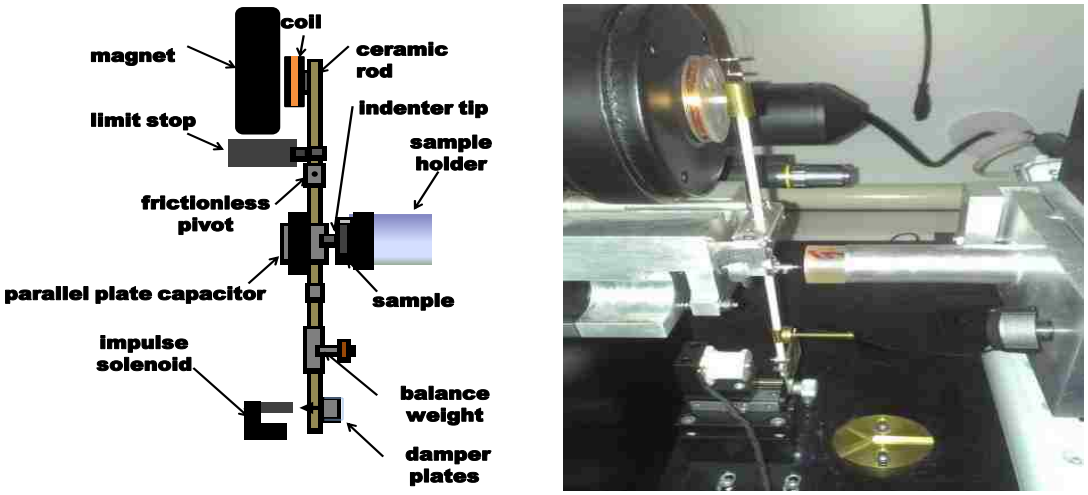

Figure 3.16: Schematic Diagram of the Nanoindentation components

3.7 Statistical Deconvolution Analysis

Statistical Deconvolution Analysis was conducted on both Nanoindentation and ^{29} Si MAS-NMR techniques. The object in using this analysis was to calculate an estimation of the volume fraction of the different phases in the final results observed in the decomposition to categorized the nanoindentation (stiffness) into a group of sub-microstructural phases of C-S-H. Two types of analysis were used to calculate the statistical deconvolution. The first technique was geared towards the ^{29} Si MAS-NMR analyses, where the MestReNova software was utilized. This software calculated the deconvolution for each C/S mixture ratio from 0.6 to 2.0. The second technique starts by determining a suitable bin size. This step is established by finding the difference between the maximum and minimum data points. It is then divided by the number of data points to find an initial bin size. Next, a histogram is configured from the data points. The bin size can be modified until an appropriate histogram is produced. Once way to established an ideal bin size is to know the number of phases expected to be present in the sample. In

calculating the number of bins required, equation 3.26 can be used to calculated as K = 3N-1, where N is the number of phases in the sample.

$$K = 3N\text{-}1 \tag{3.26}$$

The experimental density function (EDF) can be expressed in equation 3.27 where the frequency of each bin is applied.

$$\text{EDF} = \frac{f/K}{N} \tag{3.27}$$

where *f* denotes the frequency, *K* defines the bin size, and *N* is the number of data points. With this equation, an EDF point is calculated for each bin. At this point, the data is fitted into individual probability density functions (PDFs) and calculated using equation 3.28, where each phase is represented by its own PDF.

$$p(x_j) = \frac{e^{-\left(\frac{(x_j-\mu)^2}{2*\sigma^2}\right)*f_i}}{\sigma * \sqrt{2\pi}} \tag{3.28}$$

where, μ denotes the average value, σ is the standard deviation, and f_i represents the surface fraction where it is occupied by the *i-th* phase on the indentation surface. The standard error, *R*, lies between the EDF points and the PDF points where it shall be minimized. *R* can be computed as Equation (3.29):

$$R = \sum_{j=1}^{m} \frac{\left(EDF_j - p(x_j)\right)^2}{m} \tag{3.29}$$

EDF_j is defined as the value of the experimental density function at the *j-th* bin, $p(x_j)$ is denoted as the PDF value for the corresponding value of the *j-th* bin, and *m* signifies the number of bins used in the construction of the EDF. To correctly fit the PDFs to the EDF, *R* shall be minimized. Each PDF is adjusted to its applicable size by multiplying all points by the volume fraction of the corresponding phase. The standard deviation, mean, and volume fraction values are all repeated until *R* reaches its minimum value. Also, in the indented specimen, each PDF is defined as a representative of one of the phases it presents.

3.8 Brunauer-Emmett-Teller (BET) and Barrett-Joyner-Halena (BJH)

Brunauer-Emmett Teller (BET) N_2 technique was performed using the Quantachrome Autosorb-1 analyzer, measuring in nitrogen at 77k for each C/S mixture ratio specimens. This analysis primarily measures surface area from the physical adsorption/desorption of nitrogen gas on the solid surface. By this system, factors of specific surface areas, and pore size distribution could be controlled and the isotherm data can be obtained. Furthermore, the BJH method was applied to attain a pore size distribution for each specimen taken from the capillary condensation measurements. This technique is applicable to all types of porous materials to measure the pore size distribution. For this technique, approximately 50 mg of dried powdered C-S-H C/S mixture ratio specimens were placed in the physisorption tube and consolidated at the tube bulb. The physisorption tube was then attached to the Autosorb-1 testing apparatus and the cold trap was shifted into place over the physisorption tube. The testing was conducted under a liquid nitrogen temperature and measurement of the volume of the nitrogen being

absorbed every 10 hours was measured. The final step to finish the analysis ends with the outgassed overnight without heating the system. Figure 3.17 shows the Quantachrome Autosorb-1 analyzer system. The resultant values for the volume of nitrogen gas being adsorbed and the corresponding relative pressures were utilized to generate absorption isotherms. In literature and various researches, there are six different types of adsorption isotherms that are representative of many materials. Classification of the adsorption isotherm category permits specific conclusions to portray certain characteristics of the material being used [39]. Equation 3.30 defines the BET equation when applied to the isotherm shown as follow:

$$\frac{P}{V(P_0-P)} = \frac{1}{V_m C} + \frac{(C-1)P}{V_m C P_0} \tag{3.30}$$

where, V, is defined as the volume of absorbed vapor at pressure P (m^3 per gram of absorbent), V_m is designated as the volume of nitrogen gas adsorbed once the entire surface is covered by a monomolecular layer (m^3 per gram of adsorbent), C is denoted as the BET constant, P signified the pressure (N/m^2) and P_0 represents the saturation vapor pressure (N/m^2). This analysis is usually followed by a plot of $P/[P_0V\,(1 - P/P_0)]$ vs. P/P_0 that commonly specifies a straight line in the region of relative pressures near completed monolayers, which is considered the multipoint BET plot. Equation 3.31 defines the slope and intercept of the BET plot. From these values, Equation 3.32 can calculate to find the volume of gas adsorbed in a monomolecular, V_m, layer and the BET constant, C:

$$s = \frac{C-1}{V_m C} \qquad i = \frac{1}{V_m C} \tag{3.31}$$

$$V_m = \frac{1}{s+i} \qquad C = \frac{s}{i} + 1 \tag{3.32}$$

where *s* signifies the slope (g/m^3), *i* is expressed as the intercept (g/m^3). Once calculating, V_m, Equation 3.33 termed the specific surface are, *S*, can be obtain as the following:

$$S = \frac{V_m N_A A_m}{V_M} * 10^{-20} \tag{3.33}$$

where A_m is the average area occupied by one molecule of adsorbate in the completed monolayer (m^2/molecule), V_M is the molar volume (m^3/mol) and N_A is the Avogadro constant (molecules/mol.). Since this technique is operate under nitrogen, and used as the adsorbate, the specific surface area can be determined by the following equation 3.34:

$$S = \frac{(6.023*10^{23})(16.2*10^{-20})V_m}{22.4*10^{-3}} \quad or \quad S = 4.35V_m * 10^6 \left(\frac{m^2}{g}\right) \tag{3.34}$$

In the analysis of the BJH method, this technique was applied to the isotherm to produce a plot of pore volume against pore diameter. The physisorption software Autosorb was used to extract the data from the adsorption isotherm for the pore volume and pore radius data for this analysis.

Figure 3.17: 3.23 BET N2 testing system

3.9 Thermo Gravimetric Analysis (TGA)

Thermo Gravimetric Analysis (TGA) was performed in order to investigate the chemical composition of the varying calcium to silicate mixture ratio specimens. This technique identifies the calcium silicate hydrate (C-S-H), calcium hydroxide (CH) and calcium carbonate ($CaCO_3$) content determinants in the phase regions defined. The TGA/DSC model SDT Q600 shown in Figure 3.18 was used for this analysis. The test was performed from 25ºC to 1000 ºC, heated at 10 ^{o} C/min and purged with nitrogen flow of 60 ml/min. The results recording resolution was 0.001 ^{o}C. Investigations using TGA by other researchers have found that weight losses associated to the various ranges of temperatures categorized certain regions. Alonso and Fernandez [8] revealed the region up to 100ºC, free water is still presented in the sample. In the range of 100ºC to 250ºC,

the placement of loss water in the C-S-H is in effect. The section of 400ºC to 500ºC, portlandite can be found while from the temperature of 600ºC to 750ºC, Calcite is defined with the decomposition of a weak endothermic peak at 650ºC. In analyzing the data, the initial mass is taken at 145ºC. At the temperature range between 145 ºC and 350 ºC, the mass loss is denoted as $\%mL_1$ where this region is considered to be the loss of water from C-S-H. From the temperature range between 350 ºC to 500 ºC, it is defined as the loss of water from CH and is denoted as $\%mL_2$. Loss of carbon dioxide (CO_2) from $CaCO_3$ is defined as $\%mL_3$ and is located in the region between the temperate ranges of 600 ºC to 825 ºC. Once the determination of the content of CH and $CaCO_3$, the remaining is defined as C-S-H where the denotation can be used in the following Equation 3.35 and 3.36 to calculate the stoichiometric formula of the C-S-H [35].

$$\text{C/S} = \frac{\overline{C/S}(100-\%mL_1-4.113\%mL_2-2.274\%mL_3)-3.336\%mL_2}{100-\%mL_1-\%mL_2-2.274\%mL_3} \quad (3.35)$$

$$x = \frac{\%mL_1\left(3.115\overline{(C/S)}+3.337\right)}{100-\%mL_1-\%mL_2-2.274\%mL_3} \quad (3.36)$$

where the molecular weight of H_2O, CH, CO_2, $CaCO_3$ and C-S-H as 18.01 g/mole, 74.1 g/mole, 44.01 g/mole, 100.09 g/mole, and 56.1 (C/S)+ 60.1 g/mole + ((18.01)* *x)* g/mole are used for the derivation of the equation above with the assumption that when the initial C/S mixture ratio of $\overline{\boldsymbol{C/S}}$ is mixed with enough deionized water, 1 mole of C-S-H and ($\overline{\boldsymbol{C/S}}$-C/S) mole of CH will be synthesized. Results of varying C-S-H mixture ratio will be discussed in detail in chapter 4.

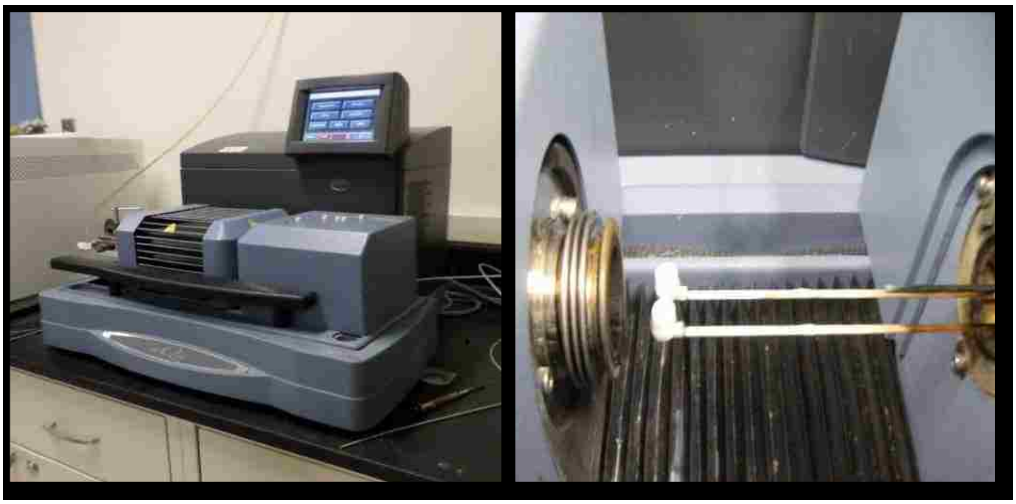

Figure 3.18: TGA/DSC SDT Q600 apparatus, and specimen holder.

3.10 X-Ray Diffraction Analysis (XRDA)

X-Ray diffraction (XRD) is a method in cement chemistry to characterize crystalline materials and detect various chemicals in compound. X-ray patterns are a distinctive "fingerprint" for each material; however, measuring the structure of C-S-H in Portland cement system is limited due to its poorly crystalline nature. Utilizing this test method, comparing results to prior outcomes can lead to confirmation of the formation of C-S-H since resultant pattern of the specimen does not change or alter with repeating testing nor does it change with different sample on the same material. In this particular technique, the Rigaku Smartlab system with a powder diffractometer using a CuKα radiation and a wavelength, $\lambda = 0.154$ nm was used to record the XRD data. Approximately, 20 grams of dried powdered C-S-H specimens of each C/S ratio were inserted into the testing mount and process individually. The operation of this system functioned under the open attenuator of 40 kV and 40 mA with an optimization for scattering angles, θ, of $2^{o}<\theta<90^{o}$.

In a crystalline material, the atomic structure are format in a repeating order and can produce similar atomic patterns, as well as using Bragg's Law to calculate the diffraction of X-Rays as shown in Figure 3.19 **(a)** and **(b)** .

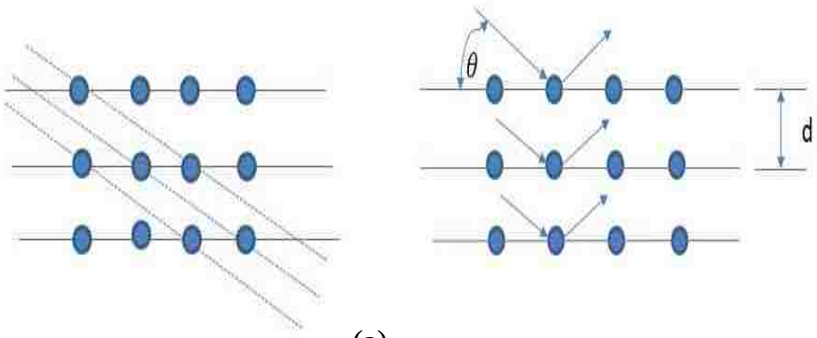

(a) (b)

Figure 3.19: (a) Crystalline structure of atomic planes (b)Bragg's Law diffractive x-rays

Where Equation 3.37 is the definition of Bragg's Law which expresses the relationship between the d-spacing, *d* and the angle of the diffraction *θ*:

$$\lambda = 2dsin\theta \tag{3.37}$$

where λ = to the wave length (nm) and *d* is the *d*-spacing, and Θ is the diffraction angle in degrees. In addition, using the software MDI Jade 2010 version 2.1.6 and the ICPP Powder Diffraction Database Release 2012, a full feature analysis of the XRD processing was used to determine the chemical phases such as calcium hydroxide shown in Figure 3.20 .

Figure 3.20: Rigaku SmartLab XRD testing system

3.11 29 Si Magic Angle Spinning Nuclear Magnetic Resonance (NMR)

^{29}Si MAS-NMR is used for analyzing the silicate connectivity and polymerization of silica-based compounds and has been recognized as an effective technique for investigating chemical bonding for hydrated cement and/or synthetic calcium silicate hydrate (C-S-H). The interpretation of the ^{29}Si NMR spectrum provides identification of the polymerization of a silicate tetrahedron where Q represents the silicate tetrahedron bonded and the numbers, n, is defined as the shard oxygen (Q^n). Thus, Q^0 denotes the monomeric orthosilicate anion, SiO_2^{4-} and the typical anhydrous silicate of cement: tricalcium silicate (C_3S) and dicalcium silicate (C_2S). Additionally, the Q^1 represents the end-chain group of C-S-H, Q^2 signifies the middle chain group while Q^3 embodies the chain-branching site. Q^4 connection is a three dimensionally fully cross linked group that represents the polymerization of quartz and can be found in silica rich products such as fly ash and silica fume. In this method, ^{29}Si Magic Angle Spinning Nuclear Magnetic Resonance (^{29}Si MAS-NMR) spectroscopy was implemented using a 7 mm Bruker®

rotor and cryomagnet (BZH 300/89) spectroscopy for all NMR testing. Prior to testing, fine powder C-S-H specimens were packed into the 7 mm rotor with attentiveness to ensure the compaction was approximately two thirds from the top of the container to enable the cap to be fitted tightly. Subsequently, the rotor was wiped clean and marked before placing it into the cryomagnet. While prepping the sample for testing, the testing apparatus was calibrated with a ^{29}Si standard to have a reference for comparisons. Once the calibration and preparation of the sample were completed, the solid-state NMR method was performed with approximately 10,000 scans were conducted on each specimen where TopSpin™ data acquisition software was executed for each test. In analyzing the NMR, the chemical shift depends primarily on the neighboring silicate connections that effect this modification and requires a statistical deconvolution analysis of the of ^{29}Si MAS NMR spectra to classify the chemical shift peaks for the silica polymerization type Q^0, Q^1, Q^2, Q^3, and Q^4. Using Saoût et al [57] referenced to the calculated intensity fraction of the Q^n's, the average degree of C-S-H connectivity, N_c, is expressed in Equation 3.38 while Equation 3.39 calculates the degree of hydration, D_h for hydrated cement paste as follows:

$$N_c = \frac{Q^1+2Q^2+3Q^3}{Q^1+Q^2+Q^3} \tag{3.38}$$

$$D_h = Q^1 + Q^2 + Q^3 \tag{3.39}$$

High polymerization of C-S-H is apparent when the D_h values are high. Furthermore, calculating the number of silicate bound together in a chain is calculated using the Equation 3.40 where it is defined as the mean chain length, L.

$$L = 2(1 + \frac{Q^2}{Q^1}) \tag{3.40}$$

where this chain is typically found in the $\frac{Q^2}{Q^1}$ ratio in naturally occurring calcium silicate hydrate expressed by Taylor [2].

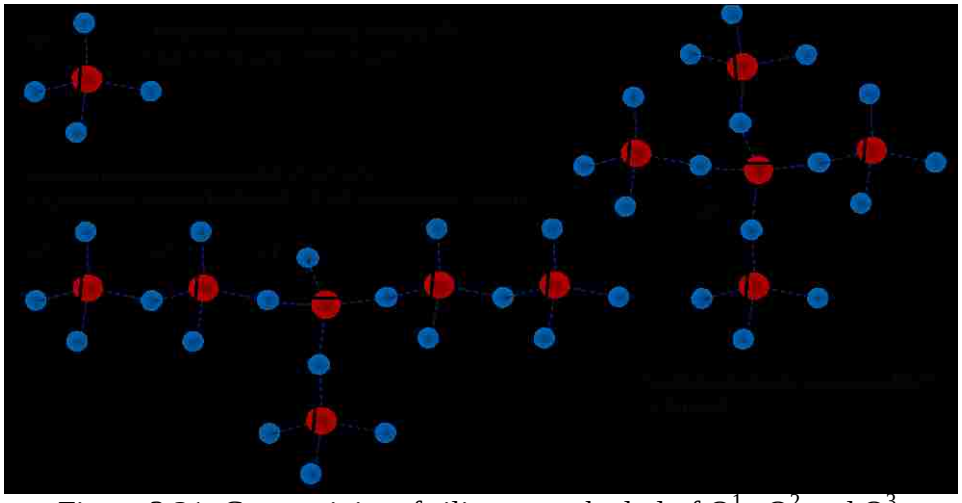

Figure 3.21: Connectivity of silicate tetrahedral of Q^1 , Q^2 and Q^3.

3.12 Transmission Electron Microscope (TEM)

Transmission Electron Microscope (TEM) was measured by using a JEOL 2100F Transmission Electron Microscope at an accelerating voltage of 200 kV shown in Figure 3.22. Measurements were conducted by preparing the samples in a dilute particle-Ethanol colloidal mixture in which was ultra-sonicated for 15 minutes and a drop of solution was placed on a carbon-coated Cu TEM grid. After drying the specimen, the grid was connected to the TEM apparatus and measurements were recorded.

Figure 3.22: JEOL 2100F Transmission Electron Microscope apparatus.

3.13 Scanning Electron Microscope

SEM was utilized to study the morphology of C-S-H using a Hitachi S-5200 Scanning Electron Microscope (SEM) shown in Figure 3.23. This device has a magnification rate ranging from 100x to 2,000,000x with a resolution of 2.0 µm at 1 kV and 2 kV. Non-coated samples were placed on specimen holder arm using double sided tape for imaging.

Figure 3.23: Hitachi S-5200 Scanning Electron Microscope apparatus.

Chapter 4 Results and Discussion

4.1 C-S-H Compaction

In investigating the dynamic modulus analyzer, bulk modulus of elasticity, bulk density, and nanoindentation, a rigid specimen is required. Therefore, in this research, it is necessary to compact the fine powder specimens of C-S-H for each selected C/S mixture ratios to determine the mechanical properties. In section 4.1.1 through 4.1.4 presents the calculated bulk modulus of elasticity resulted from the compaction curve for 0.7, 1.5, and 2.0 with a graphical comparison between these ratios. These selected ratios represent the overall categories of LD C-S-H and HD C-S-H sections mentioned in previous literature, as well as the region where C-S-H typically is found in Portland cement paste, C/S mixture ratio of 1.5.

4.1.1 0.7 C/S C-S-H

Table 4.1 displays the calculated bulk modulus of elasticity (E_b) for each compacted specimens that was obtained using Equation 3.2 where the loading-unloading pressure-displacement curves for 0.7 C/S mixture ratios are shown graphically in Appendix A. In observing the 0.7 C/S mixture ratio bulk modulus of elasticity, there is a trend signifying the increases as the compaction pressure increases from 200 to 500 MPa where it starts from 67.6 to 216.8 GPa, respectively. It is noted that 0.7 C/S C-S-H mixture ratio has been found to be more porous than 1.5 and 2.0 C/S C-S-H. This porosity allows the material to become stiffer or more compacted as the pressure increases as shown in the calculation values found in the Table below.

Table 4.1 Calculation of the bulk elastic modulus for 0.7 C/S C-S-H

C/S ratio	Pressure (MPa)	S_t (N/mm^3)	t_f (mm)	t_r (mm)	E_b (GPa)
0.7	200	5,934	13.26	1.86	67.6
	300	6,558	13.26	1.78	75.3
	400	7,897	13.26	1.82	90.3
	500	18,746	13.26	1.69	216.8

4.1.2 1.5 C/S Mixture Ratio

The curves for the loading-unloading pressure-displacement of 1.5 C/S mixture ratios are shown in Figure 4.2 with varying pressure from 200MPa to 500 MPa. Table 4.2 presents the calculated bulk modulus of elasticity (E_b) where the compacted specimen was achieved. As can be observed in Figure 4.2, the trend of 1.5 C/S C-S-H increases in displacement with increasing pressure, as well, as the bulk modulus of elasticity, indicating a higher deformation at 200 MPa compared to 500 MPa. It is noted that upon previous research, Boumiz [58] measured the elastic modulus of compacted powder of tri-calcium silicate (C_3S) by acoustic method to be equal to 117 GPa while Granju [59] measured clinker on polished blocks to be in the range between 60 and 300 GPa. It is stated in previous research that Portland cement paste is similar to the range of 1.5 to 1.7 C/S mixture ratio synthetically and the comparison of the elastic modulus of elasticity shows a trend from 47.6 GPa to 497.1 GPa. In observation, the results of 1.5 C/S C-S-H is consistent with previous literature.

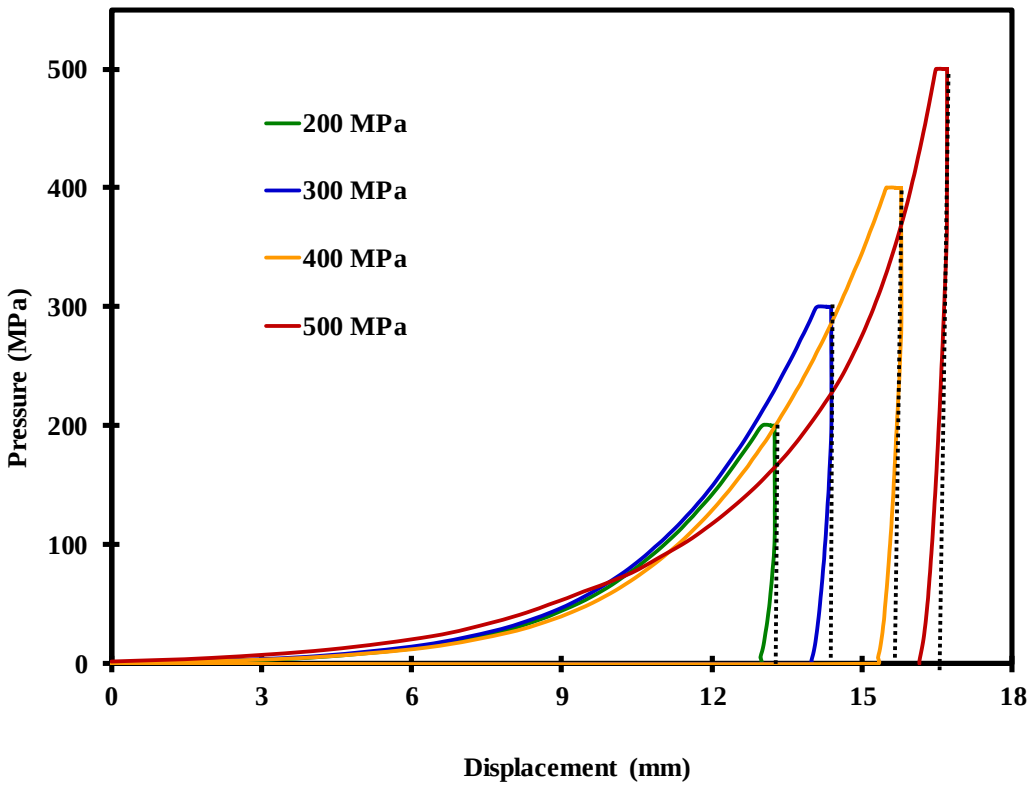

Figure 4.1: 1.5 C/S Mixture Ratio Loading – Unloading Curves

Table 4.2 Calculation of the bulk elastic modulus for 1.5 C/S C-S-H

C/S ratio	Pressure (MPa)	S_t (N/mm^3)	t_f (mm)	t_r (mm)	E_b (GPa)
1.5	200	13,271	8.45	1.73	89.1
	300	15,988	8.45	1.81	106.1
	400	30,071	8.45	1.77	200.8
	500	73,909	8.45	1.72	497.1

4.1.3 2.0 C/S Mixture Ratio

The loading-unloading pressure-displacement curves for the 2.0 C/S mixture ratio can be found in Appendix A while the calculated results are presented in Table 4.3 where, E_b, is found to be 253.9 to 624.7 GPa for the pressure ranging from 200 to 500 MPa. In examining the calculated results, the trend from a low pressure to a high pressure

coincides with the increasing modulus of elasticity. The results from the pressure of 500 MPa will be compared to 0.7 and 1.5 C/S C-S-H in section 4.1.4.

Table 4.3 Calculation of the bulk elastic modulus for 2.0 C/S mixture ratio

C/S ratio	Pressure (MPa)	S_t (N/mm^3)	t_f (mm)	t_r (mm)	E_b (GPa)
2	200	137,492	3.68	1.83	253.9
	300	170,536	3.68	1.8	320.0
	400	214,999	3.68	1.79	405.6
	500	329,080	3.68	1.77	627.4

4.1.4 0.7, 1.5, and 2.0 C/S Mixture Ratio

It was presented in Figure 3.7 that Alizadeh [44] introduced the porosity of compacted C-S-H, where it shows that at the pressure of 500 MPa simulate C-S-H porosity of concrete at specific w/c ratio. It is this reason; the selection of 500 MPa was investigated and analyzed in a comparative analysis of both compaction curve of the loading-unloading pressure-displacement curves for the C/S mixture ratio of 0.7, 1.5, and 2.0 C/S mixture ratio as shown in Figure 4.3. Graphically, it shows a trend of increasing displacement as the ratio of C/S mixture increases from 0.7 to 2.0. This shows that 0.7 C/S C-S-H has a higher porosity than 2.0 and concludes that 1.5 C/S C-S-H compaction showed values expected from prior literature.

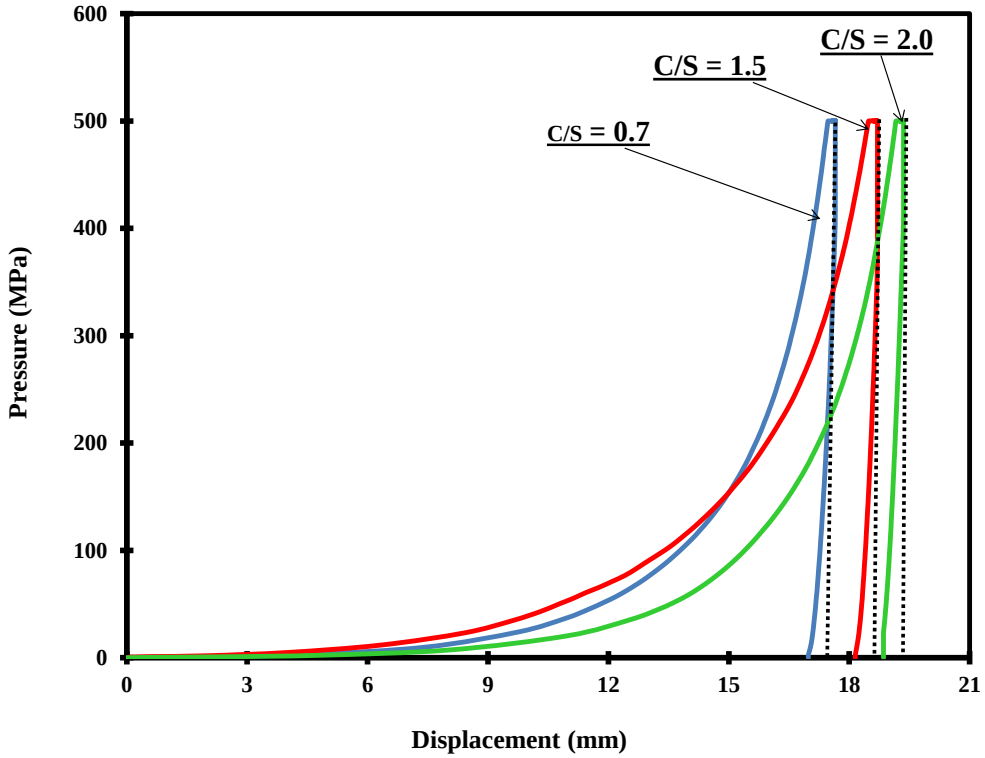

Figure 4.2: Comparison of 0.7,1.5, & 2.0 C/S Mixture Ratio Loading–Unloading Curves

Table 4.4 Bulk elastic modulus for 0.7, 1.5, and 2.0 C/S C-S-H at 500 MPa

C/S ratio	S_t (N/mm^3)	t_f (mm)	t_r (mm)	E_b (GPa)
0.7	18,746	13.26	1.69	216.8
1.5	73,909	8.45	1.72	497.1
2	329,080	3.68	1.77	627.4

4.2 Bulk Density

Bulk density has been determined in accordance to ASTM Standard C 914-95 [51] where five specimens of each C/S mixture ratio of 0.7, 1.5, and 2.0 C-S-H were cut into 20 pieces with the same dimensions for each ratio. Figure 4.3 shows the comparisons graphically between each ratio with the difference pressures, ranging from 200 to 500 MPa. As one can observe, the 0.7 C/S C-S-H has a lower density than the 1.5 and 2.0

C/S. Comparing 1.5 and 2.0 C/S mixture ratio, 2.0 C/S C-S-H is slightly higher at the pressure of 200 MPa and gradually increases with the pressure. This analysis concurs with previous research conducted by Foley et al [7] and Kim et al [55] where the C/S mixture ratios increased in both pressure and mixture ratios.

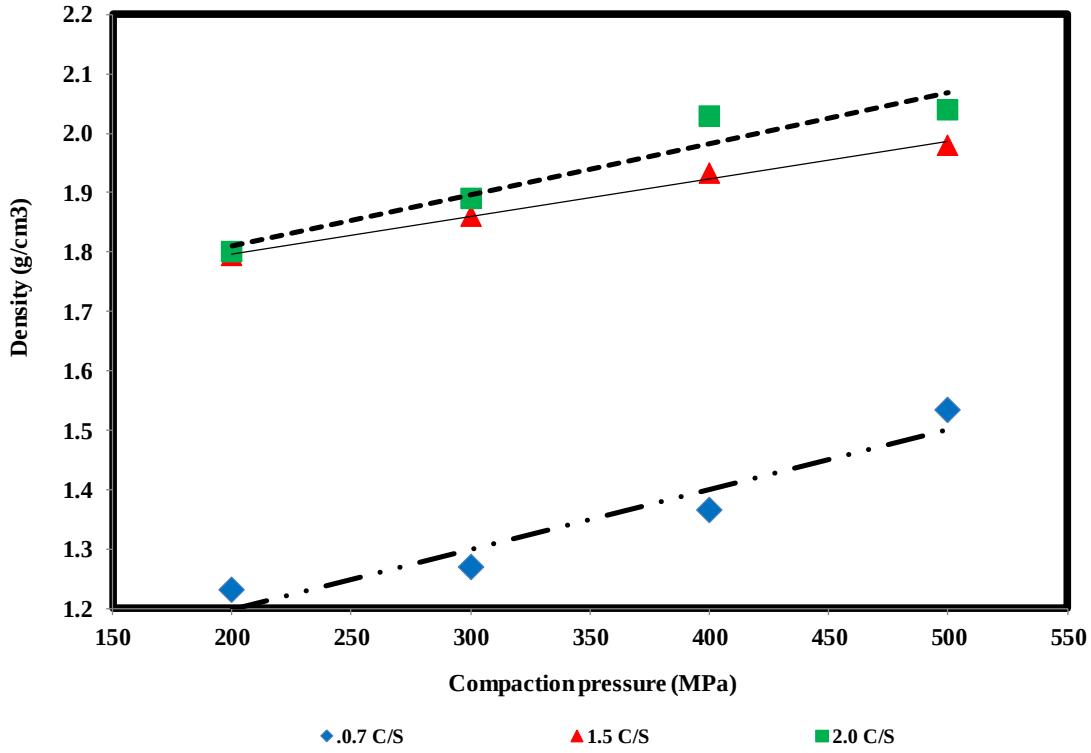

Figure 4.3: 0.7, 1.5, and 2.0 C/S Mixture Ratio Density vs Compaction pressure

Table 4.5 Calculation of the bulk elastic modulus for 0.7, 1.5, and 2.0 C/S mixture ratios

Compaction pressure	0.7 C/S		1.5 C/S		2.0 C/S	
	Density (g/cm^3)	COV	Density (g/cm^3)	COV	Density (g/cm^3)	COV
500	1.53	0.01	1.98	0.01	2.04	0.02
400	1.37	0.03	1.93	0.03	2.03	0.03
300	1.27	0.03	1.86	0.04	1.89	0.04
200	1.23	0.04	1.79	0.05	1.8	0.05

4.3 Dynamic Modulus Analyzer

Following the compaction of 0.7, 1.5, and 2.0 C/S mixture ratio, the specimens has been tested to determine the mechanical properties using the Dynamic Modulus Analyzer also known as the Dynamic Mechanical Analysis. In this technique, it allows for examination of both the elastic and viscoelastic properties of C-S-H. Although the analysis was conducted from 1 Hz to 3 Hz, only the 1 Hz was analyzed and compared as shown in Figure 4.4 through Figure 4.7 for the storage modulus and tan delta. It was found that there was little to none in difference for frequencies from 2 Hz to 3 Hz for each sample. In addition, the last five seconds was analyzed for each specimen to measure the elastic effect in Figure 4.5.

This analysis for the macro C-S-H of 0.7 and 1.5 C/S ratio show similar behavior in storage modulus; however, adding more CaO and reaching to 2.0 C/S C-S-H exhibits a trend change and the stiffness get higher as shown graphically in Figure 4.5. In investigating the Tan Delta, the determination of damping (creep) or energy loss in viscoelastic materials were measured in the C/S mixture ratio of 0.7, 1.5, and 2.0 C-S-H where it is established that the materials with higher tan delta are materials with higher creep. Numerically, tan delta is the ratio between the loss modulus/storage modulus or the loss compliance/storage compliance. In analyzing Figure 4.6 and 4.7, the macro C-S-H of 0.7 has a lower creep than 1.5. This may have been determined by the fact that 0.7 C-S-H materials are found to very stiff. In addition, the difference between 0.7 and 1.5 in macro creep does not seem to be significant in difference where it matches the observation in storage modulus analysis. Correspondingly, the 0.7 C/S C-S-H is stiffer

and has less creep but this variance at the macro scale are not substantial. Conversely, adding more CaO and reaching to 2.0, this development changes and creep gets significantly lower. In observing the 2.0 C/S C-S-H in Figure 4.6, the very low creep matches the measurement of its very high stiffness.

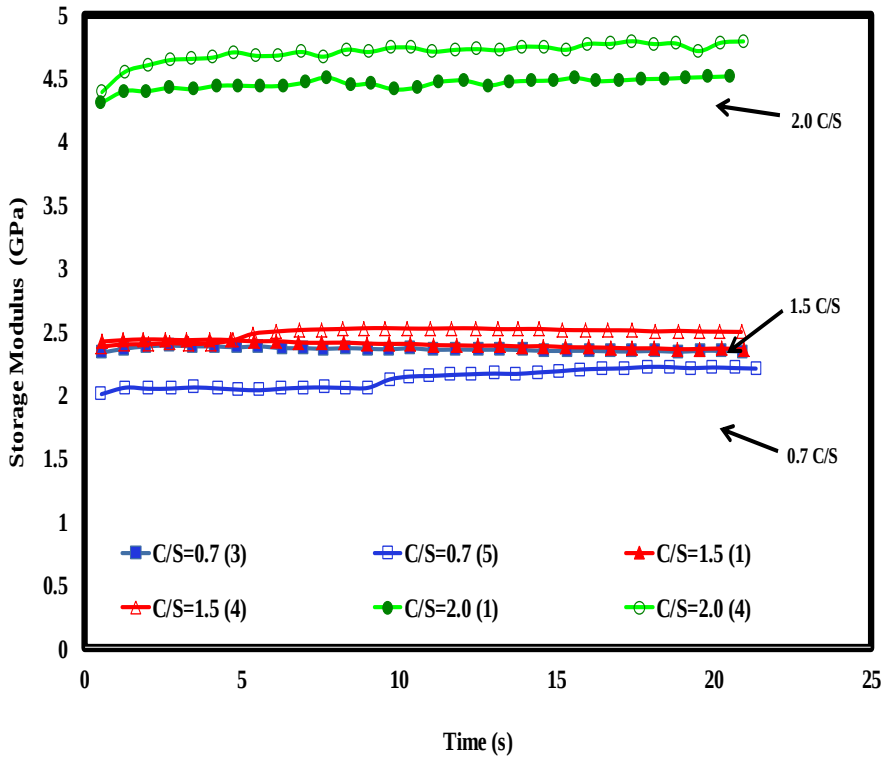

Figure 4.4: 0.7, 1.5, and 2.0 C/S Mixture Ratio Storage Modulus Comparative of 1 Hz

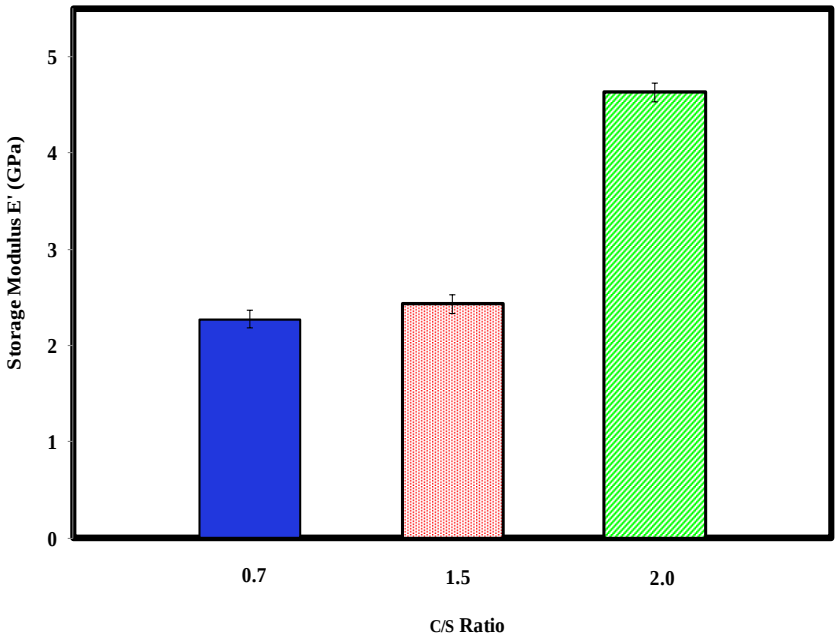

Figure 4.5: Graphical Figure of 0.7 – 2.0 C/S C-S-H of Storage Modulus

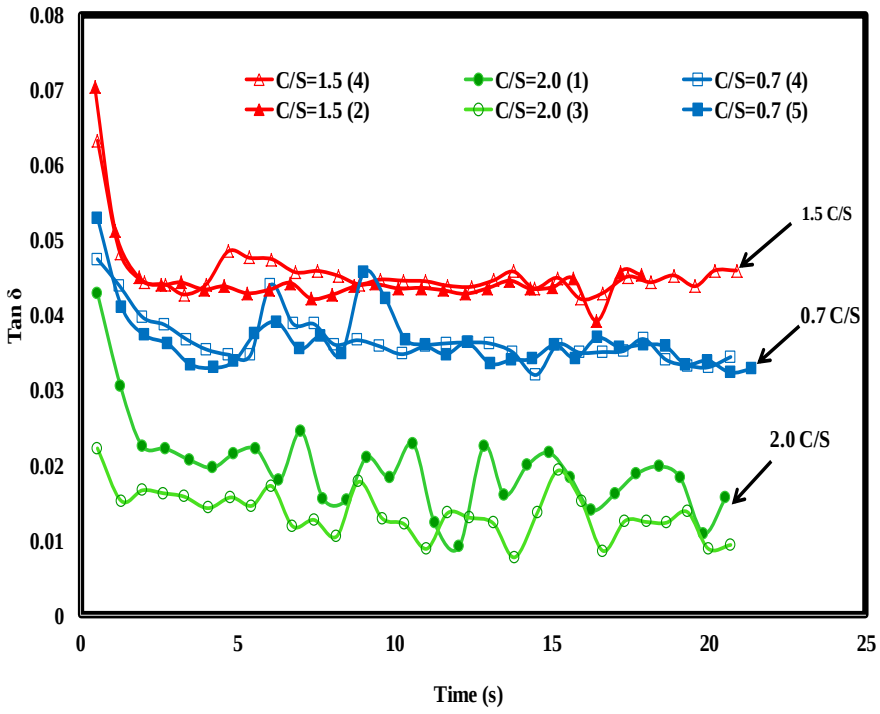

Figure 4.6: 0.7 C/S C-S-H Internal Friction, Tan δ

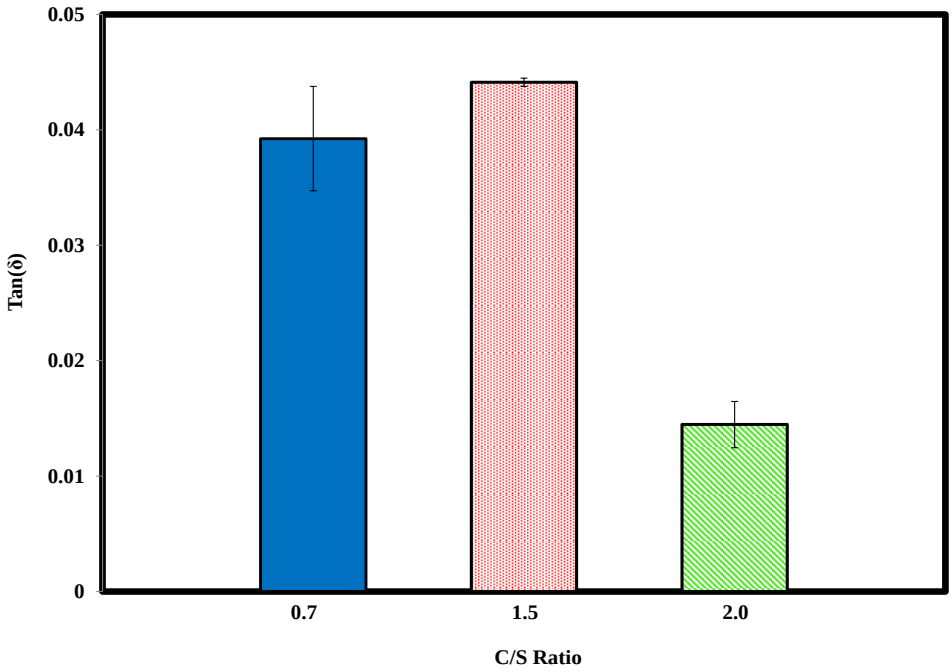

Figure 4.7: 2.0 C/S C-S-H Internal Friction, Tan δ

4.4 Nanoindentation

Nanoindentation data was analyzed using the method described in Chapter 3. Figure 4.9 shows a comparison of the average reduced elastic modulus while Figure 4.10 displays the creep compliance of the two types of C/S mixture ratio of 0.7 and 1.5 C-S-H. It is observed from the reduced elastic modulus that C-S-H made with low C/S mixture ratio of 0.7 has average elastic modulus higher than that C-S-H made with high C/S mixture ratio of 1.5. Furthermore, the results in Figure 4.10 show that C-S-H made low C/S mixture ratio of 0.7 has average creep compliance lower than that C-S-H made with high C/S mixture ratio of 1.5. The statistical variation between the nanoindentation observations in both materials is considerable high and when the observed difference statistically insignificant. This wide variation can be attributed to the existence of many

submicron C-S-H phases. This necessitates conducting statistical deconvolution analysis to understand any modification that result in the observed mechanical characteristics. Figure 4.11 and Figure 4.12 exhibits a comparison of the statistic deconvolution analysis after Contantinedes and Ulm [42]. It is obvious that C-S-H with low C/S mixture ratio incorporates a higher fraction of high density phases that may possibly be high density C-S-H or CH crystals. In Table 4.6 shows the elastic moduli for each individual identified phase and sized relative to their relative surface fraction for each compaction pressure.

Table 4.6 : Surface fractions and Young's Modulus compacted at 500 MPa for 0.7 % 1.5 C/S C-S-H

C/S Mixture Ratio	0.7 CSH Phase Categorization	Surface Fraction	Young's Modulus (GPa)	Weighted Average Young's Modulus (GPa)
0.7	VLD-CSH	2%	10 ± 4	156.0
	LD-CSH	20%	26 ± 7	
	HD-CSH	44%	50 ± 10	
	VHD-CSH	34%	70 ± 9	
1.5	VLD-CSH	45%	9 ± 3	117.0
	LD-CSH	30%	17 ± 5	
	HD-CSH	15%	35 ± 7	
	VHD-CSH	10%	56 ± 5	

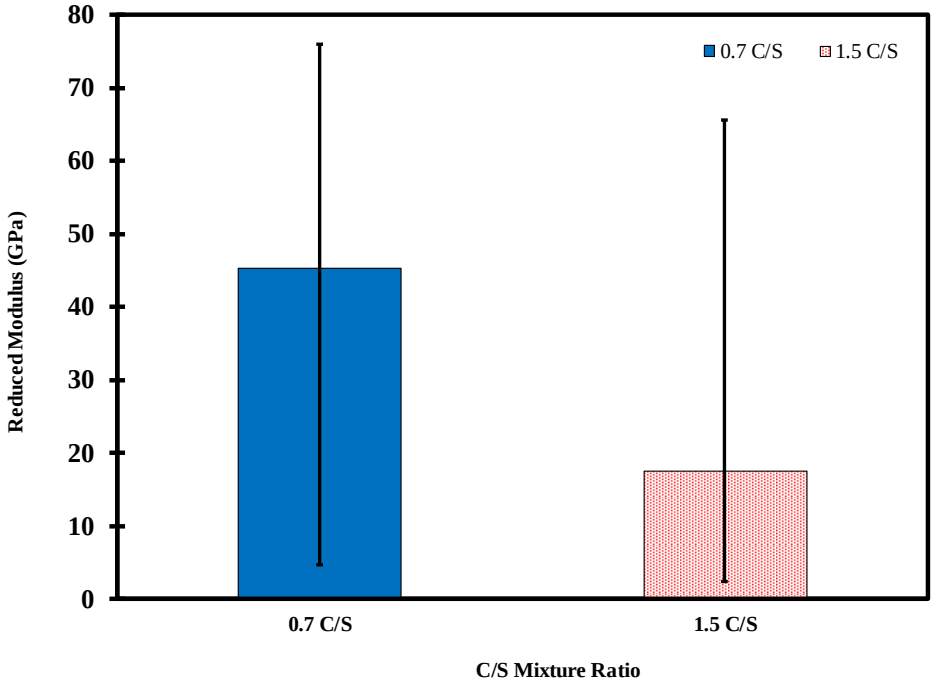

Figure 4.8: 0.7 and 1.5C/S Mixture Ratio Reduced Modulus

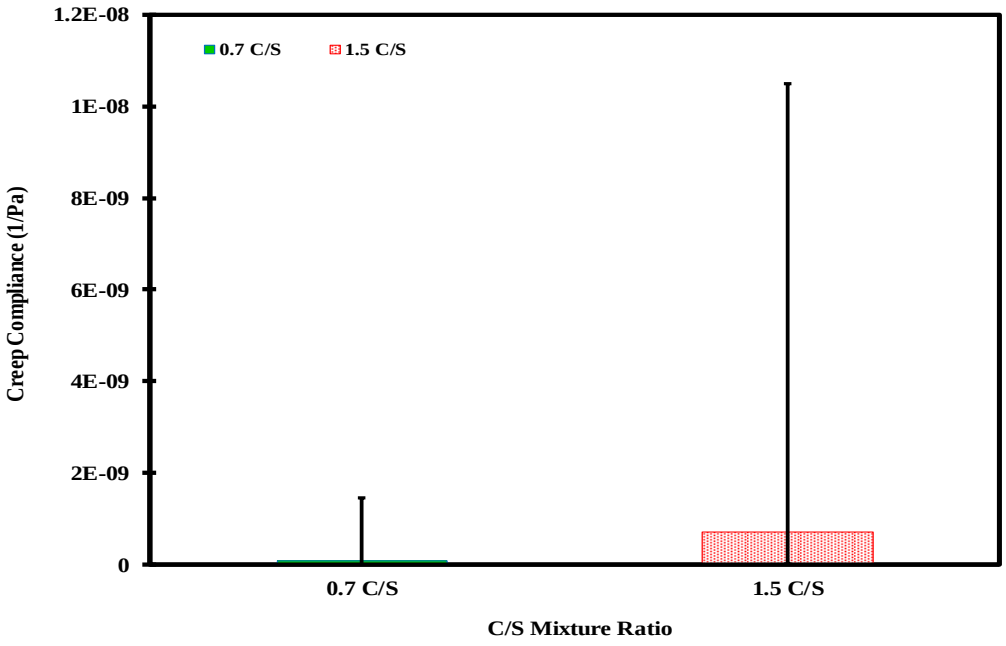

Figure 4.9 : 0.7 and 1.5C/S Mixture Ratio Creep Compliance

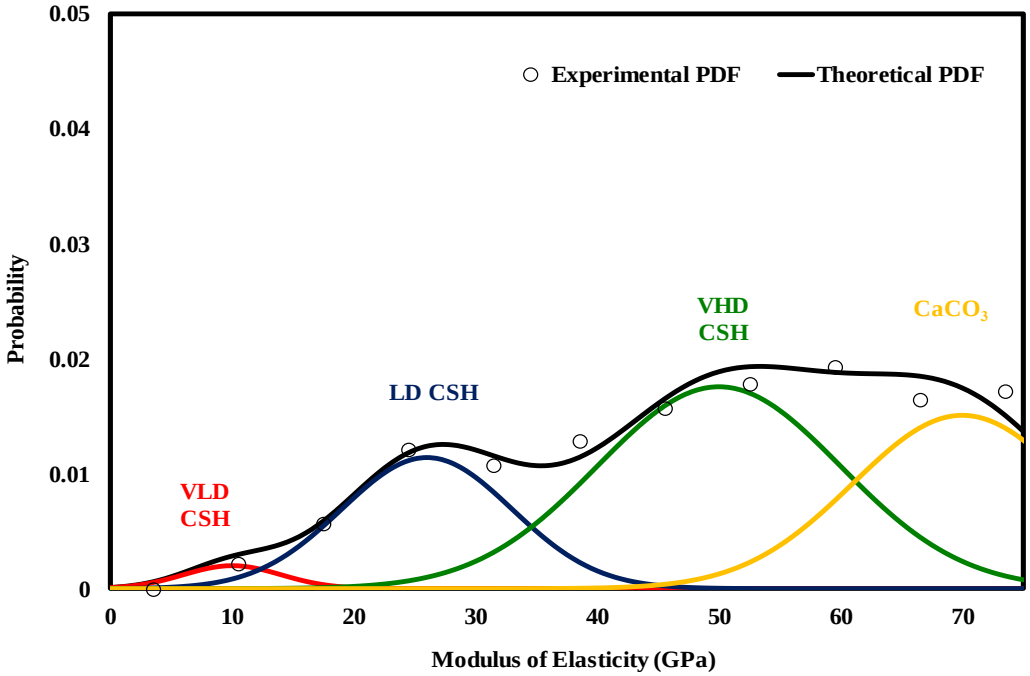

Figure 4.10: 0.7 C/S C-S-H Statistic Deconvolution Analysis

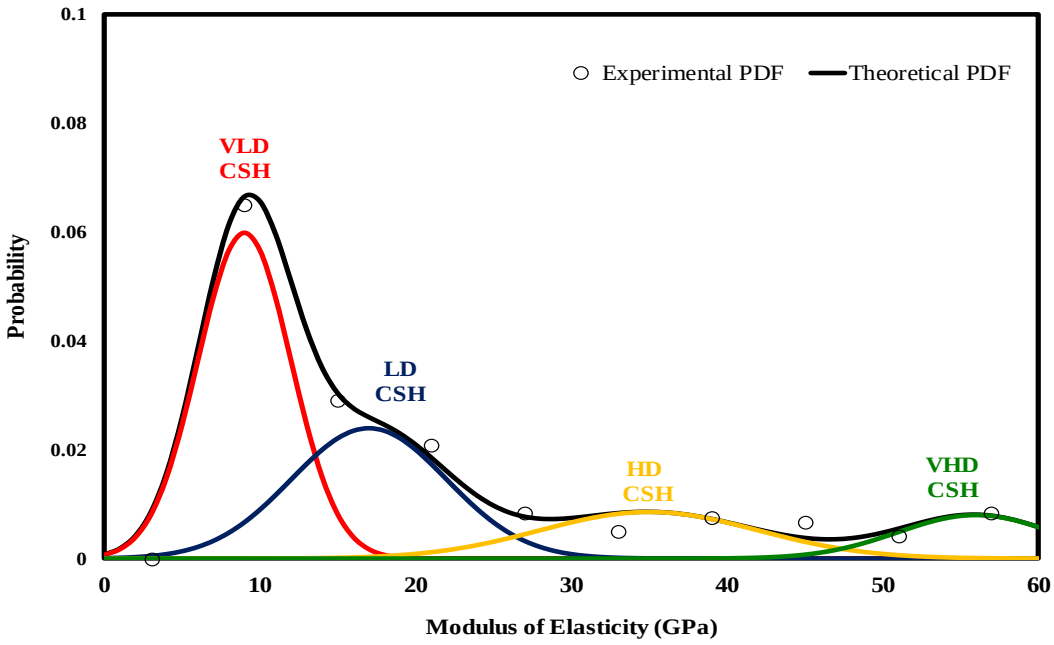

Figure 4.11: 1.5 C/S C-S-H Statistic Deconvolution Analysis

4.5 Specific Gravity

Specific Gravity has been determined in accordance to ASTM Standard C 188-09 [50]. In this technique, 1 gram of each C/S mixture ratio of 0.7, 1.5, and 2.0 C-S-H was used to determine the particle density of C-S-H where it shown that the 0.7 C/S ratios have a lower density than 1.5 and 2.0 C/S C-S-H. Figure 4.8 shows the comparison between the ratios where it shows 0.7, 1.5, and 2.0 C/S C-S-H has a density of 1.32, 1.48, and 2.04 g/cm^3. This coincides with the bulk density and confirms that the 0.7 C/S mixture ratios has a higher porosity and a higher volume voids out to the three. This also corresponds to the literature where the density of C-S-H has been found to be approximately 2.604 g/cm^3 and its chemical formula defined as $(CaO)_{1.7}(SiO_2)(H_2O)_{1.8}$.

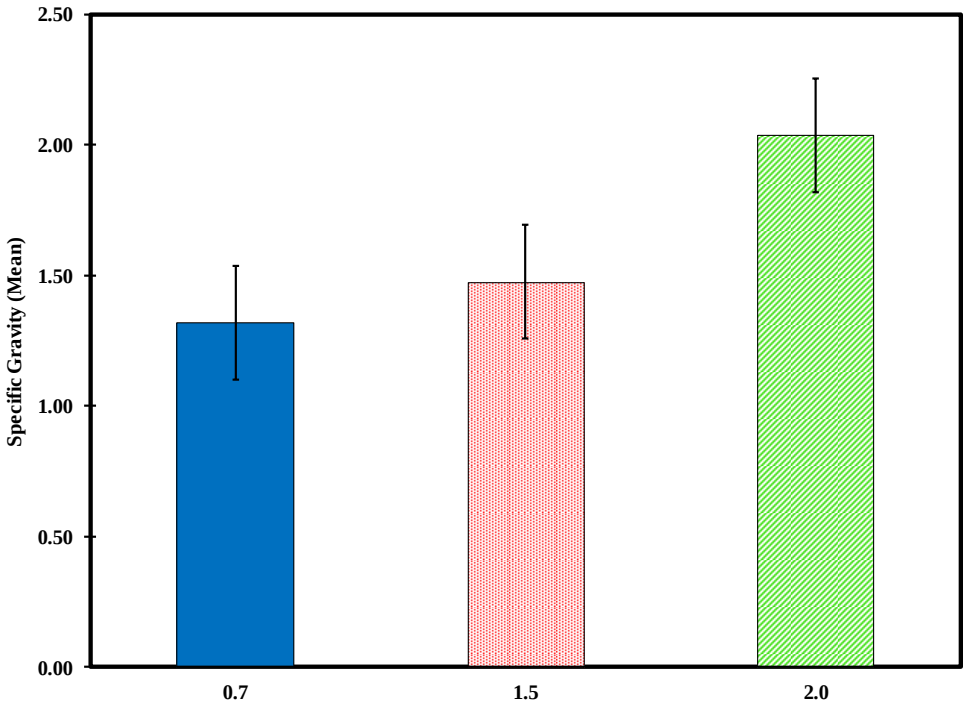

Figure 4.12: 0.7, 1.5, and 2.0 C/S Mixture Ratio Specific Gravity

4.6 Brunauer-Emmett-Teller (BET) and Barrett-Joyner-Halena (BJH)

Specific surface computed by BET method is comparable for all C/S mixture ratios. In observing the lower region of the mixture ratio, 0.7 C/S has a higher porosity as opposed to 0.6 C/S mixture ratio. This may be due to the preparation of the specimen; however, there are several possible explanations for this occurrence. Figure 4.13 through Figure 4. 17 show the volume adsorpted versus the Relative Intensity. For all specimens, it can be classified as Type IV pore structure where it shows good pore connectivity. The N2 isotherms show type H3 hysteresis loop indicating plate like particles giving rise to slit – shaped pores.

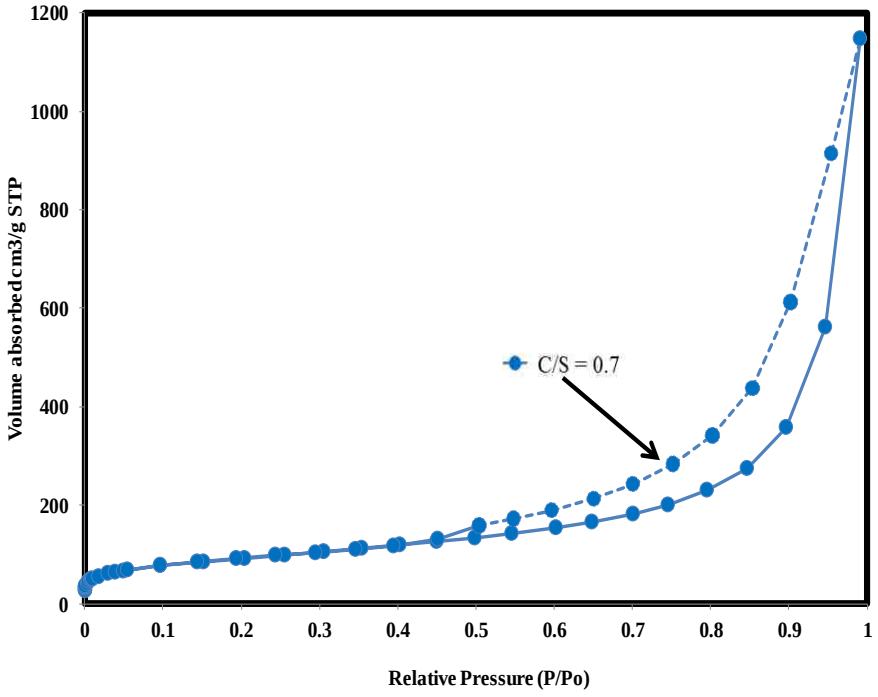

Figure 4.13 BET Analysis of 0.7 C/S Mixture Ratio

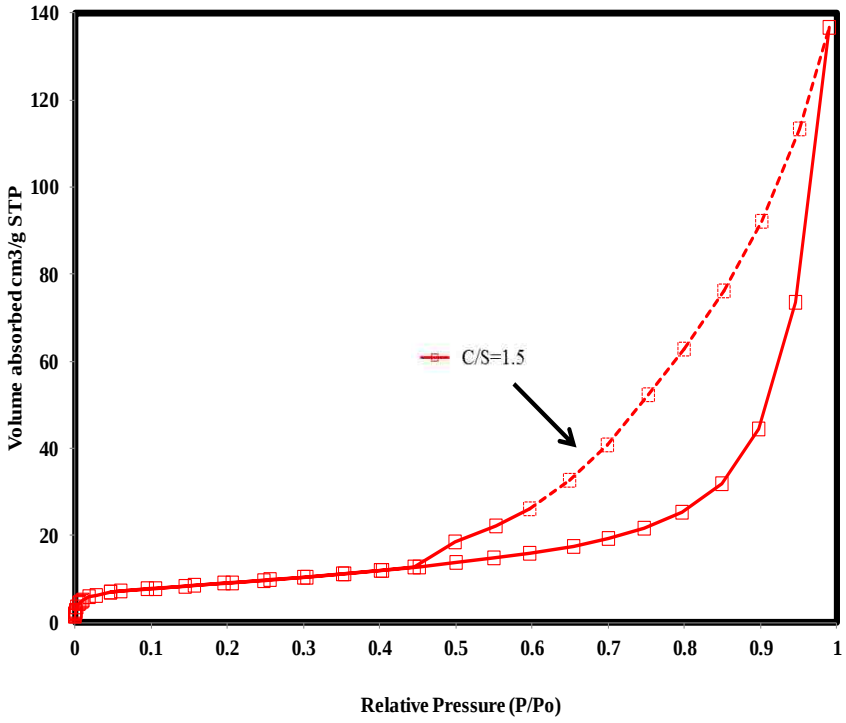

Figure 4.14 BET Analysis of 1.5,C/S Mixture Ratio

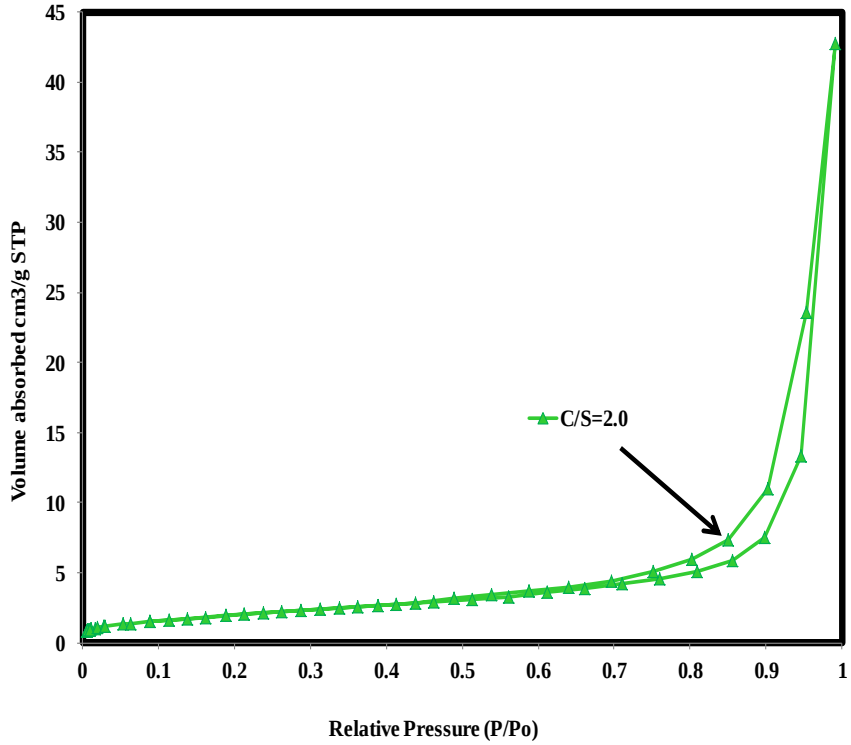

Figure 4.15 BET Analysis of 2.0 C/S Mixture Ratio

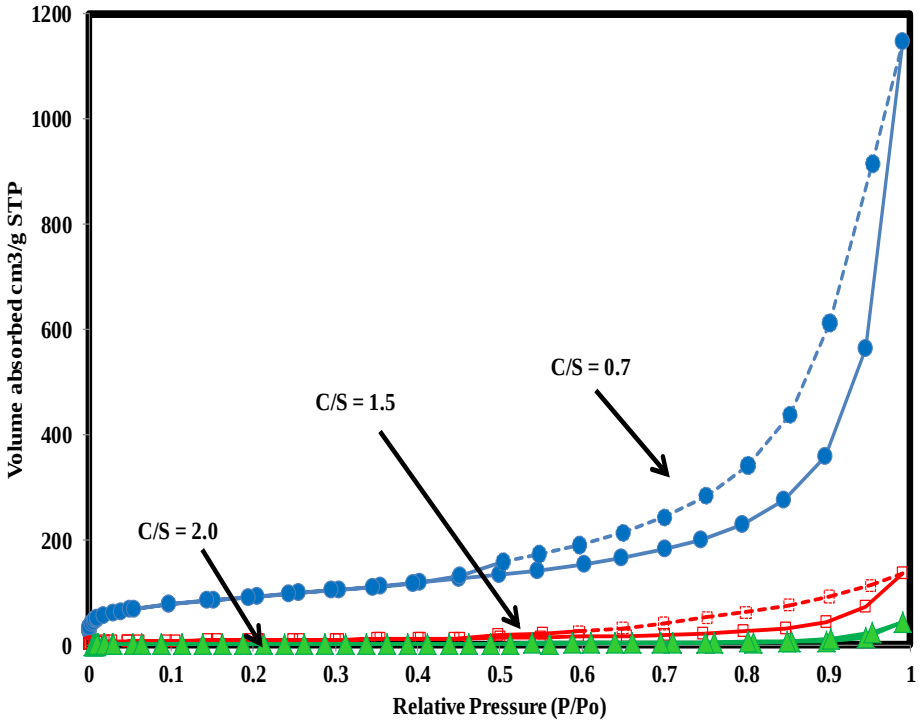

Figure 4.16 BET Analysis of 0.7, 1.5, and 2.0 C/S Mixture Ratio

4.7 Thermo Gravimetric Analysis (TGA)

TGA tests were performed from 25 °C to 1000 °C, heated at 10 °C/min. The temperature range where water began to dissociate from the C-S-H between 125 °C and 145-150 °C was observed in this research. The mass losses at the temperature ranges from 145 °C to 400 °C, from 400 °C to 600 °C and from 600 °C to 825 °C are recognized as the dehydration of C-S-H, the dehydroxylation of calcium hydroxide and the decarbonization of calcite respectively. TGA curves for the synthetic C-S-H with varying C/S mixture ratio ranging from 0.6 to 2.0 are shown in Figure 4.17 and 4.18. To exclude additional absorbing water prior to performing the TGA from the TGA results, the initial weight is taken at 145 °C [7]. In addition, using the mass loss resulted from this technique, a

calculated stoichiometric formula for each varying C/S mixture ratios from 0.6 to 2.0 C/S C-S-H are presented in Table 4.7. Using the mass loss resulted from this technique, the stoichiometric formulas of synthetic C-S-H dried to 11% RH in this study for 0.7, 1.5, and 2.0 are approximated as $C_{0.53}SH_{0.41}$, $C_{1.29}SH_{1.49}$,and $C_{1.69}SH_{2.06}$,respectively. Detailed explanation for the calculation of this analysis was explained in the experimental methodology section. TGA analysis shows a comparison between the synthetic C-S-H produced with 0.7, 1.5, and 2.0 C/S mixture ratios resulted in C-S-H with 0.53, 1.29, and 1.69 C/S ratios. It is noted that the C/S mixture ratios may not exactly be equal to the ratio calculated, there is a trend from 0.6 to 2.0 where it increase in the calcium oxide and water values.

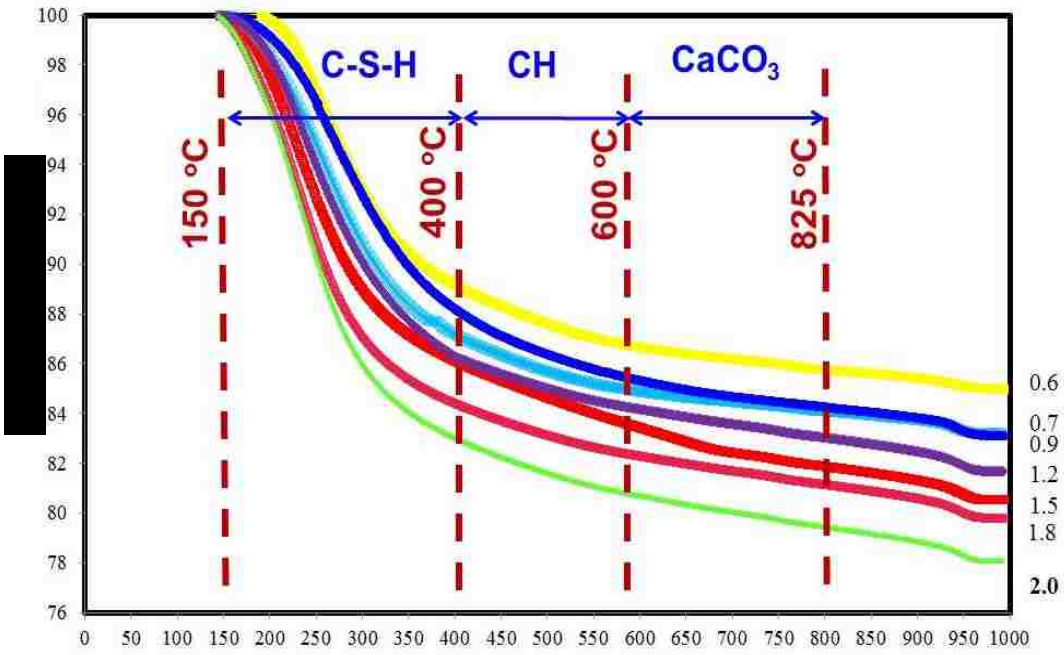

Figure 4.17 TGA Analysis of 0.6 to 2.0 C/S Mixture Ratio

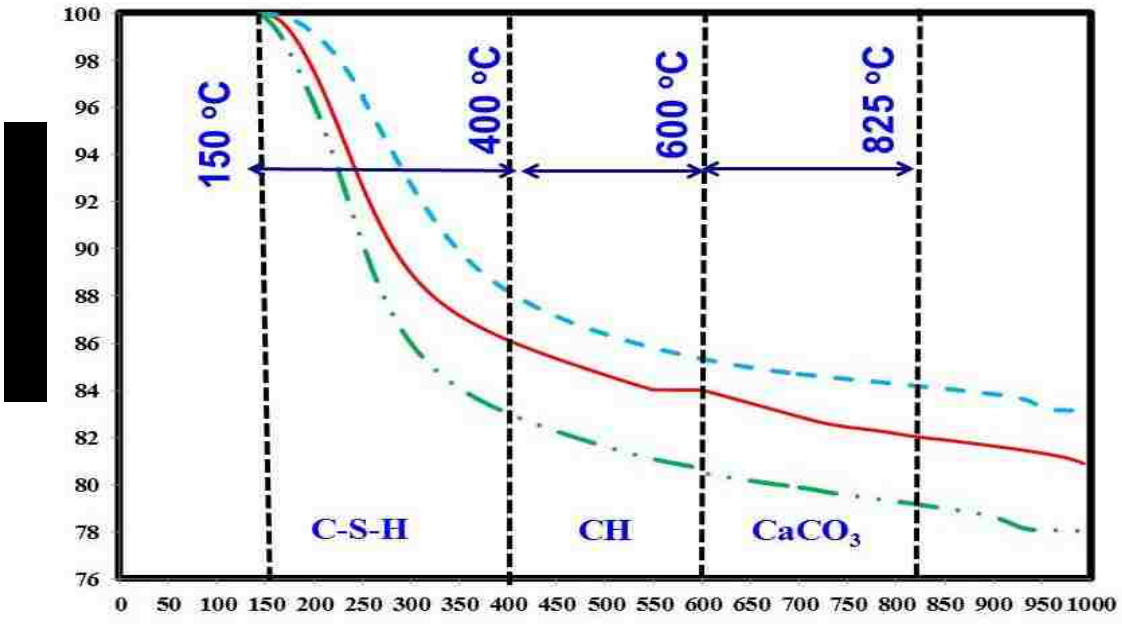

Figure 4.18 : TGA Analysis of 0.7, 1.5, and 2.0 C/S Mixture Ratio

Table 4.7: TGA phase

C/S mixture	150 °C ~ 400 °C	400 °C ~ 600 °C	600 °C ~ 825 °C	Stoichiometric formula
0.6	7.03%	1.15%	0.87%	$C_{0.53}$ $SH_{0.41}$
0.7	10.82%	2.11%	0.98%	$C_{0.60}$ $SH_{0.72}$
0.9	12.81%	2.12%	1.01%	$C_{0.73}$ $SH_{0.95}$
1.2	13.68%	2.30%	1.27%	$C_{1.02}$ $SH_{1.24}$
1.5	13.83%	2.33%	1.27%	$C_{1.29}$ $SH_{1.49}$
1.8	15.41%	2.47%	1.39%	$C_{1.41}$ $SH_{1.68}$
2.0	16.78%	2.69%	1.67%	$C_{1.69}$ $SH_{2.06}$

4.8 X-ray Diffraction (XRD)

The main crystalline phases detected from this analysis is Portlandite·$Ca(OH)_2$, jennite, and tobermorite $9A \cdot Ca_5S_{16}O(_{16}(OH)_2$. These formations indicate similar evidence found in literature in regards to the phases of 0.6 to 1.5 to be a 1.4-nm tobermorite type layer while the 2.0 C/S C-S-H to be a jennite structure formation. In literature, it states that the C/S mixture ratio is found to be within the range of 1.5 to 1.7 C/S mixture ratio similar to Portland cement paste. XRD peaks for all C/S mixture ratios are shown from Figure 4.6 to 4.9 for 0.7, 1.5, and 2.0. For C/S mixture ratio of 0.6, 0.9, 1.2, and 1.8 are presented in the Appendix C where it aids in the verification of C-S-H and CH presented in the analysis. In comparing the three spectra, 0.7 has limited C-S-H crystalline structure, indicating a tobermorite classification while the 2.0 spectra are similar to a jennite structure. In analyzing the 1.5 C/S Mixture Ratio where it confirms that both 0.7 and 2.0 have a high content of CH formation as opposed to the 1.5 C/S C-S-H mixture ratio. In addition there is a high CH content in both 0.7 and 2.0, There is little difference between the two spectra with a tendency to enable CH formation at a high C/S mixture ratio of 1.5. It is noted that CH is more crystalline than C-S-H and the peaks appear disproportionally high for their actual volume in the sample. The XRD spectra confirms that most of the higher stiffness phases observed in C-S-H made using 0.7 and 2.0 C/S mixture ratio compared with C-S-H produced using 1.5 C/S mixture ratio cannot be attributed to high CH content but rather to either HD C-S-H or to the lower water content in the final C-S-H material as apparent from TGA analysis. Peaks present at 7º, 29º, 32º, and 55º are typical characteristic of C-S-H where the XRD peaks are attributable to C-S-

H lined up concur to published results [7, 35 and 21]. Figure 4.19 through 4.22 shows the 0.7, 1.5, 2.0, a comparisons graph between the 0.7, 1.5, and 2.0 ratios.

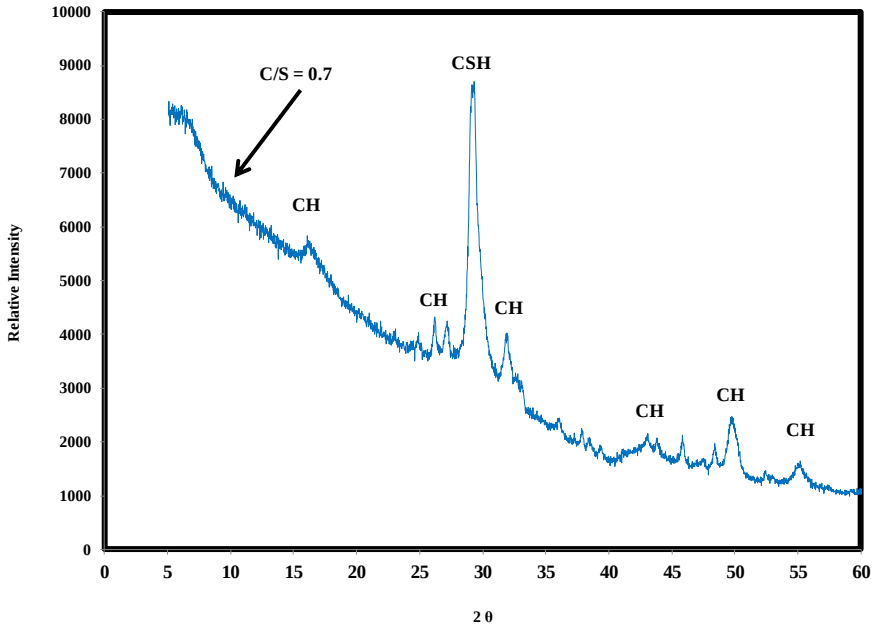

Figure 4.19 XRD : Relative Intensity 0.7 C/S C-S-H

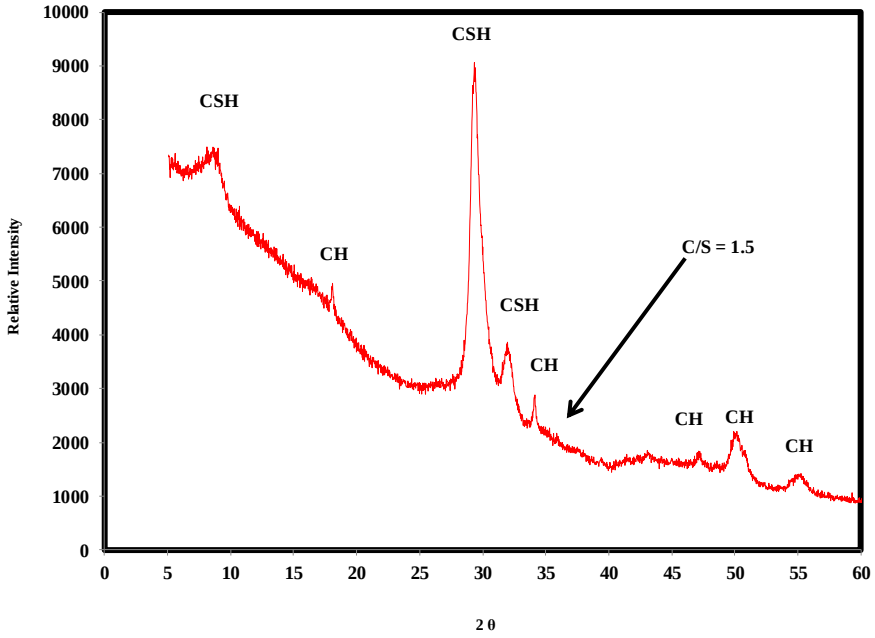

Figure 4.20 XRD : Relative Intensity 1.5 C/S C-S-H

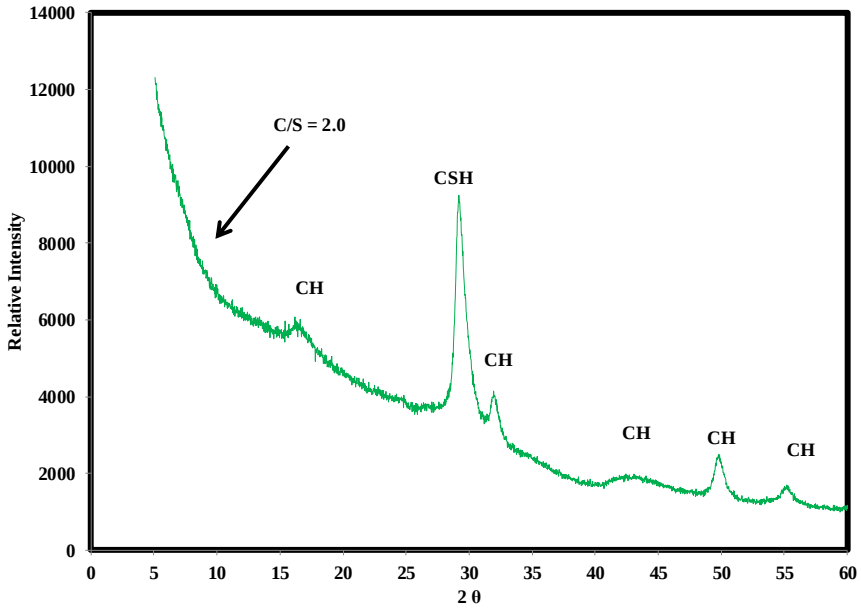

Figure 4.21 XRD : Relative Intensity 2.0 C/S C-S-H

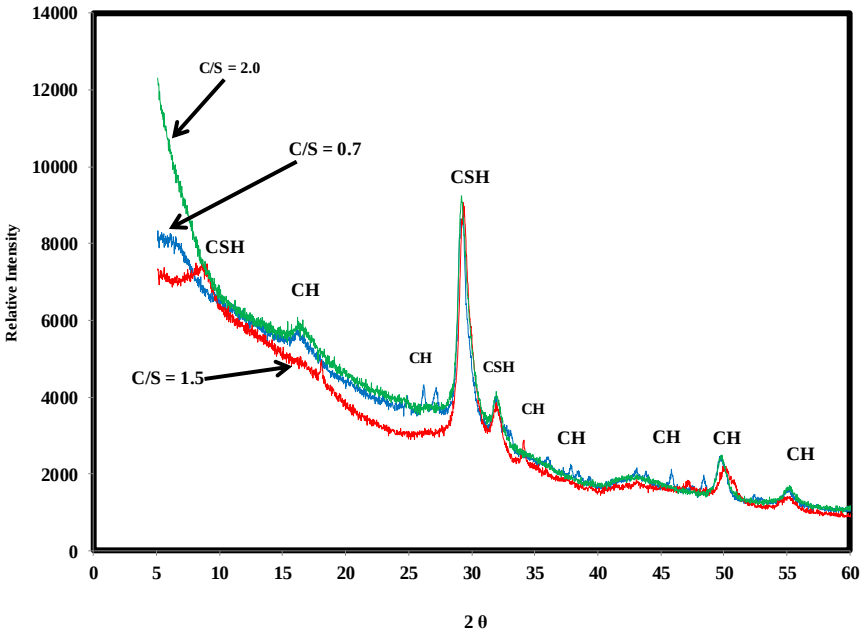

Figure 4.22 XRD : Relative Intensity 0.7, 1.5, and 2.0 C/S C-S-H

4.9 ^{29} Si Magic Angle Spinning Nuclear Magnetic Resonance (NMR)

^{29}Si MAS-NMR is a used for analyzing the silicate connectivity and polymerization of silica-based compounds. Figure 4.23 through Figure 4.26 shows ^{29}Si MAS-NMR spectra of C-S-H for 0.7 , 1.5, and 2.0 C/S mixture. The silicate connectivity Q^n of Q^1, Q^2_b, Q^2 and Q^3 were observed near the corresponding peaks of -79.35 ppm, -79.13 ppm, -85.5 ppm and -85.7 ppm respectively. The average degree of silicate connectivity *n* can be calculated using the calculated Q^n intensities as $n = (Q^1+2Q^2+3Q^3) / (Q^1+Q^2+Q^3)$ (Saoût 2006). C-S-H with a 1.5 C/S mixture ratio shows near-equal Q^1 and Q^2 bonding at -79.3 and -85.6 respectively, while for 0.7 C/S, mostly Q^2 is observed. The average degree of silicate connectivity *n* for 0.7 and 1.5 C/S mixture ratio are calculated as 1.975 and 1.454 respectively.

0.7 C/S Mixture Ratio

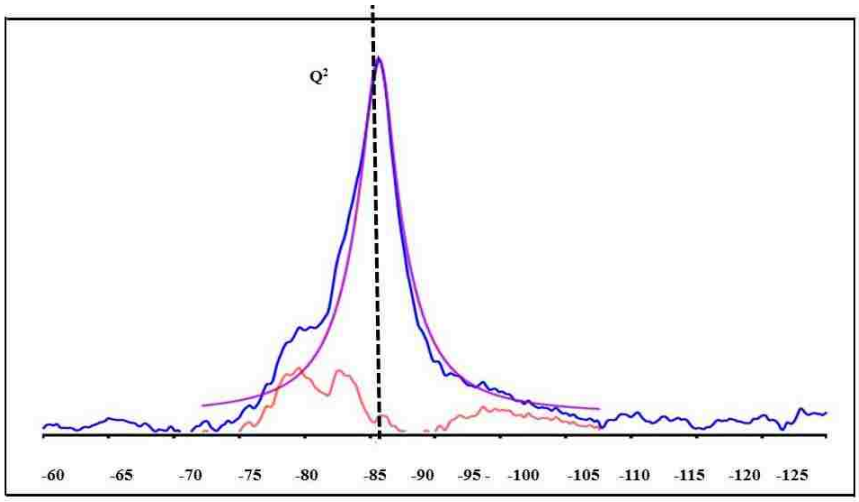

Figure 4.23: ^{29} Si MAS-NMR 0.7 C/S C-S-H Deconvolution

1.5 C/S Mixture Ratio

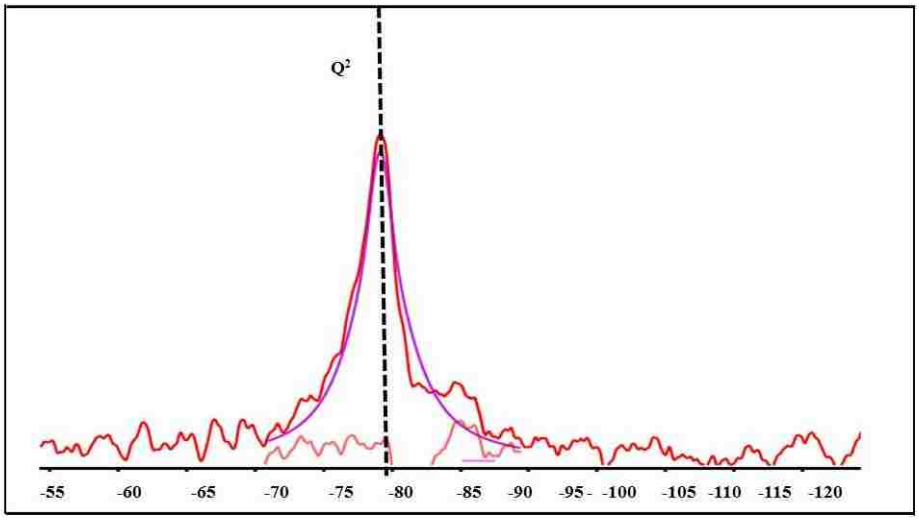

Figure 4.24: ^{29} Si MAS-NMR 1.5 C/S C-S-H Deconvolution

2.0 C/S Mixture Ratio

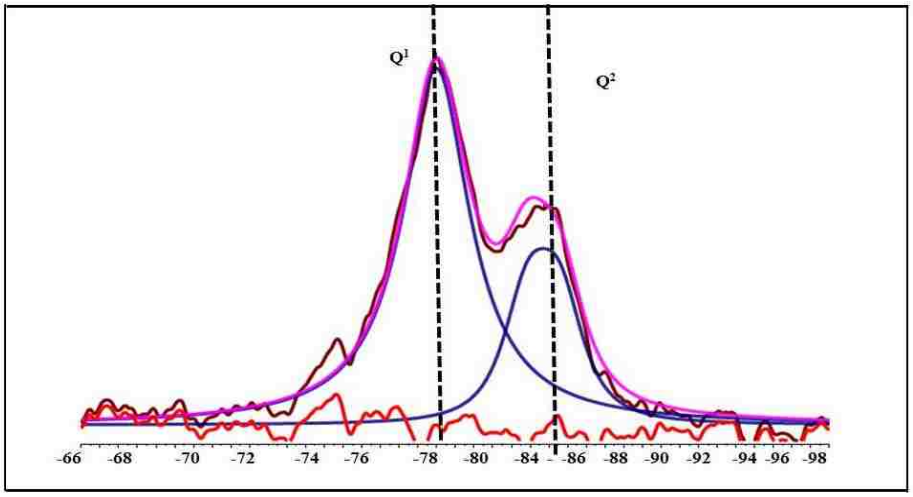

Figure 4.25: ^{29} Si MAS-NMR 2.0 C/S C-S-H Deconvolution

4.10 Transmission Electron Microscope (TEM)

TEM specimens were made by producing a droplet including C-S-H and observing it under the TEM. TEM images shown in Figure 4.28 through Figure 4.31 confirm NMR observation. While no particular feature can be observed in C-S-H produced using 1.5 mixture ratio, a very distinct rod-like structure is observed in C-S-H produced using 0.7 C/S mixture ratio. It is strongly believed that such rod-like connection represents silicate chain polymerization.

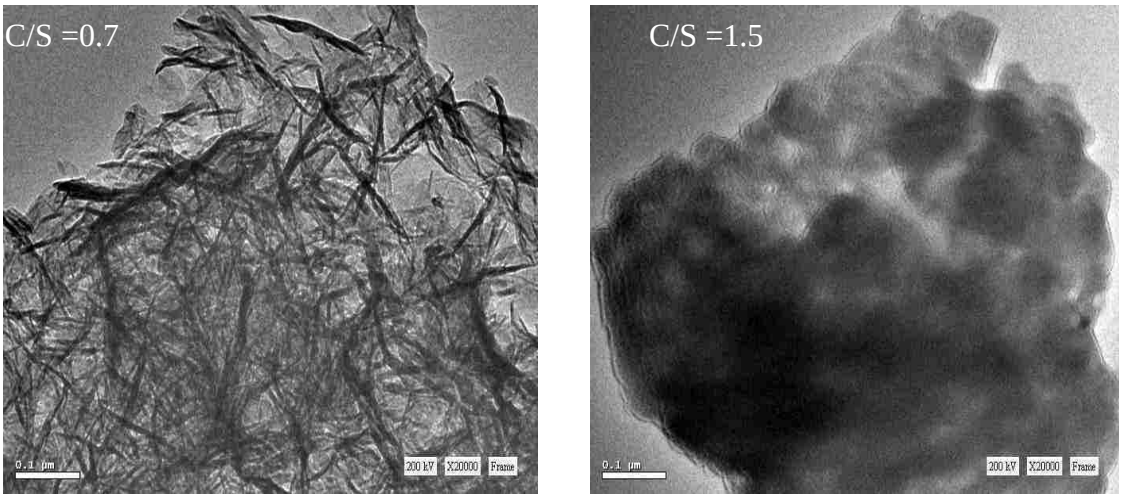

Figure 4.26: 0.7 & 1.5 C/S C-S-H image at resolution of 200 kV x 20000

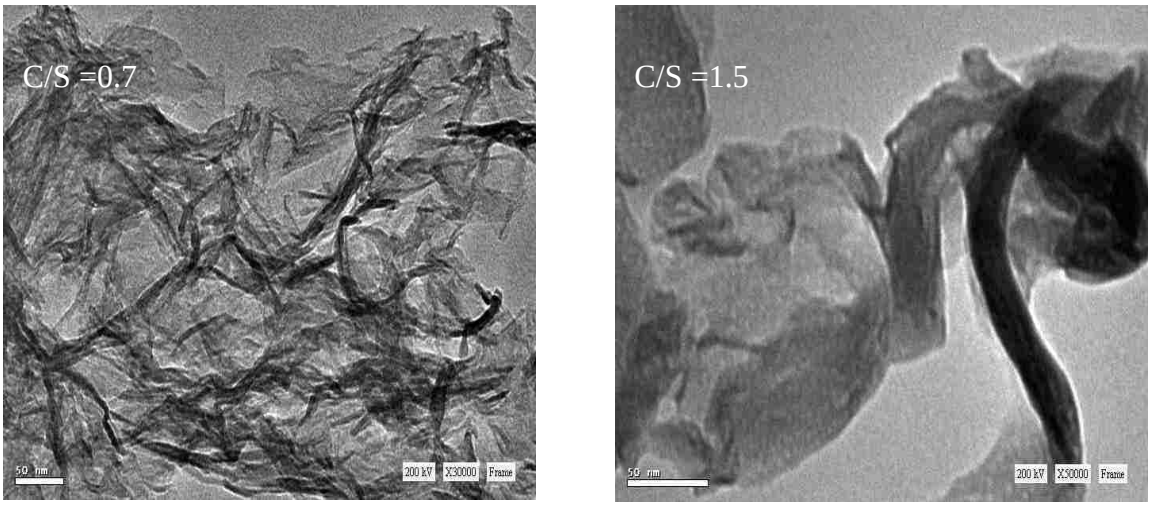

Figure 4.27: 0.7 & 1.5 C/S C-S-H image at resolution of 200 kV at X25000 and X50000

4.11 Scanning Electron Microscopy (SEM)

Scanning electron micrographs of C-S-H are shown in Figure 4.31. Specimens were not coated and careful prepared prior to being placed in the SEM. The investigations of 0.7 and 1.5 C/S C-S-H show a relatively homogenous C-S-H.

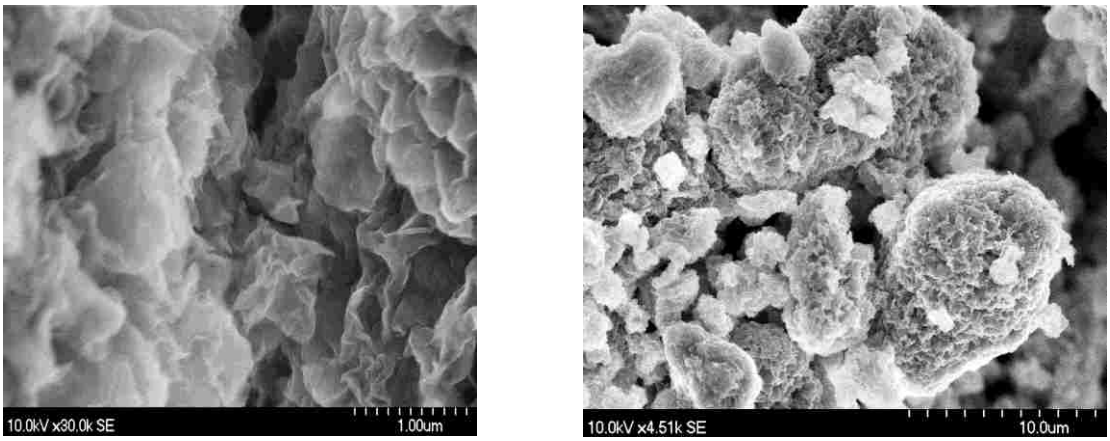

Figure 4.28: 0.7 and 1.5 C/S C-S-H images

Chapter 5 Conclusion and Recommendations

In this study, synthetic calcium silicate hydrate (C-S-H) was produced with the calcium to silicate (C/S) mixture ratios varying from 0.6 through 2.0. The produced C-S-H was dried at 11% relative humidity (RH) condition. In order to investigate the mechanical behavior of C-S-H, compacted C-S-H specimens were produced. This was achieved by compacting C-S-H powder at various compaction levels ranging from 200 to 500 MPa. Solid C-S-H specimens at three C/S ratios of 0.7, 1.5, and 2.0 were used to characterize the bulk density, elastic modulus, and creep compliance of C-S-H. In addition, the specific gravity of the powder C-S-H at all mixture ratios was measured. Furthermore, C-S-H powder was characterized using Thermo gravimetric analysis (TGA), X-Ray Diffraction (XRD), Brunauer-Emmitt-Teller (BET), 29Si Magic Spinning Nuclear Magnetic Resonance (NMR), Transmission Electron Microscope (TEM) and Scanning Electron Microscope (SEM). Successful compaction was performed at the maximum pressure of 500 MPa where the modulus of elasticity for the 0.7, 1.5, and 2.0 C/S C-S-H was found to be 216.8, 497.1, and 627.4 GPa respectively. Moreover, mechanical characterization of compacted C-S-H using nanoindentation and dynamic modulus analyzer (DMA) was conducted. Nanoindentation showed the 0.7 C/S ratio of C-S-H to have high reduced elastic modulus and low creep compliance in comparison with C-S-H produced with the 1.5 C/S mixture ratio. Statistical deconvolution analysis of the nanoindentation data showed that the 0.7 C/S ratios have stiffer submicron phases than the C-S-H produced using the 1.5 C/S mixture ratio. DMA results disclosed the elastic effect where 0.7 and 1.5 C/S C-S-H have similar storage modulus as opposed to the 2.0 C/S mixture ratio. This observation signifies that significantly reducing silica content to

achieve a 2.0 C/S ratio produces C-S-H with relatively high stiffness. On the other hand, creep of the compacted C-S-H was evaluated by observing (tan δ) where δ is the damping angle. It was shown that C-S-H with 0.7 C/S ratios has a lower creep than the 1.5 C/S mixing ratio. However, adding more silica content significantly to the mixing ratio leads to changing the trend where creep gets significantly lower on the macro scale when reaching 2.0 C/S mixing ratio. The bulk density for the different C/S mixing ratios was calculated and the 0.7 C/S mixing ratio was found to have a lower density than the 1.5 and 2.0 C/S mixing ratio. In addition, the 0.7 C/S mixing ratio was found to have a lower specific gravity than the 1.5 and 2.0 C/S mixing ratio. BET showed a high surface area of the 0.7 C/S ratio compared with the 1.5 and 2.0 C/S mixing ratios which indicate a higher void content.

The above observations can be explained by having two counteracting factors combining the nano and macro scale characteristics of C-S-H. At relatively low C/S ratios (e.g. C/S = 0.7), the ability of silica to form polymerized chains stiffen C-S-H as this effect overcomes the increased porosity of C-S-H at high silica content. The result of the above interaction is an increased stiffness and reduced creep of the 0.7 C/S ratio. The role of silicate polymerization is confirmed by nanoindentation proving a significant volume fraction of high stiff submicron phases and by TEM images showing significant silicate polymerization. On the other hand, it seems there is a maximum limit of C/S ratio beyond which the reduced porosity due to reduced silica content will overcome the absence of silicate polymerization and thus, in turn, will also result in increasing the stiffness and reducing creep of C-S-H at relatively high C/S ratios such as 2.0.

TGA analysis confirmed that C-S-H with a 0.7 C/S ratio to have a considerably lower water content than 1.5 C-S-H. In addition, as one can observe, a trend showing increased water content occurred with increasing the C/S mixture ratio. The reduction in nano-creep compliance of the 0.7 C-S-H might therefore be attributed to such reduction in water content in addition to silicate polymerization. It is evident the C/S mixture ratios of different synthetic C-S-H have an impact on water content and thus on the mechanical behavior of C-S-H where water plays an important role. Furthermore, XRD analysis showed lower CH content in the 0.7 C-S-H compared with the 1.5 and 2.0 C-S-H. Moreover, the XRD and NMR confirmed the formation of a typical C-S-H reported by previous research. NMR observations confirmed that 0.7 C-S-H has a much higher silicate polymerization and a different microstructure. Not to mention, the silicate polymerization in C-S-H was observed as the C/S ratio was decreased. TEM images showed that the 0.7 C/S mixing ratio results in a rigid rod like structure of C-S-H opposed to the classical amorphous and globule like C-S-H formed with the 1.5 C/S mixing ratio.

Future Research

One of the recommendations is to conduct fracture testing of C-S-H at varying C/S ratios. We believe that reducing the C/S ratio would tend to result in a stiffer C-S-H. Further research is warranted to identify the optimal C/S ratio for improved fracture toughness of C-S-H. One other important investigation is to examine the effect of changing the alkali (here being lime) on the hydration and behavior of the silicate-hydrate. New research at UNM examined the significance of magnesium and/or iron silicate hydrate on formation energy and mechanical characteristics compared with C-S-H.

Reference

[1] Neville, J.J., Brooks, A.M., *Concrete Technology - Volume 1*. Singapore: Longman Singapore Publishers Ltd., 1987.

[2] Taylor, H.F.W., *Cement Chemistry*, 2nd Edition. Thomas Telford Publishing, 1997.

[3] Constantinides G, Ulm F-J, "The nanogranular nature of C-S-H" *J. Mech. Phys. Solids*, vol. 55, pp. 64–90, 2007.

[4] Guillot, C.,"A Hell made of Oil," *Eng. Technol.*, vol. 14, no. September, 2010.

[5] Venables, M.,"Deepwater Drilling in deep trouble," *Eng. Technol.*, vol. 14, no. July, pp. 14–16, 2010.

[6] Taylor, H.F.W., "726 Hydrated Calcium Silicate. Part I. Compound Formation at Ordinary Temperature," *Journal of the Chemical Society.*, pp. 3682–3690, 1950.

[7] Foley, E.M., Kim, J.J., Reda Taha, M.M., "Synthesis and Nano-Mechanical Characterization of C-S-H with a 1.5 C/S Ratio," *Cement and Concrete Research.*, vol. 42, pp. 1225-1232, 2012.

[8] Alonso, C., Fernanadez, L., "Dehydration and rehydration processes of cement paste exposed to high temperature environments," *Journal of Material Science*, vol. 39, pp. 3015-3024, 2004.

[9] Alizadeh, R., Beaudoin, J.J., Raki, L., "Mechanical properties of calcium silicate hydrates," *Material and Structures*, vol. 44, no. 1, pp. 13–28, Apr. 2010.

[10] Taylor, H.F.W.," Proposed Structure for Calcium Silicate Hydrate Gel," *J. Am. Ceram. Soc.*,vol. 69, no. 6, pp. 464–467, 1986.

[11] Tennis, P.D., Jennings, H.M., " A model for two types of C-S-H in the microstructure of cement paste," *Cement and Concrete Research*, vol. 30, pp. 101–116, 2000.

[12] Jennings, H.M., "A model for the microstructure of calcium silicate in cement paste," *Cement and Concrete Research*, vol. 30, pp. 855-863, 2000.

[13] Taplin, J., "A method for following the hydration reaction in Portland cement paste," *Aust. J. Appl. Sci.*, vol. 10, pp. 329-345, 1959

[14] Richardson, I.G., "Tobermorite/jennite- and tobermorite/calcium hydroxide-based models for the structure of C-S-H: applicability to hardened pastes of tri-calcium silicate, β-dicalcium silicate, Portland cement, and blends of Portland cement with blast-furnace slag, metakaol," *Cement and Concrete Research.*, vol. 34, no. 9, pp. 1733–1777, Sep. 2004.

[15] Nonat, A., "The structure and stoichiometry of C-S-H," *Cement and Concrete Research*, vol. 34, no. 9, pp. 1521–1528, Sep. 2004.

[16] Sugiyama,D., "Chemical alteration of calcium silicate hydrate (C-S-H) in sodium chloride solution," *Cement and Concrete Research,* vol. 38, pp. 1270–1275, 2008.

[17] Lea, F.M., "*The Chemistry of Cement and Concrete*," 3rd Edition. New York, N.Y.: Chemical Publishing Co. Inc., 1971, pp. 177–202

[18] Alizadeh, R., Beaudoin, J.J., Raki, L., "Mechanical properties of calcium silicate hydrates," *Material and Structures*, vol. 44, no. 1, pp. 13–28, Apr. 2010.

[19] Cong, X., and Kirkpatrick, R.J., "^{29} Si MAS NMR Study of the Structure of Calcium Silicate Hydrate," *Adv. Cem. Mat*., vol. 3, pp. 144-156, 1996

[20] Cong, X., and Kirkpatrick, R.J., "^{17} O MAS NMR Study of the Structure of Calcium Silicate Hydrate gel," *Adv. Cem. Mat*., vol. 79, pp. 1585-1592, 1996

[21] Cong, X., and Kirkpatrick, R.J., "^{29} Si and ^{17} O MAS NMR Investigation of the Structure of Some Crystalline Calcium Silicate Hydrates," *Adv. Cem. Mat*., vol. 3, pp. 133-143, 1996

[22] FitzGerald, S.A, Newmann, D.A., and Rush, J.J., "In situ quasi-elastic neutron scattering study of the hydration of Tri-calcium Silicate" *Chem. Mater.*, vol. 10, pp. 397–402, 1997.

[23] Young, J.F., Hansen, W., "Volume relationships for C-S-H formation based on hydration stoichiometries," *Mater. Res. Symp.*, vol. 85, pp. 313–322, 1987.

[24] Allen, A.J., Thomas, J.J., and Jennings, H.M. "Composition and density of nanoscale calcium-silicate-hydrate in cement.," *Nat. Mater.*, vol. 6, no. 4, pp. 311–6, Apr. 2007.

[25] Renaudin, G., Russias, J., Leroux, F., Frizon,F., and Cau-dit-Coumes, C.,"Structural characterization of C–S–H and C–A–S–H samples—Part I: Long-range order investigated by Rietveld analyses," *J. Solid State Chem.*, vol. 182, no. 12, pp. 3312–3319, Dec. 2009.

[26] Powers, T.C. and Brownyard, T.L., "Studies of the physical properties of hardened Portland cement paste," *ACI Journal Proc*., Vol. 43, p. 101-933, 1947

[27] Feldman, R., "A model for hydrated Portland cement paste as deduced from sorption-length change and mechanical properties," *Materiaux et construction*, vol. 1. pp.509-590, November, 1968

[28] Alizadeh, R., Beaudoin,J.J., Raki, L., and Terskikh,V., "C–S–H/polyaniline nanocomposites prepared by in situ polymerization," *J. Mater. Sci.*, vol. 46, no. 2, pp. 460–467, Sep. 2010.

[29] Beaudoin, J.J., and Feldman, R.F., "Dependence of degree of silica polymerization and intrinsic mechanical properties of C-S-H on C/S ratio," *8th International Congress on the Chemistry of Cement*, Brazil, V. 3, 337-342, 1986

[30] Atkins, M., Glasser, F., Kindess, A., "Cement hydrate phases: solubility at 25 degree C," *Cement and Concrete Research*, vol. 22, pp.1-6, 1992

[31] Lodeiro, I.G., D. E. Macphee, a. Palomo, and a. Fernández-Jiménez, "Effect of alkalis on fresh C–S–H gels. FTIR analysis," *Cement and Concrete Research*, vol. 39, no. 3, pp. 147–153, Mar. 2009.

[32] Odelson, J.B., Kerr, E.A, Vadaka,V. "Young's modulus of cement paste at elevated temperatures," *Cement and Concrete Research*, vol. 37, pp. 1225–263, 2007.

[33] Alarcon-Ruiz, L., Platret, G., Massieu, E., and Ehrlacher, A., "The use of thermal analysis in assessing the effect of temperature on a cement paste," *Cement and Concrete Research*, vol. 39, pp.3015-3024, 2004.

[34] Jain, J., Neithalath, N., "Physico-chemical change in nano-silica and silica fume modified cement paste in response to leaching, " *Int. J. Mater. Struct. Integ*r. vol. 3, pp.114-133, 2009

[35] Kim, J.J, Foley, E.M, and Reda Taha, M.M., "Nano-mechanical characterization of synthetic calcium–silicate–hydrate (C–S–H) with varying CaO/SiO2 mixture ratios," *Cement and Concrete Composites.*, vol. 36, pp. 65–70, Feb. 2013.

[36] Oder, I., "The BET-specific surface area of hydrated Portland cement and related materials," *Cement and Concrete Research,*. vol. 33, no. 12, pp.2049-2056, 2004.

[37] Jennings, H.M., Tennis, P.D. "Model for the developing microstructure in Portland Cement Paste," *J. Am. Ceram. Soc.*, vol. 77, pp. 3161-3172, 1994.

[38] Juenger, M.C.G., and Jennings, H.M., "Examining the relationship between the microstructure of Calcium Silicate Hydrate and Shrinkage of cement paste," *Cement and Concrete Research*, vol. 32, pp.289-296, 2002.

[39] Brunauer S., Emmett P. H., and Teller, E., "Absorption of gases in multimolecular layers, " *J. Amer. Chem. Soc.* vol. 62. pp.723. 1940.

[40] Collodetti, G., Gleize, P.J., and Monteiro, P., "Exploring the potential of siloxane surface modified nano-SiO2 to improve the Portland cement pastes hydration properties," *Constructions and Building Materials*, vol. 54, pp.91-105, 2014

[41] Magi,M., Lippmaa, E., and Samoson, A., " Solid-state high resolution silicon-29 chemical shifts in silicates," *Journal of Physical Chemistry*, vol. 88, pp.1518-1522, 1984

[42] Young, J.F., "Investigation of calcium silicate hydrate using silicon-29 nuclear magnetic resonance spectroscopy," *Journal of the American Ceramic Society*, vol. 31, no. 3, pp.C118-C120, 1988

[43] Yu, P., Kirkpatrick, R.J., " Thermal dehydration of tobermorite and jennite," *Cement and Concrete Research*, pp.185-191, 1999

[44] Alizadeh, R., "Nanostructure and Engineering Properties of Basic and Modified Calcium Silicate Hydrate System," Ph.D dissertation, University of Ottawa , 2009

[45] Li, S. and Roy, D.M., "Preparation of CaO/SiO2 ratio C-S-H*," J.Mater. Res*., vol 3, no. 2, pp. 379-386, 1988.

[46] Vandamme, M., Ulm, F-J, "Nanogranular orgin of concrete creep," Proceedings of the National Academy of Sciences, 106.26, pp.10552-10557, 2009

[47] Da Silva, W.R.L., Nemecek, J., Stemberk, P., " Application of multi-scale elastic homogenization based on nanoindentation for high performance concrete," *Advances in Engineering Software*, vol. 62-63, pp.109-118, 2013

[48] Constantinides, G. and Ulm, F-J., "The effect of two types of C-S-H on the elasticity of cement-based materials: Results from nanoindentation and micromechanical modeling," *Cement and Concrete Research*, vol. 34, no. 1, pp. 67–80, Jan. 2004.

[49] Mondal, L.D., Shah, P., Marks, S.P., "Nanoscale characterization of cementitious materials," *ACI Mater. J.*, pp. 174–179, 2008.

[50] ASTM Standard E 104-02: Standard Practice for maintaining Constant Relative Humidity by Means of Aqueous Solution. *ASTM International*, West Conshohocken, PA, 2007

[51] ASTM Standard C 914-95: Standard Test Method for Bulk Density and Volume of Solid Refractories by Wax Immersion. *ASTM International*, West Conshohocken, PA, 2007

[52] ASTM Standard C 188-09: Standard Test Method for Density of Hydraulic Cement. *ASTM Internationa*l, West Conshohocken, PA, 2007

[53] ASTM Standard D 87: Standard Test Method for Melting Point of Petroleum Wax (Cooling Curve). *ASTM International*, West Conshohocken, PA, 2007

[54] Oliver, W. C., and Pharr, G. M., "An improved technique for determining hardness and elastic modulus using load and displacement sensing indentation experiments" *Journal of materials research*, 7(6): 1564-1583, 1992

[55] Giannakopoulos, A., Elastic and viscoelastic indentation of flat surfaces by pyramid indenters. *J. of the Mechanics and Physics of Solids*, 2006. 54: p. 1305-1332.

[56] Lu H., Wang, B., Ma, J., Huang, G, and Viswanathan, H., "Measurement of creep compliance of solid polymers by nanoindentation", *Mech. of Time-dependent Materials*, pp. 189-207., 2003

[57] Saoût GL, Le´colier E, Rivereau A, Zanni H."Chemical structure of cement aged at normal and elevated temperatures and pressures, Part I: Class G oilwell cement" *Cement and Concrete Research*, 36, 71–78, 2006

[58] Boumiz, A., Etude compare des evolutions chimiques et mecaniques des pates de ciment et mortiers a tress jeune age, Ph.D thesis, University Denis Diderot, Paris 7, France 1995

[59] Granju, J.L., Modelisation des pates de ciments durcies: Caracterisation de l etat dehydration, loss of evolution de lat resistance en compression et du module de deformation longitudinale, PhD. Thesis, University Paul Sabatier de Toulouse, France 1987

[60] Pourbeik,P., Beaudoin, J.J., Alizadeh, R., and Raki, L., "Mechanical property-porosity relationships of layered calcium silicate hydrate phases," *Materials and Structures*, 46, pp. 1489-1495, 2013

Appendix A: Compaction Curve

0.7 C/S C-S-H Compaction Curves:

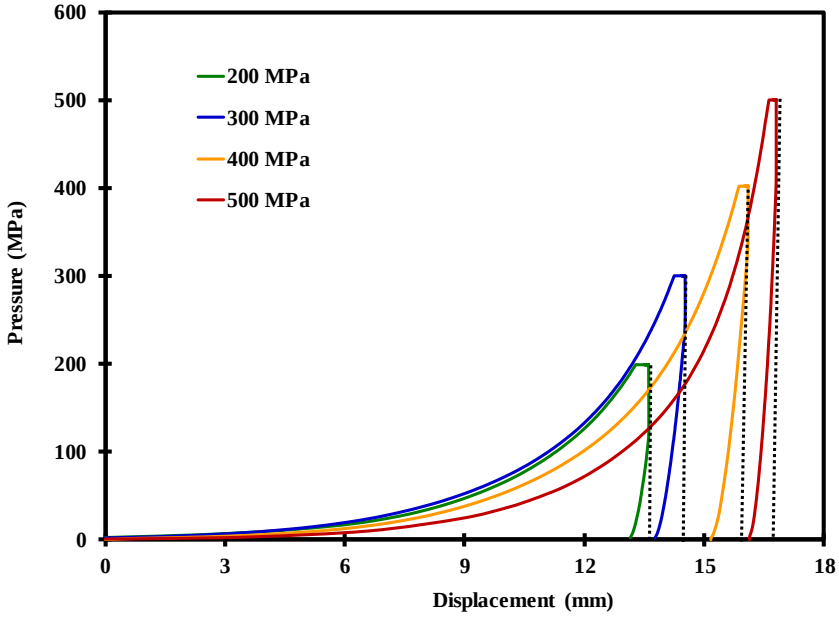

Figure A.1: BET Analysis of 0.7 C/S Mixture Ratio

2.0 C/S C-S-H Compaction Curves:

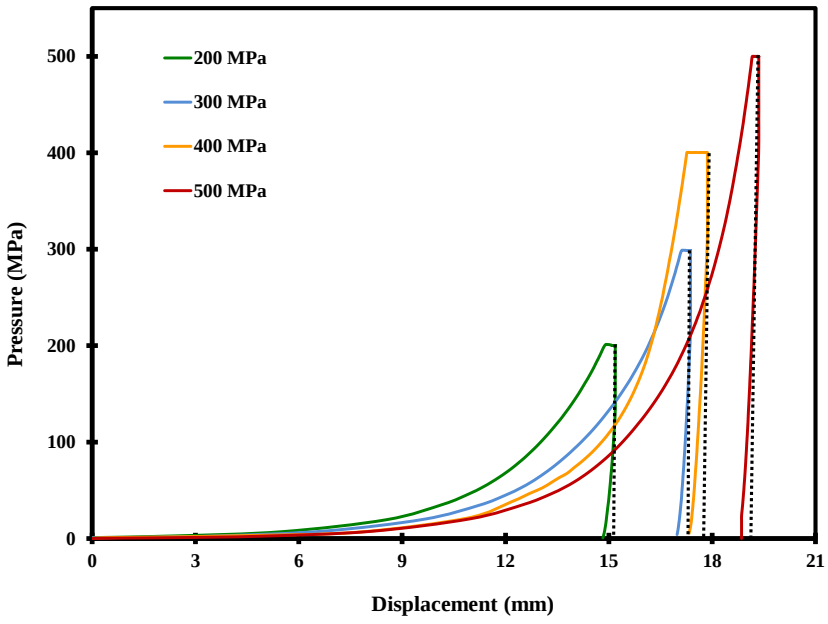

Figure A.2 BET Analysis of 2.0 C/S Mixture Ratio

Appendix B: BET Graphs

0.6 C/S C-S-H:

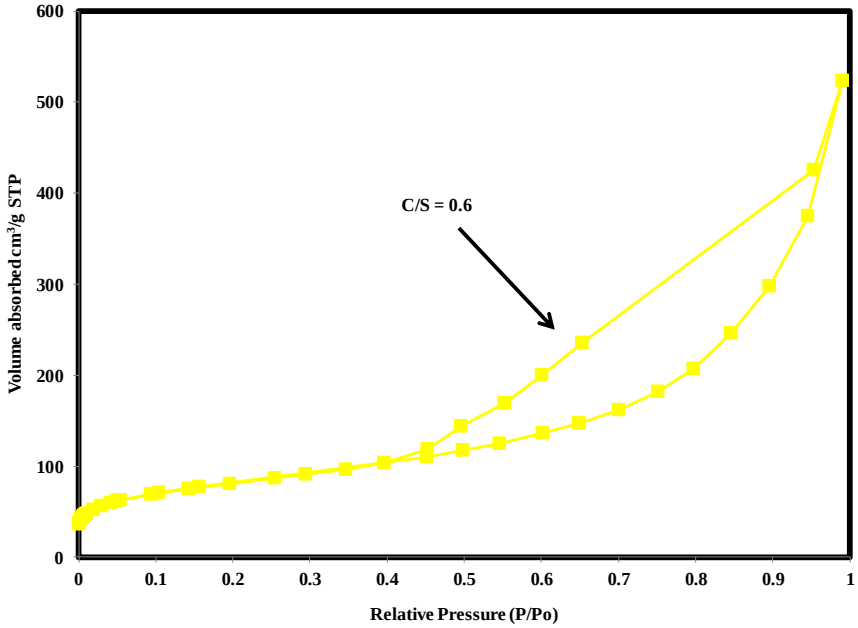

Figure B.1 BET Analysis of 0.6 C/S Mixture Ratio

0.9 C/S C-S-H:

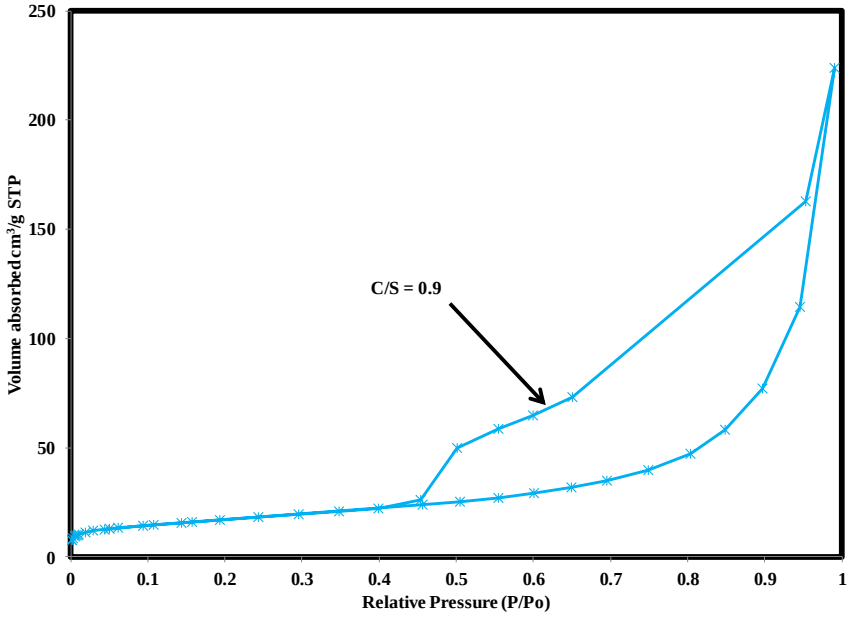

Figure B.2 BET Analysis of 0.9 C/S Mixture Ratio

1.2 C/S C-S-H:

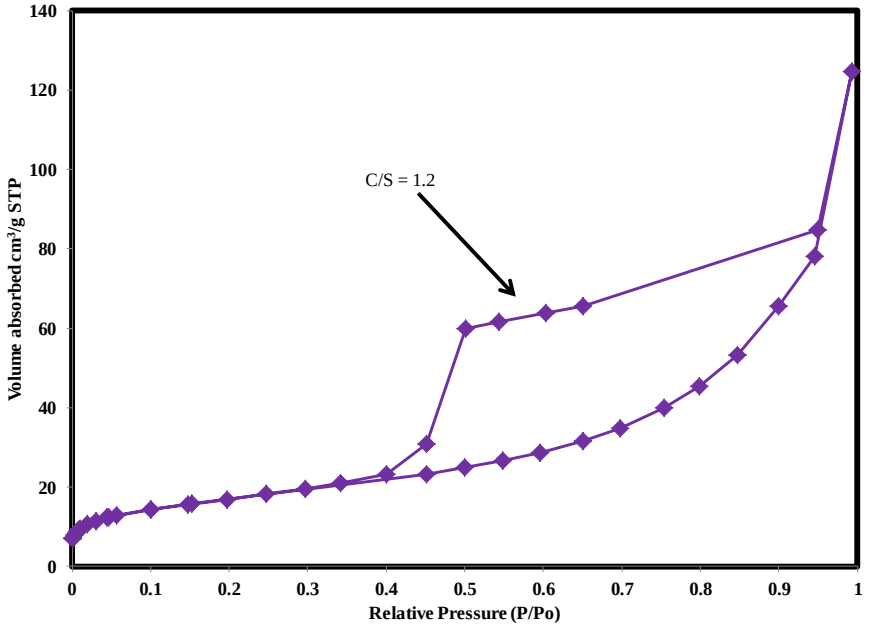

Figure B.3 BET Analysis of 1.2 C/S Mixture Ratio

1.8 C/S C-S-H:

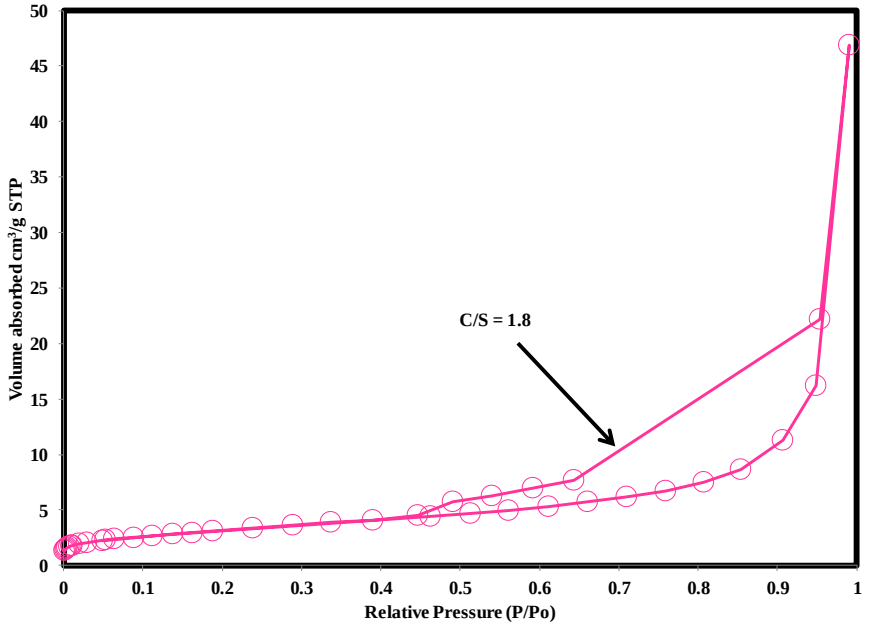

Figure B.4 BET Analysis of 1.8 C/S Mixture Ratio

Appendix C: XRD Graphs

0.6 C/S C-S-H:

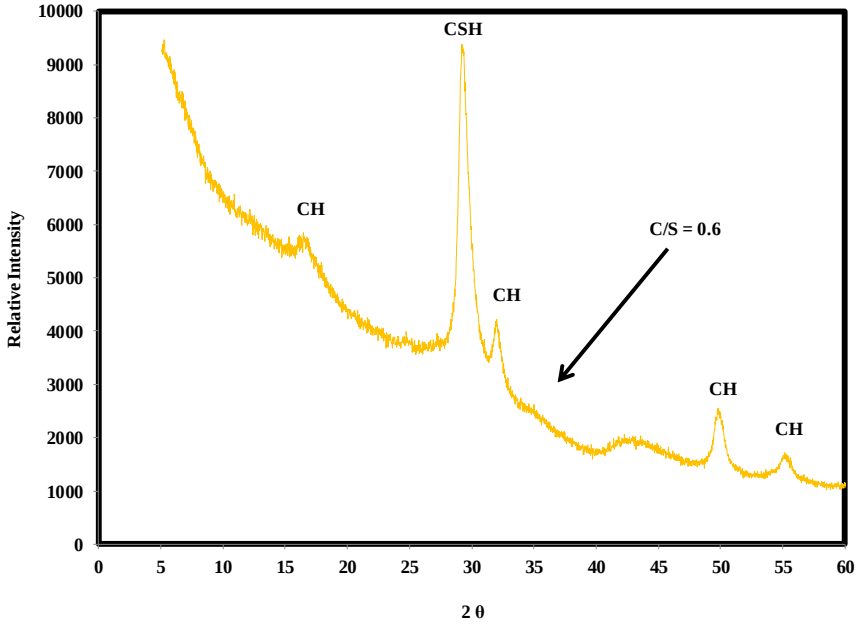

Figure C.1 XRD Analysis of 0.6 C/S Mixture Ratio

0.9 C/S C-S-H:

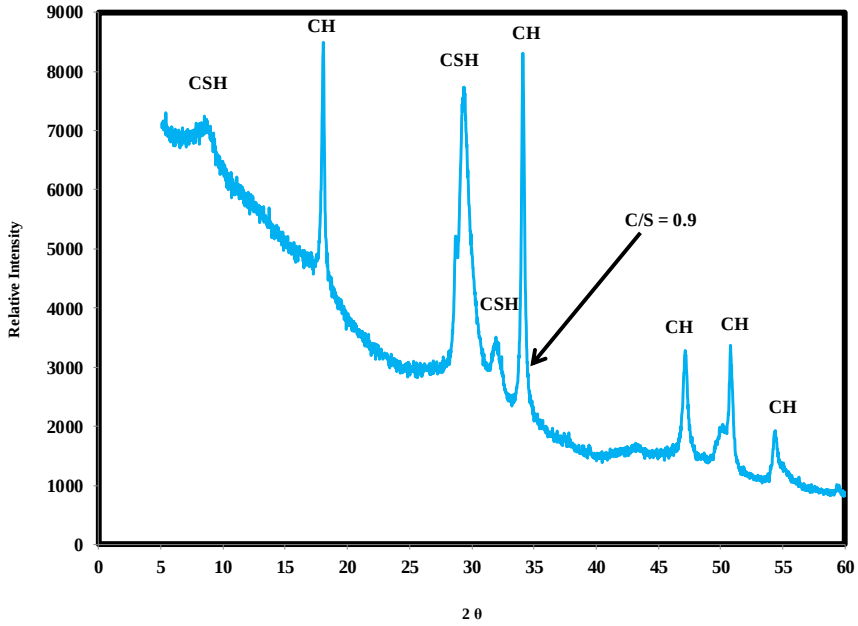

Figure C. 2 XRD Analysis of 0.9 C/S Mixture Ratio

1.2 C/S C-S-H:

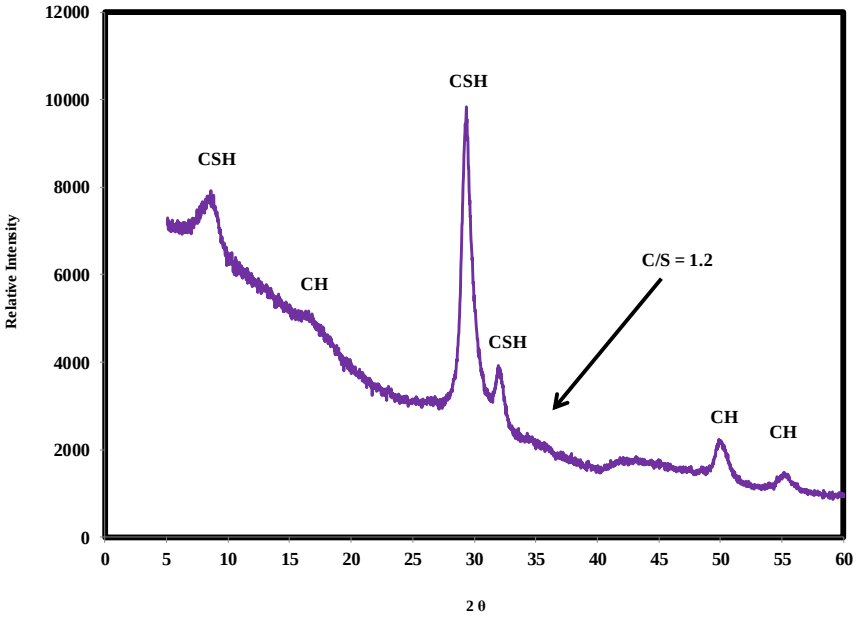

Figure C.3 XRD Analysis of 1.2 C/S Mixture Ratio

1.8 C/S C-S-H:

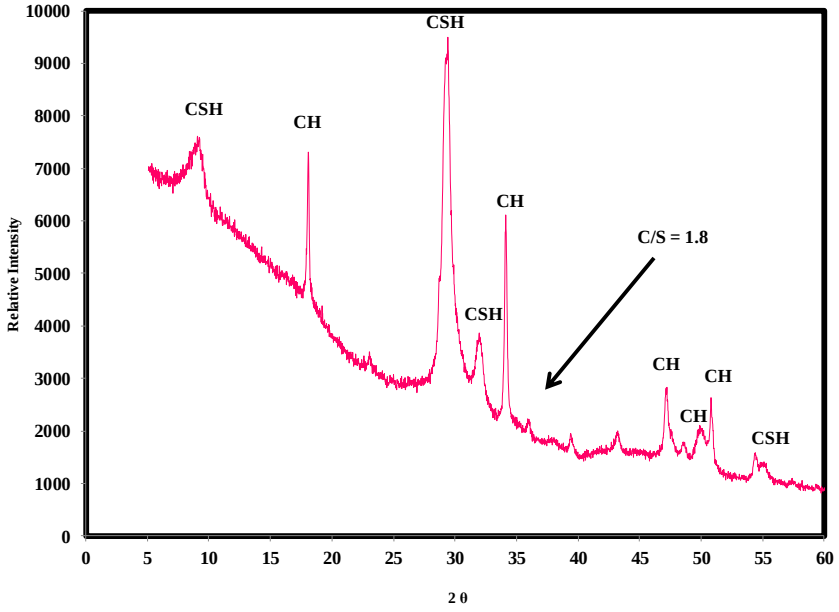

Figure C. 4 XRD Analysis of 1.8 C/S Mixture Ratio

Appendix D: NMR Graphs

0.6 C/S Mixture Ratio

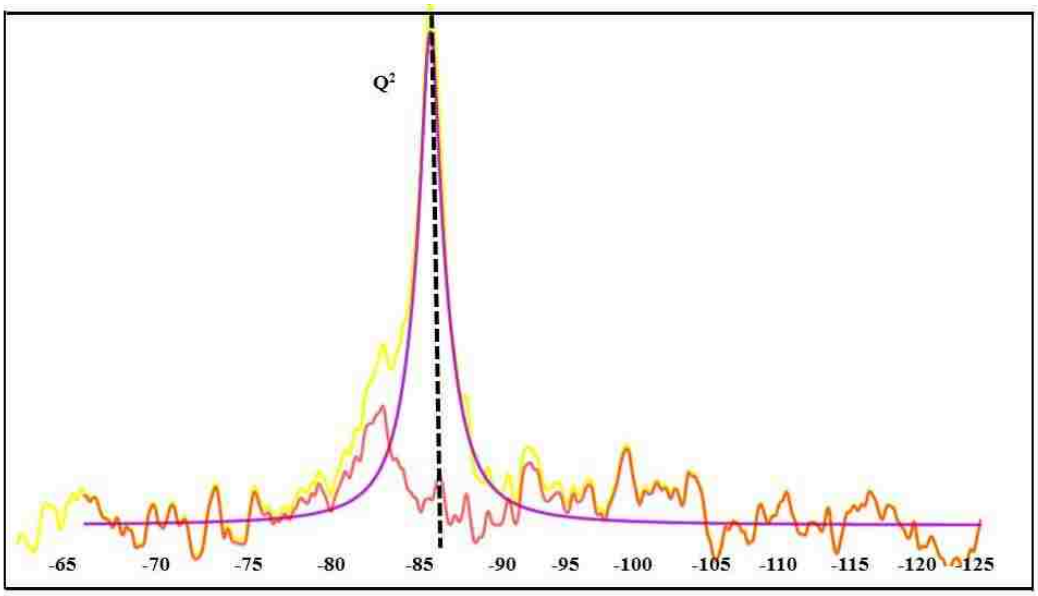

Figure D.1 NMR Deconvolution Analysis of 0.6 C/S Mixture Ratio

0.9 C/S Mixture Ratio

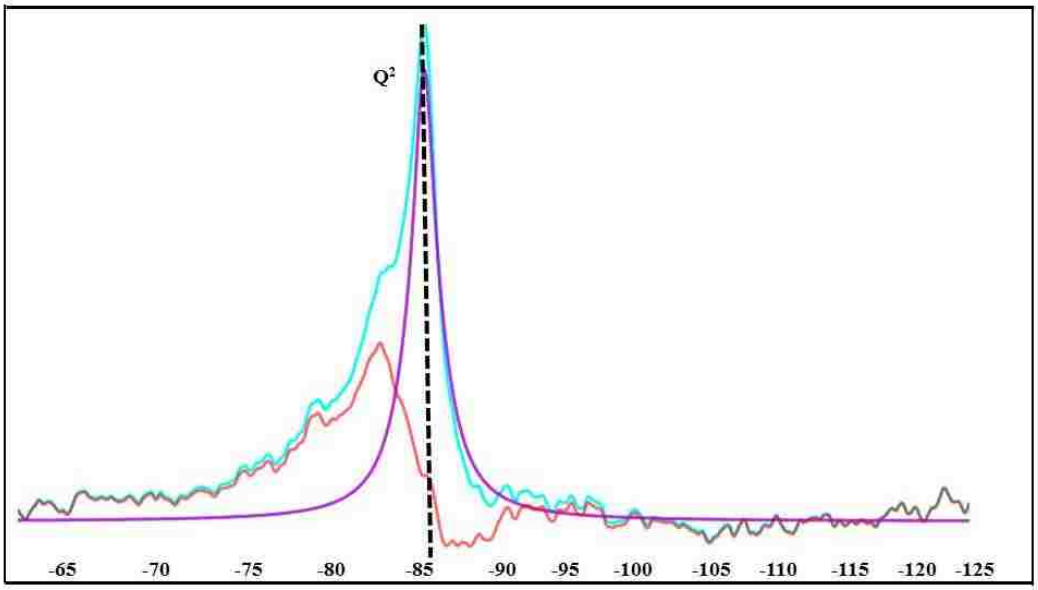

Figure D.2 NMR Deconvolution Analysis of 0.9 C/S Mixture Ratio

1.2 C/S Mixture Ratio

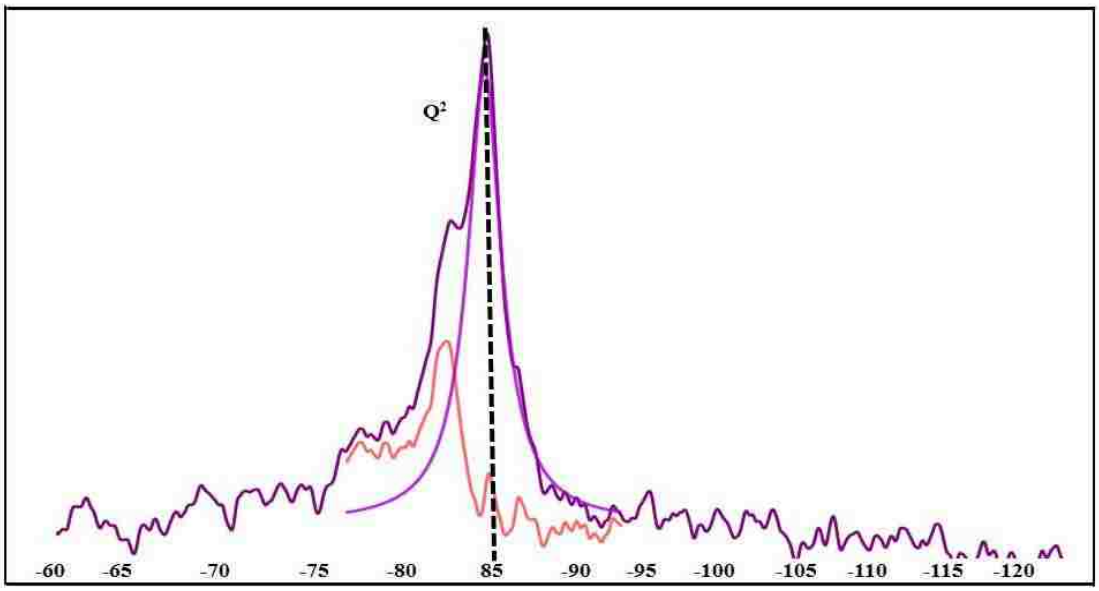

Figure D.3 NMR Deconvolution Analysis of 1.2 C/S Mixture Ratio

1.8 C/S Mixture Ratio

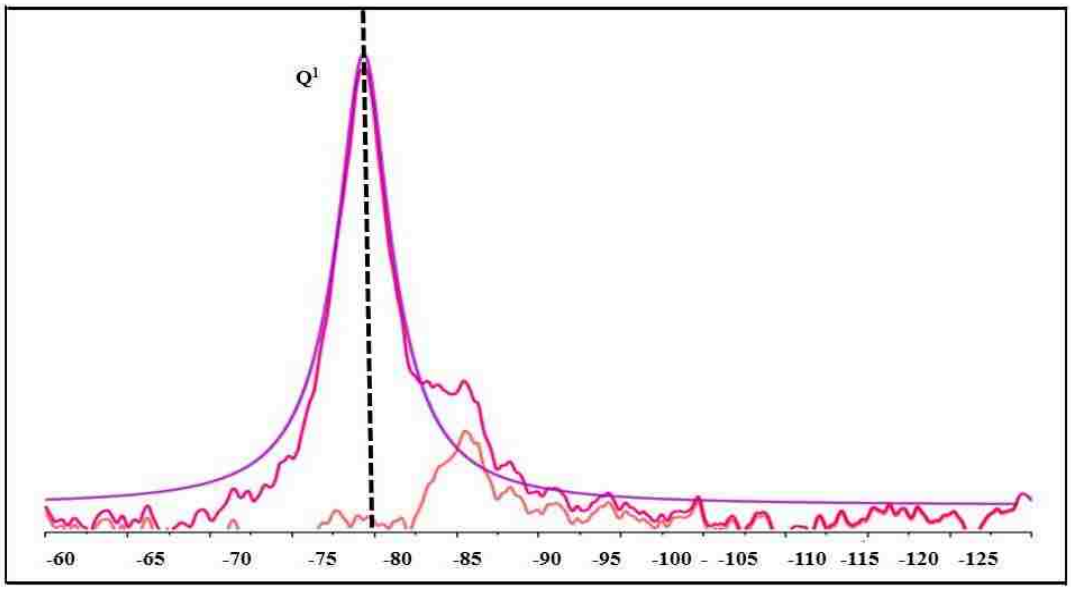

Figure D.4 NMR Deconvolution Analysis of 1.8 C/S Mixture Ratio

Appendix E: TEM Micrograph

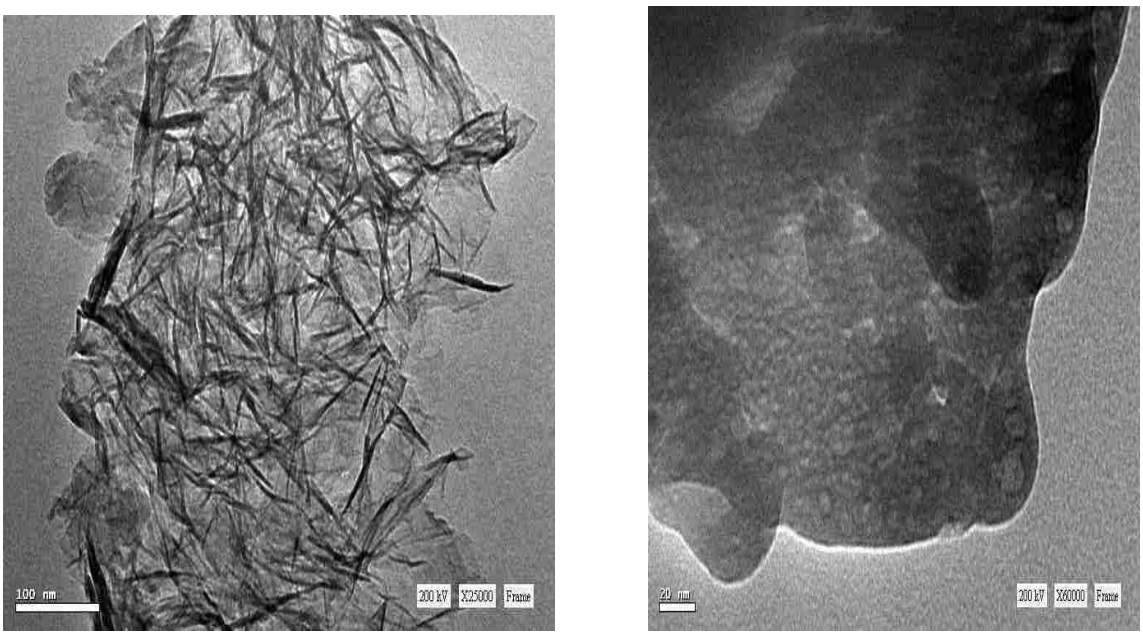

Figure E.1: 0.7 and 1.5 C/S C-S-H comparison images

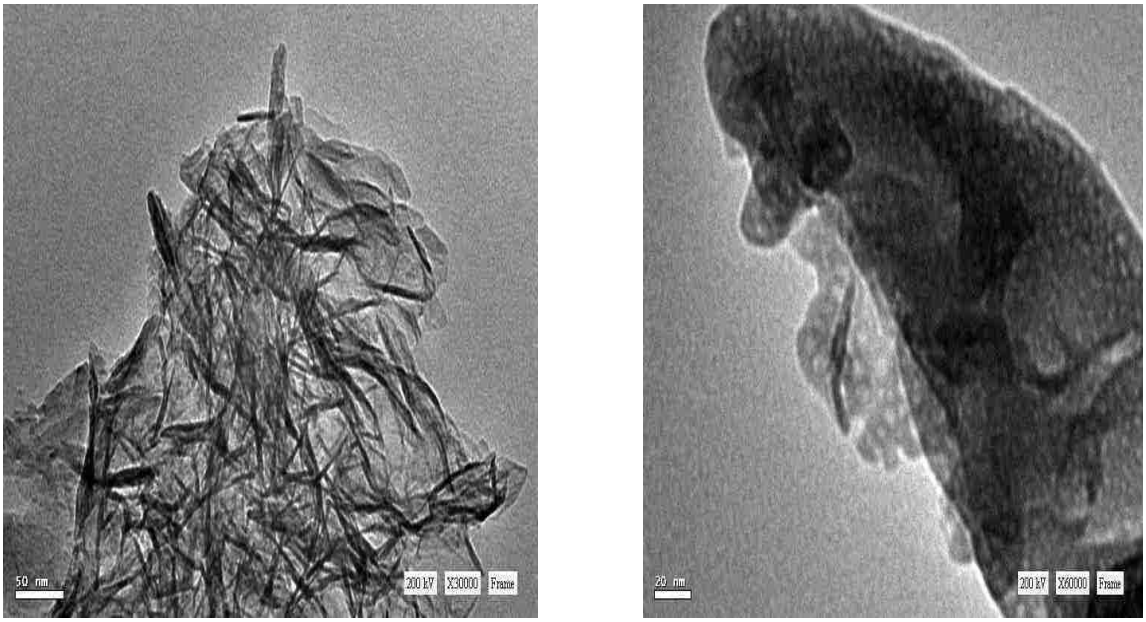

Figure E.2: 0.7 and 1.5 C/S C-S-H comparison images

Appendix F: Compaction Analysis

0.7 C/S C-S-H Calculation for 200 MPa:

Thickness measurement of the specimen :

t_r : initial thickness (mm)	t_f: final thickness (mm)
1.86	13.26

Raw Data for:

x : Displacement (mm)	y: Pressure (MPa)
17.732699	198.9321
17.733067	196.7498

Where, $\Delta y = 2.1823$
$\Delta x = 0.0003678$

Slope = $\frac{\Delta y}{\Delta x}$ = 5, 933.53

Using the equation 3.2:
$E_b = S_t (t_f - t_r)$ E_b = 5,933.53(13.26-1.86) = 67.6 GPa = 0.7 C/S at 200 MPa

0.7 C/S C-S-H Calculation for 300 MPa:

Thickness measurement of the specimen :

t_r : initial thickness (mm)	t_f: final thickness (mm)
1.78	13.26

Raw Data for:

x : Displacement (mm)	y: Pressure (MPa)
16.172425	299.8337
16.172765	297.5998

Where, $\Delta y = 2.2338427$
$\Delta x = 0.0003406$

Slope = $\frac{\Delta y}{\Delta x}$ = 6,558.28

Using the equation 3.2:
$E_b = S_t (t_f - t_r)$ E_b = 6,558.28 (13.26-1.78) = 75.3 GPa = 0.7 C/S at 300 MPa

0.7 C/S C-S-H Calculation for 400 MPa:

Thickness measurement of the specimen :

t_r : initial thickness (mm)	t_f: final thickness (mm)
1.82	13.26

Raw Data for:

x : Displacement (mm)	y: Pressure (MPa)
16.1019	401.7931
16.1010	395.0856

Where, $\Delta y = 6.7074492$
$\Delta x = 0.0008494$

Slope = $\frac{\Delta y}{\Delta x}$ = 7,896.91

Using the equation 3.2:
$E_b = S_t (t_f - t_r)$ E_b = 7,896.91 (13.26-1.82) = 90.3 GPa = 0.7 C/S at 400 MPa

0.7 C/S C-S-H Calculation for 500 MPa:

Thickness measurement of the specimen :

t_r : initial thickness (mm)	t_f: final thickness (mm)
1.69	13.26

Raw Data for:

x : Displacement (mm)	y: Pressure (MPa)
17.653068	500.1915
17.653427	493.4684

Where, $\Delta y = 6.7231465$
$\Delta x = 0.0003586$

Slope = $\frac{\Delta y}{\Delta x}$ = 18,745.81

Using the equation 3.2:
$E_b = S_t (t_f - t_r)$ E_b = 18,745.81 (13.26-1.69) = 216.8 GPa = 0.7 C/S at 500 MPa

Appendix G: TGA Analysis

2.0 C/S Mixing Ratio of C-S-H :

Raw Data for:

At 150	99.780392
At 400	83.0231135
At 600	80.4887545
At 825	79.1353233

Calculations for % mass loss over region 1 (C-S-H), region 2 (CH), and region 3 ($CaCO_3$):

1 (C-S-H), $\%mL_1$: Difference from Temperature at 400°C to 150°C
99.780392-83.0231135 = $\underline{16.76 = \%mL_1}$

2 (C-S-H), $\%mL_2$: Difference from Temperature at 600°C to 400°C
83.0231135 -80.4887545= $\underline{2.53 = \%mL_2}$

3 (C-S-H), $\%mL_3$: Difference from Temperature at 825°C to 600°C
80.4887545-79.1353233= $\underline{1.35 = \%mL_3}$

Using the equation 3.35, 3.36, and Molecular weight for each component listed:

$$C/S = \frac{\overline{C/S}(100-\%mL_1-4.113\%mL_2-2.274\%mL_3)-3.336\%mL_2}{100-\%mL_1-\%mL_2-2.274\%mL_3} \quad (3.35)$$

$$x = \frac{\%mL_1\left(3.115\overline{(C/S)}+3.337\right)}{100-\%mL_1-\%mL_2-2.274\%mL_3} \quad (3.36)$$

Molecular weight:

H_2O :	18.01	g/mole
CH:	74.10	g/mole
CO2:	44.01	g/mole
CaCO3:	100.09	g/mole
C-S-H:	CaO(C/S)+SiO2+((18.01)*x)	g/mole
SiO2:	60.01	g/mole
CaO:	56.1	g/mole

Determinate of stoichiometric formula for the 2.0 C/S ratio, $C_{(C/S)}\ SH_{(x)}$:

$$C/S = \frac{(2.0)(100-16.76\ -4.113(2.53)-2.274(1.35))-(3.336(2.53))}{100-16.76-2.53-2.274(1.35)} = 1.69$$

$$x = \frac{(16.76)(3.115(2.0)+3.337)}{100-(16.76)-(2.53)-2.274(1.35)} = 2.06$$

$$C_{(C/S)}\ SH_{(x)} = C_{(1.69)}\ SH_{(2.06)}$$

0.9 C/S Mixing Ratio of C-S-H :

Raw Data for:

At 150	99.98941
At 400	87.18402
At 600	84.87988
At 825	84.00956

Calculations for % mass loss over region 1 (C-S-H), region 2 (CH), and region 3 ($CaCO_3$):

1 (C-S-H), $\%mL_1$: Difference from Temperature at 400°C to 150°C
99.98941-87.18402= 12.81= $\%mL_1$

2 (C-S-H), $\%mL_2$: Difference from Temperature at 600°C to 400°C
87.18402-84.87988= 2.30= $\%mL_2$

3 (C-S-H), $\%mL_3$: Difference from Temperature at 825°C to 600°C
84.87988-84.00956= 0.87= $\%mL_3$

Using the equation 3.35, 3.36, and Molecular weight for each component listed:

$$C/S = \frac{\overline{C/S}(100-\%mL_1-4.113\%mL_2-2.274\%mL_3)-3.336\%mL_2}{100-\%mL_1-\%mL_2-2.274\%mL_3} \quad (3.35)$$

$$x = \frac{\%mL_1\left(3.115\overline{(C/S)}+3.337\right)}{100-\%mL_1-\%mL_2-2.274\%mL_3} \quad (3.36)$$

Molecular weight:

H_2O : 18.01 g/mole
CH: 74.10 g/mole
CO2: 44.01 g/mole
CaCO3: 100.09 g/mole
C-S-H: CaO(C/S)+SiO2+((18.01)*x) g/mole
SiO2: 60.01 g/mole
CaO: 56.1 g/mole

Determinate of stoichiometric formula for the 2.0 C/S ratio, $C_{(C/S)}\ SH_{(x)}$:

$$C/S = \frac{(0.9)(100-12.81\ -4.113(2.30)-2.274(0.87))-(3.336(2.30))}{100-12.81-2.30-2.274(0.87)} = 0.73$$

$$x = \frac{(12.81)(3.115(0.9)+3.337)}{100-(12.81)-(2.30)-2.274(0.87)} = 0.95$$

$$C_{(C/S)}\ SH_{(x)} = C_{(0.75)}\ SH_{(0.95)}$$